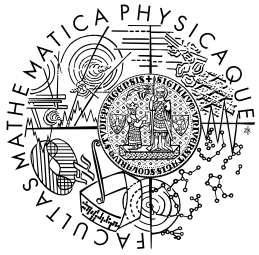

FACULTY
OF MATHEMATICS
AND PHYSICS
Charles University

MASTER THESIS

Vojtěch Partík

Exploring Galaxy Evolution in the Virgo Cluster

Astronomical Institute of Charles University

Supervisor of the master thesis: Dr. Rhys Taylor
Study programme: Astronomy and Astrophysics
Study branch: FAAP

Prague 2024

I declare that I carried out this master thesis independently, and only with the cited sources, literature and other professional sources. It has not been used to obtain another or the same degree.

I understand that my work relates to the rights and obligations under the Act No. 121/2000 Sb., the Copyright Act, as amended, in particular the fact that the Charles University has the right to conclude a license agreement on the use of this work as a school work pursuant to Section 60 subsection 1 of the Copyright Act.

In ..... date ....

Author's signature

First and foremost, I need to thank my supervisor Dr. Rhys Taylor for his tremendous help, support and witty humor throughout writing this thesis. I would also like to thank my family and friends for keeping my mental health somewhat in check during the last few years.

Title: Exploring Galaxy Evolution in the Virgo Cluster

Author: Vojtěch Partík

institute: Astronomical Institute of Charles University

Supervisor: Dr. Rhys Taylor, Astronomical Institute of the Czech Academy of Sciences

Abstract: Galaxies are some of the largest structures in the Universe, but there is still much about them that we do not know, including the role of environment in their evolution. To study them we employ a wide range of observational techniques, one of which is through a study of the neutral hydrogen (HI). As it is more than twice as extended as the stellar component of galaxies, and thus much more easily disturbed, it makes an excellent indicator of the environmental processes the galaxies undergo. This work takes advantage of the Widefield Arecibo Virgo Environment Survey (WAVES) neutral hydrogen survey of the Virgo Cluster, conducted by the Arecibo radio telescope prior to its collapse. By analyzing the WAVES region in radio and optical data and comparing it to an adjacent part of the Virgo Cluster, named VC1, I describe the possible evolutionary processes taking place. I conclude that the WAVES region is relatively more relaxed than VC1 and I further find compelling evidence of evolution through gas loss of the dwarf irregular galaxies into dwarf ellipticals, while also putting a constraint on the maximum HI mass of early-type galaxies in the studied region.

Keywords: Arecibo telescope, galaxies, Virgo Cluster, neutral hydrogen

Contents

1. Introduction

1.1 Gas and its role in star-forming galaxies

Hydrogen is the most abundant element in the Universe, and can be found in three main phases: neutral hydrogen (HI), ionized hydrogen (HII) and molecular hydrogen (H_2). These three phases are not always found in distinct structures and are often intermingled. However, they tend to occur preferentially in different parts of a galaxy, and the following description gives a simplified yet useful overview of the gaseous components of a typical galaxy (a gravitationally bound system of stars, dust and gas presumably embedded in a dark matter halo).

Firstly, neutral hydrogen is composed simply of a proton and an orbiting electron, creating a neutral total electric charge. HI can be found even in the space between the galaxies, but we see most of it in and around its host galaxies, in gaseous halo, which can extend as far as roughly twice the radius of its stellar component (Wolfire et al., 2003). It has typical temperatures of $T \sim 10^4$ K and interestingly keeps roughly the same density (typically ~ 10 $M_\odot pc^{-2}$ or $\sim 10^{21}$ cm^{-2}) throughout the galactic disk (Wolfire et al., 2003; Leroy et al., 2008), although this can of course vary galaxy to galaxy.

Secondly, molecular hydrogen is mostly found within the central molecular zone (CMZ) and the spiral arms of galaxies and with temperatures of $T \sim 100$ K, where the conditions can be favorable to satisfy the Jean's criterion. These regions can then fuel and support star formation, but the actual distribution of H_2 is more complicated than the HI, and its understanding is also made more difficult by observational limitations. As H_2 is a symmetrical molecule, its emission in the optical part of the spectrum is very weak. All this hinders any ground observations and therefore alternative approaches need to be taken, such as observing the CO molecules, which occupy roughly the same space as H_2 or observing the H_2 emission lines from space (Gnedin et al., 2016).

Lastly, ionized hydrogen has typical temperatures around $T \sim 10^6$ K, but can be even hotter than this, as there is no real upper limit to its temperature. Because of its temperature HII is too hot to fulfill the Jean's criterion and thus cannot contribute to star formation in any significant way. But it does materialize in so-called HII regions found around very hot OB stars, thanks to their highly energetic radiation, which is enough to ionize the HI. Besides HII regions, ionized hydrogen can also be detected throughout the whole galaxy, reaching even further than HI (Wolfire et al., 2003).

Although there is not much evidence HI is directly responsible for star formation (SF), it seems to serve as reservoir for the molecular hydrogen, which can then collapse into stars (Leroy et al., 2008). Hence if a galaxy still has a lot of HI, it can be expected that it has fairly young SF regions and can be still forming new stars.

It is also important to note that HI plays an important role in galaxy evolution throughout its entire history. For example, a less evolved galaxy has not yet used up all the available HI for star formation and can use its H_2 fuel to form many new massive blue OB stars and slowly replenish the H_2 via its HI reservoir. The large number of young and massive stars then give its host galaxy its characteristic

blue color. On the other hand, if a galaxy has used up most of its HI, the star formation has been quenched (stopped) and only the older, colder and redder stars are left. These galaxies then logically tend to be redder. This mechanism is of course a simplified description, as there are many exceptions to these general trends. But in general most galaxies seem to follow such behavior (Bell et al., 2004; Gavazzi et al., 2010).

Many of the processes driving galaxy evolution remain poorly understood. Some prefer the idea that galaxy type is largely predetermined by the environment where it was formed and subsequent processes play only a minor role (Dressler, 2004). Others, like Cortese and Hughes (2009); Dunne et al. (2011); Kenney et al. (2013), suggested that it can be in fact driven by gas loss and other environmental processes. This makes the study of gas very important for understanding the galaxies as a whole.

To understand galaxy evolution, we must first categorize the galaxies, and if one wants to classify a vast number of observed galaxies one option is to do so based on their appearances - morphology. Then, in the most simple terms we can sort them into two categories: "late-type" galaxies (LTG) and "early-type" galaxies (ETG) (Hubble, 1926).

Late-type galaxies usually show some kind of optical structure, which can be either spiral arms, galactic bars, star-forming regions or the galaxy itself may have an irregular shape. This group consists of spiral and irregular galaxies, of which notable examples are our Galaxy (the Milky Way), M31 and NGC 1427, as shown in figure 1.1. Kinematically, spiral galaxies are characterized by organized rotation-dominated motions of the stars and gas around the galactic center. Although not a strict rule, late-type galaxies typically have a detectable HI content.

Early-type galaxies, on the other hand, are much more smooth, with no clear structure and their motions are dispersion-dominated. This group consists primarily of elliptical and lenticular galaxies, such as M87, M49 or NGC 5866, as shown in figure 1.1. The origins of early-type galaxies are still being discussed, but elliptical galaxies are generally believed to have formed through mergers of late-type disk galaxies (Toomre and Toomre, 1972; Barnes, 1988). In contrast, dwarf spheroidal galaxies may have formed from gas loss or through interactions of late-type dwarf irregulars (Moore et al., 1996). Early-type galaxies also usually tend to have very little or no HI component, which quenched their star formation, compared to their late-type counterparts.

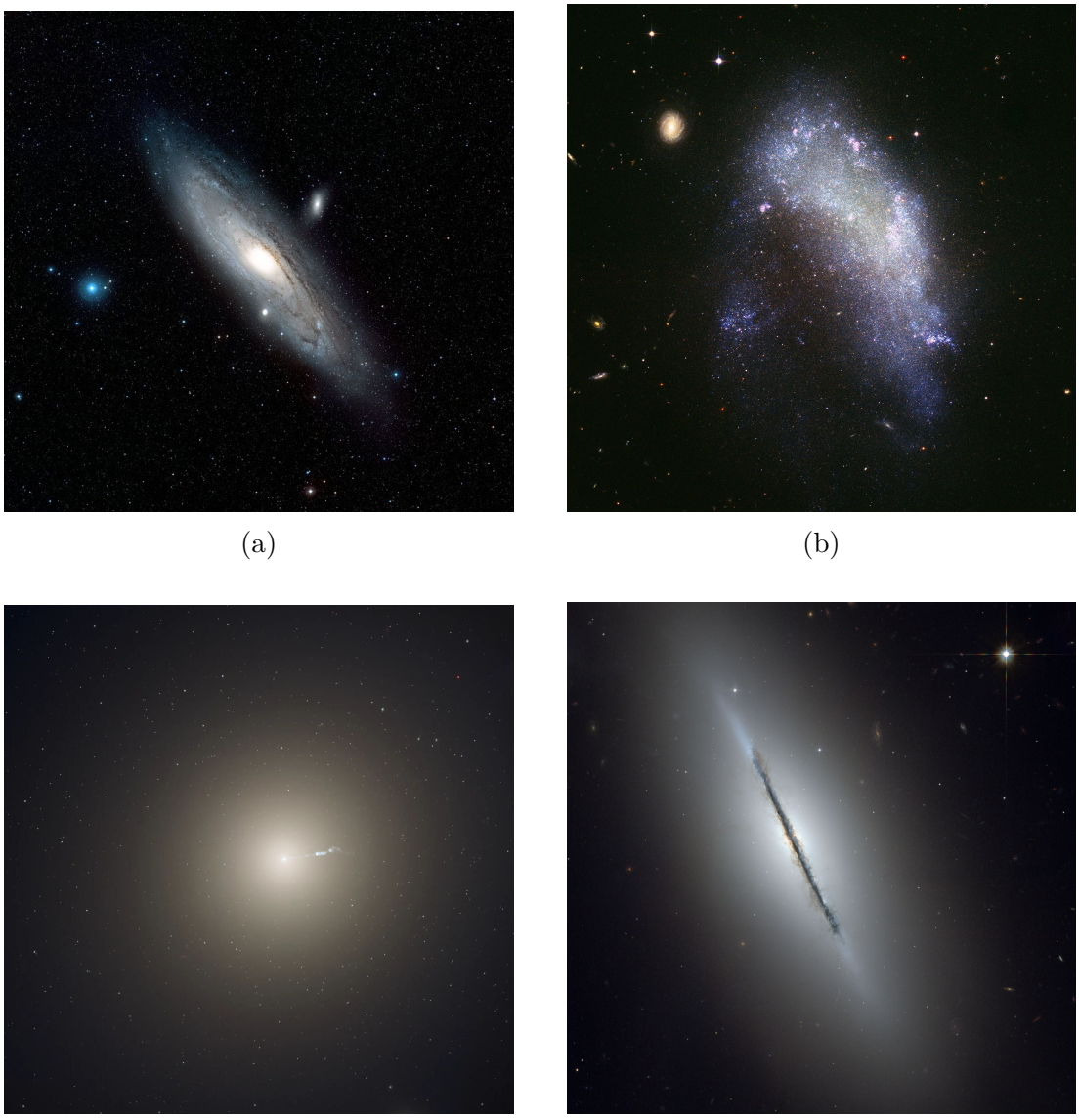

(a) (b)

(c) (d)

Figure 1.1: Examples of galactic types: (a) Spiral late-type galaxy, M31. (b) Irregular late-type galaxy, NGC 1427A. (c) Elliptical early-type galaxy, M87. (d) Lenticular early-type galaxy, NGC 5866. (a) credit: ESA/Hubble and Digitized Sky Survey 2. (b), (c) and (d) credit: NASA, ESA, and The Hubble Heritage Team.

That being said one should keep in mind the definitions are not always strict and in practice different people might classify a single object differently. However, galaxies generally tend to divide into a red sequence consisting mainly of early-types and a blue cloud of late-types on what is known as the color-magnitude diagram, which we will see in section 3.5.6, but the transition region between them is quite underpopulated. That would mean the galaxies do not stay in such states for very long. Some, like Eales et al. (2016), even claim that there is no clear break between these two categories and they are simply a result of colors of galaxies not changing much below a critical value of specific star formation rate. But despite this, the existence of red and blue sequences is generally accepted as genuine. We also need to remember that the terms ”late” and ”early” can be

misleading, since they do not refer to their actual age or evolution but rather their position on the Hubble sequence, which we will introduce later in this section.

Hubble (1926) wrote in his original paper:

> "Early" and "late," in spite of their temporal connotations, appear to be the most convenient adjectives available for describing relative positions in the sequence.
>
> ...
>
> Terms which apply to series in general are available, however, and of these "early" and "late" are the most suitable. They can be assumed to express a progression from simple to complex forms.

There are many ways to further describe galactic morphologies, one of which is the popular Hubble tuning fork, first proposed by Hubble (1936), see figure 1.2. That comes with many caveats, especially because since its first publication in 1934 the advancement in observational equipment, larger and deeper surveys and more detailed research led to discovery of galaxies which do not fit into the tuning fork at all (e.g. peculiar galaxies or ring galaxies). Today, instead of creating extremely precise but cumbersome categories, we use a more general morphology classification system in a form of a linear sequence (Gavazzi et al., 2003). Table 1.1 shows the linear classification system, including the division of early-type and late-type galaxies.

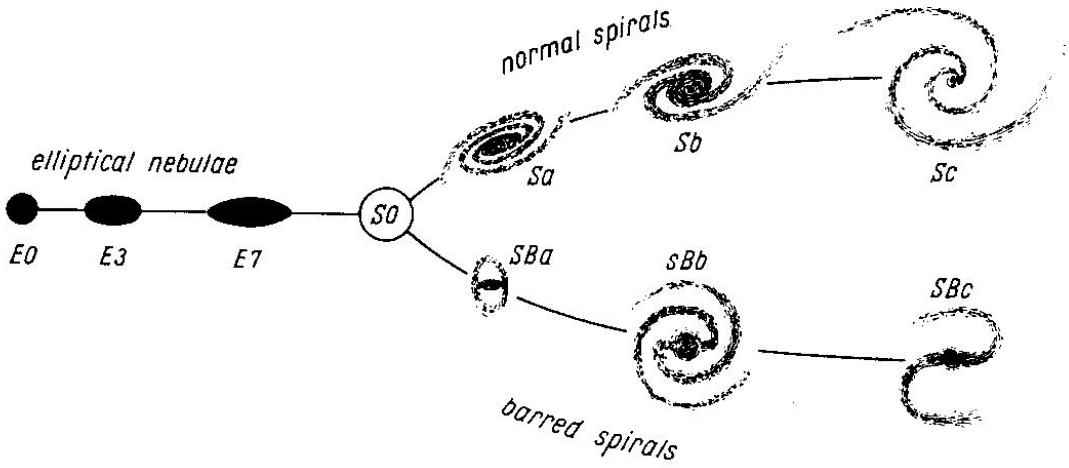

Figure 1.2: Original Hubble tuning fork for classification of galactic types. Credit: (Hubble, 1936).

	Linear type	Hubble type
Early-type galaxies	-3	dS0
	-2	dE/dS0
	-1	dE (d:E)
	0	E - E/S0
	1	S0
	2	S0a - S0/Sa
Late-type galaxies	3	Sa
	4	Sab
	5	Sb
	6	Sbc
	7	Sc (dSc)
	8	Scd
	9	Sd
	10	Sdm - Sd/Sm
	11	Sm
	12	Im (Im/S)
	13	Pec
	14	S/BCD (dS/BCD dS0/BCD Sd/BCD)
	15	Sm/BCD
	16	Im/BCD
	17	BCD
	18	S (dS)
	19	dIm/dE
	20	?

Table 1.1: Linear morphological classifications. Early/Late type classification is also shown.

Since HI is considered to be a reservoir of fuel for star formation, which affects both the color and therefore morphology of galaxies, understanding HI plays a crucial role in understanding their morphological evolution (Bacchini et al., 2019). Being more extended than H_2, it is also easier to disturb through processes which we will describe in the next section. Moreover, HI allows us to study systems and objects which are optically dark. Observationally, HI emission also has practical advantages, as its detection is much less weather dependent than higher frequency observations, such as optical, as it can easily pass through various environments which otherwise block optical emissions, like dark clouds or Earth's atmosphere (Dickey and Lockman, 1990). So, in order to get a more complete view of the Universe it is necessary to observe the neutral hydrogen emission as well as the optical one.

1.2 Galactic environments and processes

Galaxies are not distributed evenly throughout the Universe. Most of them can be found in small groups, where only a few of the galaxies have mass comparable or larger than our Galaxy. For example our Local Group, which hosts our Galaxy and M31, is one such system. Sometimes however, they are found in clusters,

which are filled with a hot intracluster medium (ICM) and can contain thousands of galaxies, with possibly hundreds of massive ones. Some of the closest examples are the Coma and Virgo clusters. More rarely they can also be found in isolation (or voids), with perhaps a few minor companion satellite galaxies.

Galactic clusters are very interesting places and great laboratories for the study of environmental effects, because their environment is so drastically different from groups and isolated galaxies. Therefore we distinguish between clusters and other environments, which we generally call "field". The presence of a galaxy in a cluster or the field is described by the observed morphology density relation, which shows that early-type galaxies are prevalent in high density environments such as clusters, whereas late-type galaxies are more often found in the lower density field (Dressler, 1980; Hashimoto et al., 1998). This can also be interpreted as evidence that galactic environment is either directly or indirectly responsible for galactic evolution (Boselli et al., 2014).

As stated before, the mechanisms behind galaxy evolution are still not fully understood, but one idea is that some galaxies, especially the ones in large clusters, were formed as early-type galaxies and do not change their morphology much in their lives, while others formed as late-types but were transformed through various processes into early-types. Perhaps the most cited mechanism for conversion of spiral galaxies into S0s is gas loss through ram pressure stripping (RPS) (Hashimoto et al., 1998; Dressler, 2004).

RPS mainly occurs in galactic clusters due to the ICM, which is made of hot ionized gas, with temperatures around $T \sim 10^7 - 10^8$ K. Because of such high temperatures, it radiates hard X-ray radiation and makes up about 15% of the total cluster mass (Sparke and Gallagher, 2007). When a galaxy moves through the ICM, it exerts pressure on the gas bound to the galaxy and if the pressure is greater than gravity, the gas is stripped and left behind with the galaxy's stellar component unaffected.

There are several ways and methods to detect this process (Gunn and Gott III, 1972). One method is to calculate the HI deficiency of a galaxy, which is essentially how much gas the galaxy is thought to have lost, by comparing its HI mass with that of a typical galaxy of the same size and morphology. Its value is given by

$$D_{\mathrm{HI}} = \log M_{\mathrm{HI}_{\mathrm{ref}}} - \log M_{\mathrm{HI}_{\mathrm{obs}}}, \tag{1.1}$$

where $M_{\mathrm{HI}_{\mathrm{ref}}}$ is the predicted HI mass and $M_{\mathrm{HI}_{\mathrm{obs}}}$ is the observed HI mass (Giovanelli and Haynes, 1985). The predicted HI mass can be calculated based on the optical diameter d using the equation

$$\log M_{\mathrm{HI}_{\mathrm{ref}}} = a + b \times \log d, \tag{1.2}$$

where a and b are parameters, which can either be general for all galaxies or based on their morphological classification.

The exact value of HI deficiency is however subject to high intrinsic scatter (typically ~ 0.3), so one can only really say a galaxy is negatively deficient (contains more gas than expected) for values lower than -0.3, is not deficient for values from -0.3 to $+0.3$ (contains a typical gas content), is moderately deficient for values from $+0.3$ to $+0.6$ and is strongly deficient for values greater than $+0.6$.

HI deficiency by itself is not direct evidence of RPS. Even if a galaxy is HI deficient, it does not mean it is currently losing gas, as this could have happened in the past. It needs to be combined with other supporting evidence in order to determine the real nature of the galactic processes which took place.

More direct evidence of gas removal can be the presence of gas tails, which are stripped from their parent galaxies and can be detected in HI (Oosterloo and van Gorkom, 2005; Chung et al., 2007). Still not many deficient galaxies seem to have gas tails present in their vicinity (Taylor et al., 2020). This can be for a number of reasons, including possible phase change or dispersal of the gas below detectable limits.

Another possible way to infer the gas loss mechanism is the method created by Köppen et al. (2018), which is an analytical approach to predict the gas removal. It uses an estimate of the local pressure the galaxy is experiencing given its velocity and position in the cluster and the required pressure to strip the HI. Taylor et al. (2020) further explored this model to predict the number of galaxies with observable HI streams. Unlike the HI deficiency, it can describe current gas removal, however the required data for this method is usually not available.

While RPS is believed to be the dominant gas-loss mechanism in galactic clusters, field galaxies are most often disrupted due to tidal interactions. When a galaxy undergoes tidal encounters with another, it can often distort the appearance of the whole galaxy. Hence if we observe, for example, a pair of galaxies interacting, exchanging gas and disrupting each other's structure, the most likely process occurring is a tidal interaction (Toomre and Toomre, 1972). If a galaxy undergoes a high-speed encounter, it is usually less damaging, because the interaction forces occur for a shorter time. That may cause limited changes in its geometry and properties, but probably will not lead to any great degree of damage to its gas or stellar component. However, in clusters there is a high concentration of galaxies and their mutual velocities are higher, due to the deeper gravitational well and therefore higher escape velocity. Hence, in clusters a galaxy can experience many high-speed encounters, a process known as "harassment", which then can become more significant.

In contrast, if galaxies interact at velocities lower than their escape velocities, they can become gravitationally bound and merge into a single object. Mergers are then further sorted into two categories. A minor merger occurs when the two merging galaxies have greatly different masses. In that case the less massive galaxy is "consumed", while the more massive one suffers relatively minor damage. But if the masses of the galaxies are comparable, i.e. a major merger, the damage is usually much bigger and can lead to complete change of appearance, properties and may even cause morphology change of late-type galaxies into early-type (Binney and Tremaine, 2011). The mass ratio dividing mergers into major and minor is typically considered to be roughly 1:3 or 1:4, with higher ratios corresponding to minor mergers and lower ratios corresponding to major mergers (Conselice, 2006; Lotz et al., 2008).

During a galaxy merger, gas can be even supplied, as opposed to RPS, which can potentially lead to the birth of starburst regions with very high star formation rates. But mergers are quite rare in clusters, since the velocity dispersion of its members is typically too high to allow it. That leaves galaxy clusters as an ideal place to study ram pressure stripping, since it dominates other gas-loss processes.

1.3 The Virgo Cluster

The Virgo Cluster is, at around $d \sim 17$ Mpc, the closest large cluster of galaxies to us and it is also a member of the Virgo Supercluster, which includes our Local group (Gavazzi et al., 1999). Its relative nearness is not only convenient but also of great importance, because the member galaxies have angular size large enough to resolve very fine details, unlike many of the other large galaxy clusters. It is made of over 150 large galaxies and thousands of smaller ones. It also contains approximately twice as many early-type galaxies than the late-types (Binggeli et al., 1985). The total mass is still heavily debated and largely depends on the methodology and the extent to which the mass is computed, but it is generally estimated at around $\sim 10^{14} - 10^{15}$ $M_\odot$ (Schindler et al., 1998; Fouqué et al., 2001; Karachentsev et al., 2018).

The exact structure of the cluster is still being studied but it is generally agreed that the main body of the cluster lies $\sim$ 17 Mpc from our Galaxy. It has also been observed that the cluster is still forming with three major infalling clouds (or subclusters), which can be as far as $\sim$ 32 Mpc away from us. They are named Cluster A, B and C and some additional clouds (W, W', M and LVC), although their association with the cluster as a whole is not certain (Gavazzi et al., 1999; Boselli et al., 2014).

As well as its spatial complexity, the structure of the Virgo Cluster is also difficult to study thanks to its velocity dispersion, roughly $\sim 650 - 750$ kms^{-1}, which makes the Hubble law ($d \sim v$) effectively invalid for the distance measurements (Jun-liang et al., 1991; Kashibadze et al., 2020). This means the Virgo Cluster can contain galaxies with velocities that can differ by hundreds of kms^{-1} but are at the same distance from us. Redshift (velocity) measurement can still be supportive evidence for a given galaxy's cluster membership, but not used by itself alone.

The center of the Virgo Cluster is generally considered to be the massive early-type galaxy M87, which also defines the center of Cluster A. About 4 degrees south of M87 lies another (less) massive early-type galaxy M49, which, defines the center of Cluster B. Cluster A contains roughly four times as many members as Cluster B (Boselli et al., 2014). These substructures have quite different properties - masses, velocity dispersions and galaxy densities, which makes the Virgo Cluster an excellent laboratory for study of galaxies and galactic processes, even tidal encounters and most importantly ram pressure stripping (Boselli et al., 2014).

Given the cluster's distance and complexity it was an obvious target for study for Binggeli et al. (1985) and their subsequent publications of the Virgo Cluster Catalog (VCC). It includes 2096 VCC galaxies observed over ~ 140 deg^2 and has become the foundation of practically all galactic research in the Virgo Cluster. This catalog includes 1277 Virgo Cluster member galaxies, 574 possible members and 245 background objects. See figure 1.3 for the plot of all members and possible members.

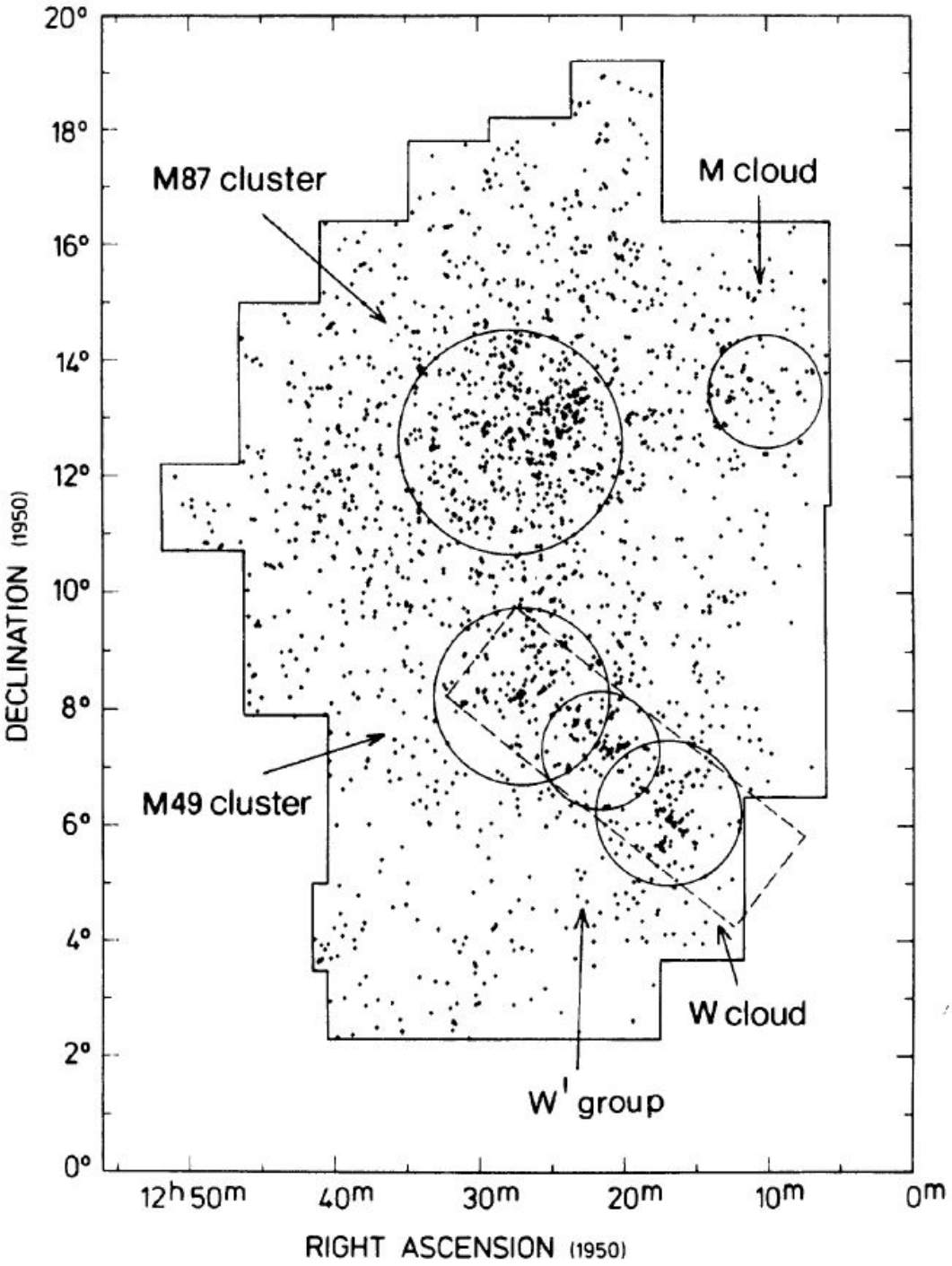

Figure 1.3: Plot of all members and possible members of the Virgo Cluster listed in the VCC. The M87 and M49 clusters are Cluster A and Cluster B respectively. The outlined section is the area of the original VCC survey. Credit: (Binggeli et al., 1987)

1.4 The HI 21 cm emission line

The 21 cm HI emission line was first detected by Ewen and Purcell (1951) and now serves as one of the most important methods of detecting neutral hydrogen. Thanks to this we can study the shape, mass, dynamics, distribution and other

features of HI in galaxies and other cosmic objects. It has also played a crucial role in observing the rotational curves of spiral galaxies, which supported the existence of dark matter (Rubin and Ford Jr, 1970; Corbelli and Salucci, 2000).

Radio observations of the 21 cm line are important since HI does not have easily detectable emission lines in the optical part of the spectrum. This is because of its typical temperature, $T \sim 10\ 000$ K, most of the atoms are in their ground state (Field, 1958) and hence cannot radiate via energy level transitions. Instead, they can radiate using a totally different mechanism.

As HI is made of a single proton and electron there are two possible configurations of the total spin (both electron and proton have a spin value of $\pm\frac{1}{2}$) in its ground state, which we call the hyperfine states. If the spins are antiparallel (up and down), we get the total spin angular momentum $F = 0$, which also corresponds to the lowest energy level of the atom. But if the spins are parallel (up and up), the atom has a $F = 1$ and a slightly higher energy level ($\Delta E = 5.9 \times 10^{-6}$ eV) (Field, 1958). So, when the atom goes from the higher energy state to lower it experiences a spin-flip transition and the energy difference is radiated as a photon with a wavelength of

$$\lambda = \frac{c}{\nu} = \frac{hc}{\Delta E} \approx 21.1 \text{ cm}, \tag{1.3}$$

where h is the Planck constant and c is the speed of light (Hellwig et al., 1970). As these energies are extremely small, the atoms are easily excited into the parallel configuration by any source of energy available, for example by absorbing another photon or by collisions.

For an individual atom, the spontaneous transition is very rare, with a probability of $\sim 2.85 \times 10^{-15}$ s^{-1}, which translates to roughly one transition per 10^7 years (Field, 1958). That would make the described mechanism extremely ineffective and impossible to detect. Fortunately, the collisions between particles of HI increase the probability of the transition occurring, to the point where we are able to detect galaxies with even a relatively low gas content.

Given its wavelength, the 21 cm line is only detectable by using radio telescopes, which generally fall into two groups: single-dish or arrays. This is usually a trade-off between sensitivity and resolution, because the size of the beam is given by

$$\Theta = 1.22 \times \frac{\lambda}{D}, \tag{1.4}$$

where λ is the wavelength and D is the diameter of the radio telescope dish. Any detectable structure smaller than Θ will not resolvable, since its size is smaller than the "pixel" of the image. D is fixed for the single-dish telescopes (usually in $\sim 50 - 100$ m) but it can be variable in most arrays, by moving the individual receivers, where it can reach up to several kilometers reaching astonishing spatial resolution. Even in arrays without movable dishes, it is possible to choose which antennae contribute to the signal the most and thus change the resulting resolution.

However, as interferometric radio telescope arrays are made of smaller individual dishes, its effective area is not as large as for a single-dish and due to complicated interferometric limitations its sensitivity is made worse by several

orders of magnitude. For comparison, the Very Large Array (VLA), despite having great resolution, has roughly 5 times smaller effective area than the Arecibo radio telescope. But in order to achieve similar mass sensitivity, it cannot simply increase its integration time by the same factor of 5. Due to the aforementioned interferometric effects the required time is in fact larger by a factor of 100. In other words, instead of observing a source for 5 minutes, it has to do a pointing for 8 hours, making it very time inefficient if the resolution of the object is not a priority (Thompson et al., 1980).

Another advantage of single-dish radio telescopes is their greater survey speed. Modern single-dish radio telescopes usually take advantage of multibeam receivers, which decrease the time necessary for sensitive surveys by surveying multiple parts of the sky simultaneously (McClure-Griffiths et al., 2023). That makes them more optimized for discovering new objects, while array radio telescopes are preferred for their detailed studies.

Using either radio instrument, we can determine the mass of the observed HI source using the standard HI mass equation

$$M_{HI} = 2.36 \times 10^5 \times d^2 \times F_{HI}, \tag{1.5}$$

where d is the distance in Mpc and F_{HI} is the integrated HI flux in Jykms^{-1} (Roberts, 1962).

1.4.1 Optically dark HI in the Virgo Cluster

In a typical disk galaxy HI extends well beyond the stellar disk but it can also be found in complete isolation from the stellar component, i.e. with no associated optical galaxy. The Virgo Cluster hosts a number of these gas clouds, as well as galaxies with tails and extensions and other unusual features. These structures can be results of RPS or other environmental processes. Taylor et al. (2012) reported of a number of dark clouds in a part of the Virgo Cluster with the typical velocity width of $W_{20} \sim 150$ kms^{-1}, size $\lesssim 20$ kpc and mass $\sim 10^7$ M$_\odot$. They suggested they could have been either associated with unusually optically faint galaxies, stripped from their parent galaxies or not be associated with anything at all and thus be a "dark galaxy".

Various other optically dark (or very faint) HI features are known in Virgo. Some examples are the VIRGOHI21, which is an HI overdensity in a stream with hints of ordered rotation, HI1225+01, which is a stream-like feature of HI with no optical counterpart capable of supplying enough gas to explain its formation (Taylor et al., 2016) or the ALFALFA Virgo 7 complex (AV7).

AV7 complex, first reported by Kent et al. (2007), is an especially peculiar object. It is comparable in size and mass to VIRGOHI21 and HI1225+01, but all of these are much more massive and extensive than the AGES clouds. It is composed of five optically dark clouds (C1, C2, etc.) of neutral hydrogen located approximately 3 degrees south of M87, with velocity widths as high as $W_{20} \sim 280$ kms^{-1} and it spans $\sim 35'$ or roughly 200 kpc at the Virgo Cluster distance. Each of its individual clouds has an HI mass between 0.5×10^8 and 1.7×10^8 M$_\odot$, which translates to the total HI mass of 5.1×10^8 M$_\odot$, an order of magnitude higher than already known "typical" dark clouds mentioned earlier. The sheer size, mass and highly complex internal structure with a unique combination of

properties make this complex so puzzling. For more information see Kent et al. (2009); Minchin et al. (2019); Jones et al. (2024).

Given that Minchin et al. (2019) already analyzed the same data used in this work to study the AV7 complex in detail, I do not re-examine it here. Rather the purpose of this study is to catalog and analyze the full data set in this region, which was not done by Minchin et al. (2019). This can potentially provide important context for understanding AV7 complex, but I do not study it here directly.

1.5 Objectives of the thesis

In this work I intend to continue and build on previous observations to help and extend the Virgo Cluster's HI map. I will partially rely on comparison with other parts of the Virgo Cluster described by Taylor et al. (2012) and Taylor et al. (2013). I will measure the major parameters of HI objects in the data sample, including their positions, systemic velocities, HI fluxes, etc. to provide reliable statistics. I will also obtain optical measurements, specifically photometric magnitudes and radii of the galaxies, to supplement the radio data.

The following analysis will then be based partially on comparisons with a region of the Virgo Cluster directly adjacent to the one studied in this work, and partially by studying in more depth the individual objects which may not follow general trends. The comparisons are necessary simply because galaxy evolution and processes cannot be observed in real time, therefore a study of different objects at different stages of their evolution is necessary. I will focus on trying to learn what is the environment like in the studied part of the cluster and how it may differ from other already studied parts, as the environment can have large impact on the evolutionary processes of galaxies. This will be done by studying the spatial distribution, colors, HI deficiency and other relevant parameters and statistics of the detected objects. For example, in the adjacent region of the cluster Taylor et al. (2012) found a population of dark clouds without optical counterparts, but should there be more or less in the region studied here might indicate a some systemic change throughout the cluster. I will further look for extensions and tails in the HI profiles, as they can provide direct evidence of ongoing gas removal, which likely affects their evolution. Ultimately, in this work I will try to address the issue of gas-loss driven evolution of galaxies but at the same time I acknowledge this is a very broad area of study which will certainly require more data for definite answers.

The rest of this work is organized as follows: In chapter 2 I describe the radio and optical data used in this work and the extraction techniques, in chapter 3 describe the process of obtaining the radio and optical data and its statistical analysis, in chapter 4 I discuss the results and I summarize my findings in chapter 5.

2. Observations

The advantage of modern astronomy is the access to many different types of data, most usually in the form of different parts (bands) of the electromagnetic spectrum. While all have their advantages and disadvantages, in this thesis I take advantage of the radio and optical data.

2.1 Radio data

Since the earliest days of radio astronomy there have been ambitions to map the HI properties of the deep sky. HI Parkes All Sky Survey (HIPASS) was the first all-sky HI survey, which used the Parkes 64-m telescope. It was conducted between 1997 and 2000 and it was able to cover 71% of the sky, with more than 5000 galaxies detected (Meyer et al., 2004; Wong et al., 2006). It took advantage of the Parkes multibeam receiver, achieving a beam size of 14.3 arcmin and 13.3 mJy root mean square (rms) noise (Barnes et al., 2001). Its discoveries included the Leading Arm of the Magellanic Stream and a number of other objects with no optical emission. HIPASS was a significant leap towards understanding the HI's role in the Universe, but thanks to advancements in radio astronomy more sensitive surveys were soon possible.

The Arecibo observatory in Puerto Rico was completed in 1963 as part of the United States Department of Defense's missile defense program. It was a 305 m single-dish radio telescope built into a natural sinkhole with a receiver platform suspended 150 m above the primary dish (see figure 2.1). Neither dish or the platform could move but the receiver was able to rotate and sway back and forth in order to move the focal point to the proper target. Initially intended as part of a plan to detect incoming missiles traveling in Earth's ionosphere but soon after its completion it was transferred to National Science Foundation for more peaceful purposes (NSF, 2021). It was capable of detecting the 21 cm emission line of neutral hydrogen but also able to perform active radar observations within our Solar system. Later, it underwent a series of upgrades, most notably in 1997 with the addition of the Gregorian dome, which greatly improved its observational capabilities but also added additional weight (Britannica, 2024). It continued to produce science until damage caused by hurricane Maria in 2017. This led to a series of snapped cables, its decommission and ultimately its collapse in 2020.

Figure 2.1: Arecibo radio telescope before its collapse. Credit: The New York Times

Despite its untimely demise, Arecibo was groundbreaking at the time and the largest radio telescope in the world for more than half a century. It had about 5 times smaller beam than HIPASS (3.5 arcmin], which made the detection of optical counterparts of HI emissions much easier and more reliable. Over the years it hosted a number of blind HI surveys, such as the Arecibo Legacy Fast ALFA (ALFALFA) survey, which mapped $\sim$ 7000 deg^2 of the sky visible to Arecibo. It utilized the drift scan observing technique, where the telescope is pointed at a part of the sky and is fixed in place while the sky drifts overhead (Giovanelli et al., 2005). It achieved *rms* noise of 2.2 mJy and in some parts of the sky even discovered 18 times more HI objects than HIPASS.

ALFALFA served as the foundation of a "wedding cake" observing strategy, with AGES and Arecibo Ultra Deep Survey (AUDS) as its next tiers with increasing sensitivity but decreasing area covered. While AGES filled the middle tier of the wedding cake strategy, AUDS was another drift scan survey of two small selected areas into a much larger depth (rms $\sim$ 0.05 mJy) (Freudling et al., 2010).

2.1.1 Arecibo Galactic Environment Survey

The Arecibo Galactic Environment Survey was a precursor to our own Wide Arecibo Virgo Extragalactic Survey (WAVES) data and it was similar to ALFALFA in properties and observational techniques, but aimed to probe the HI emission in smaller regions and into more depth (Auld et al., 2006). Two of these regions were located in the Virgo Cluster, named VC1 and VC2, see figure 2.2. VC1 was a 10×2 deg^2 field centered on M49, whereas VC2 was a 5×1 deg^2 strip, which included most of Cluster C and extended slightly into Cluster A. Both

of these regions avoided the M87 galaxy due to the strong continuum source. AGES scientific goals were to compare the HI properties of galaxies in the cluster environment with those in the field and consequently improve models of environmental effects on galaxy evolution, such as RPS or tidal stripping.

AGES also utilized the ALFA (Arecibo L-band Feed Array) multibeam receiver in a 7-beam configuration in two polarizations for drift scan observations. With the sky allowed to drift overhead, it takes 12 seconds for a source to cross the 1.4 GHz beam on the sky. So to achieve the required ~ 0.5 mJy *rms* noise, it needed a total of 300 s of integration time, which translated to 25 separate scans (Auld et al., 2006). Such configuration allowed for an HI mass sensitivity limit of 5×10^7 $M_\odot$ per beam at the Virgo Cluster distance. The bandwidth spanned 100 MHz with 4096 channels, in velocity ranging from 2000 kms^{-1} to 20 000 kms^{-1} with a 5 kms^{-1} width of the spectral channel (Cortese et al., 2008).

The resulting data were in the form of "data cubes" (although being rather cuboid-shaped) in `.fits` format with three axes being the right ascension, declination and frequency, which was converted into heliocentric velocity for convenience. Given the relative strength of signal, the observations were of course sensitive to man-made radio frequency interference (RFI), like airport radars, mobile signals or satellites flying overhead. Notably, the Punta del Este Federal Aviation Administration radar caused strong RFI between 15 400 $\mathrm{kms}^{-1} < \mathrm{v} <$ 16 000 kms^{-1} or the L3 GPS satellite at roughly 8500 kms^{-1} (Taylor et al., 2012). As well as man-made signals, our own Galaxy produces such a strong signal that it renders the data over the range $-50 < v < +50$ kms^{-1} unusable. For the intermittent sources of RFI a median filtering can be applied with some success but the constant sources cannot be removed. Despite some channels being contaminated by this constant RFI sometimes we can still detect an HI source there, provided it is bright enough. Apart from the RFI and bright emission from the Milky Way, the edges of the data cubes were also affected with worse sensitivity than nominal, because of the multibeam receiver only covering these regions with 3 feeds instead of the full 7.

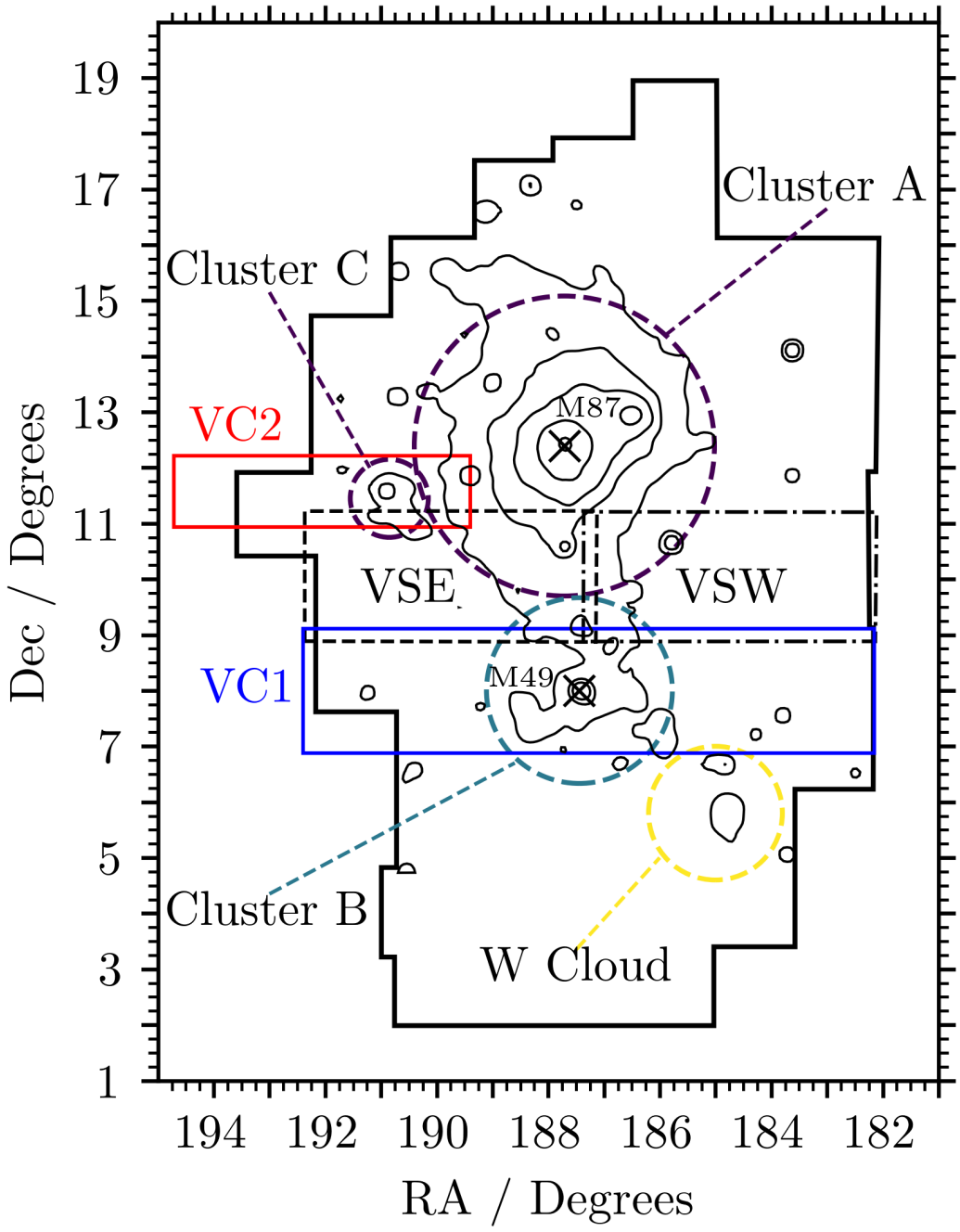

Figure 2.2: The Virgo Cluster within the VCC (black outline) with highlighted AGES' VC1, VC2 and WAVES' VSE and VSW regions, including positions of M87 and M49. The contours represent the X-ray gas density from Böhringer et al. (1994). Colors of clusters and clouds represent their distance: purple = 17 Mpc, blue = 23 Mpc, yellow = 32 Mpc, taken from Boselli et al. (2014).

2.1.2 Wide Arecibo Virgo Extragalactic Survey

WAVES was intended as a successor to AGES, designed to expand the survey in Virgo to eventually cover the whole cluster to AGES depth. Its technical details and observational techniques are identical to those of AGES, with only minor

increase of rms noise to ~ 1 mJy, which was likely caused by the hurricane Maria damage and possibly the M87 interference.

It was still ongoing when the telescope collapsed. While the 20 square degrees southern field had been fully observed by this point, only 10 out of the planned 35 square degrees of the northern field were actually observed. The observations took place in 2017 and 2018, with the first half of observations being conducted before the hurricane Maria damage and the rest after (Minchin et al., 2019). The WAVES South region is located directly north of VC1 centered at the filament spine of the X-ray gas connecting M87 and M49. It was split into two data cubes, named VSE and VSW for the eastern and western part respectively. The spatial area covered by VSE ranged from 12:28:30 to 12:49:28 in RA, and by VSW from 12:08:26 to 12:29:29 in RA, with the same of declination from +8:52:20 to +11:13:30 for both regions.

The main effort in this work is to catalog the WAVES South data cube and analyze the HI detections present. Thanks to WAVES being directly adjacent to the already studied VC1 region it allows us to conduct a similar study and make important comparisons between these two regions. That will help us to learn how the galactic environment changes throughout the Virgo Cluster and potentially how it affects galaxy evolution. See figure 2.2 for the comparison of VSE, VSW and the AGES footprints. This work focuses on the WAVES South field, with WAVES North left to a future work.

WAVES used the same scan pattern and data reduction pipeline as AGES (Auld et al., 2006; Minchin et al., 2019). Specifically, the data reduction was performed using the `AIPS++` packages `LIVEDATA` and `GRIDZILLA`, which were originally designed for HIPASS but were modified to be used on Arecibo's `CIMAFITS` file format. `LIVEDATA` first does bandpass estimation and removal, Doppler tracking and calibrates the residual spectrum. `GRIDZILLA` then co-adds all the spectra to produce the 3D data cubes (Auld et al., 2006). This process was done by Robert Minchin (NRAO) and took roughly a week to finish.

After I acquired the reduced data, I applied my own 2nd order polynomial baseline fitting along the spectral axis to reduce any remaining ripple in the baseline. This involves an iterative $2-\sigma$ clipping process, where points with signal-to-noise (S/N) ratio higher than 2 are ignored, the baseline is fitted with a polynomial and subtracted, and the whole process is repeated for five iterations. Lastly, Hanning smoothing was applied along the spectral axis to reduce Gibbs ringing near very bright HI sources. This reduces our resolution from 5 kms^{-1} to 10 kms^{-1} in velocity, but that is not a significant disadvantage since the velocity dispersion of a static gas cloud is $\sim 8-10$ kms^{-1} anyway due to its random thermal movements ($T \sim 10\ 000$ K). Position-velocity slice of the data cube showing the effects of the described reduction process is shown in figure 2.3.

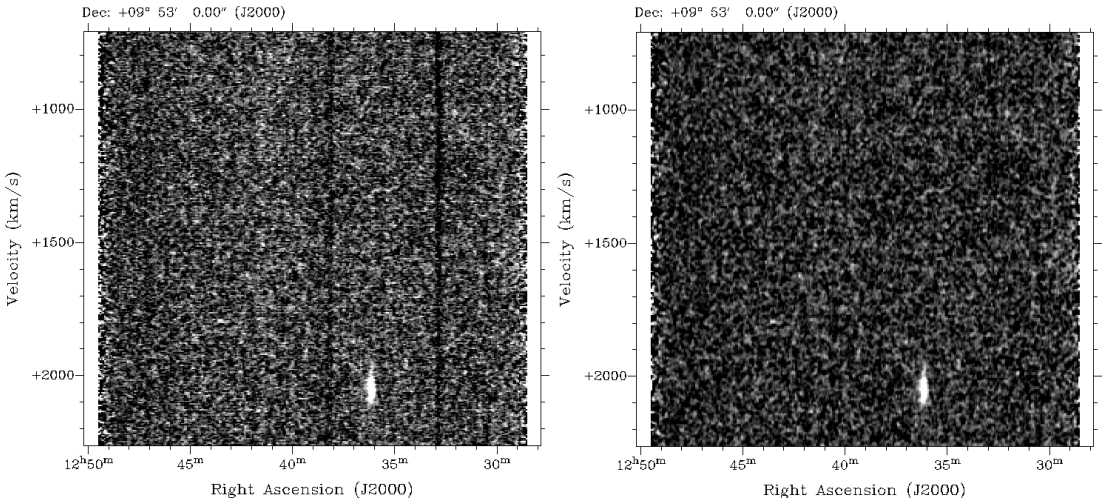

Figure 2.3: Position-velocity slice of the WAVES flux data cube before (left) and after (right) applying Hanning smoothing and a second polynomial baseline subtraction. Courtesy of Rhys Taylor.

2.2 Optical data

While radio data offers important information otherwise invisible to classic observations, it is necessary to compare with optical data as well. This is because in order to understand the role of gas, we need a comparison sample of HI non-detected galaxies, which in clusters usually makes up a larger population. Optical data further provides information to assign optical counterparts to HI sources and their respective morphological types, which in turn help us study galaxy evolution. For this work I have used the Galaxy On Line Database Milano Network, based on the original VCC, as the main source of optical objects because it is especially useful for the Virgo studies as it gives a volume-limited sample to certain brightness limit.

2.2.1 Galaxy On Line Database Milano Network

The Galaxy On Line Database Milano Network (GOLDMine) is an online database of the Virgo, Coma and Abell 1367 clusters, launched in 2002 with an interface for panning around the sky map. It combines the following catalogs: VCC by Binggeli et al. (1985), NGC by Dreyer (1888), IC by Dreyer (1895), CGCG by Zwicky et al. (1968) and UGC by Nilson (1973). It contains 3267 galaxies in total, with approximately 60% of early-types and 40% of late-types, which is consistent with the cluster environment as described in section 1.2.

The GOLDMine catalog, which for the purposes of this work is mainly based on the VCC, describes many properties of galaxies, including their coordinates, photometry measurements (although uncorrected for extinction), their systemic heliocentric velocity and their morphological type, using the linear classification system shown in table 1.1 (GOLDMine, 2002). It also offers the major a and minor b optical diameter determined from the original VCC photographic plates. For the Virgo Cluster objects the morphological types are based on the VCC catalog types by Binggeli et al. (1985). Despite some uncertainties, due to possible

overlap, every galaxy with a type value lower or equal to 2 is considered to be an early-type and 3 or higher to be a late-type. A special case may be the type 20, which indicates an unspecified type but typically has late-type morphology signs.

Another important quantity given by the GOLDMine catalog is the distance given in Mpc. In the Virgo Cluster the distance was assigned by Gavazzi et al. (1999). Due to the impracticality of manually measuring distance of 2000 galaxies, they measured only a selection (200 in total) of objects using the Fundamental Plane method for the early-types and the Tully-Fisher method for the late-types. Then they determined approximate boundaries based on the spatial morphology of the cluster on the sky and combined the average distance measurements for each substructure to assign it a single distance of either 17, 23 or 32 Mpc. This method of course leads to considerable uncertainties due to lack of individual distance measurements and the spatial dispersion of the individual sub clusters. Despite this the distances are reasonable for giving a broad view of the cluster on the large scale, which is my main goal.

2.2.2 Sloan Digital Sky Survey

Since its beginning in 2000, the Sloan Digital Sky Survey (SDSS) has become one of the largest deep optical sky surveys in history with a total mapped area of over 12 000 square degrees, which also includes the entire Virgo Cluster. It utilizes the 2.5 m optical telescope equipped with large-format mosaic CCD camera at the Apache Point Observatory in New Mexico, USA (York et al., 2000).

The mosaic camera of the SDSS provides photometry measurements in five optical bands u, g, r, i and z to a depth of up to ~ 26 mag, see figure 2.4 for an overview of the band ranges. The telescope is also equipped with two double fiber-fed spectrographs, which were used to measure spectra of approximately 10^6 brightest galaxies and 10^5 quasars (Abazajian et al., 2009). Besides photometry and spectroscopy, it also provides other automatically calculated properties of the measured objects, such as inclination angle and radius. The SDSS actually measures "Petrosian radius" (R_P), which is defined as a radius at which the following equation is satisfied

$$I(R_P) = \eta \left(\frac{\int_0^{R_P} I(r) 2\pi dr}{\pi R_P^2} \right). \tag{2.1}$$

Where $I(r)$ is the local intensity at the radius r from the galactic center, and η is a calibration constant with a value of 0.2 adopted by the SDSS (Shimasaku et al., 2001). In other words it is the radius calculated from the galaxy's center to the point at which the local intensity is equal to the averaged intensity, with some correctional factor. This definition has the advantages that it is independent of distance and it is insensitive to reddening by dust in the foreground. This is because as a ratio of the integrated and the local brightness, both are affected by reddening in the same way, leaving the ratio unchanged.

Of course, these quantities may be prone to error, especially with peculiar or low surface brightness objects, so in those cases an individual approach is needed. The SDSS database is accessible via the structured query language (SQL) online (though the user can also use the interactive online sky explorer to pan around the SDSS's sky data and view objects in "true" color). I have used the latest

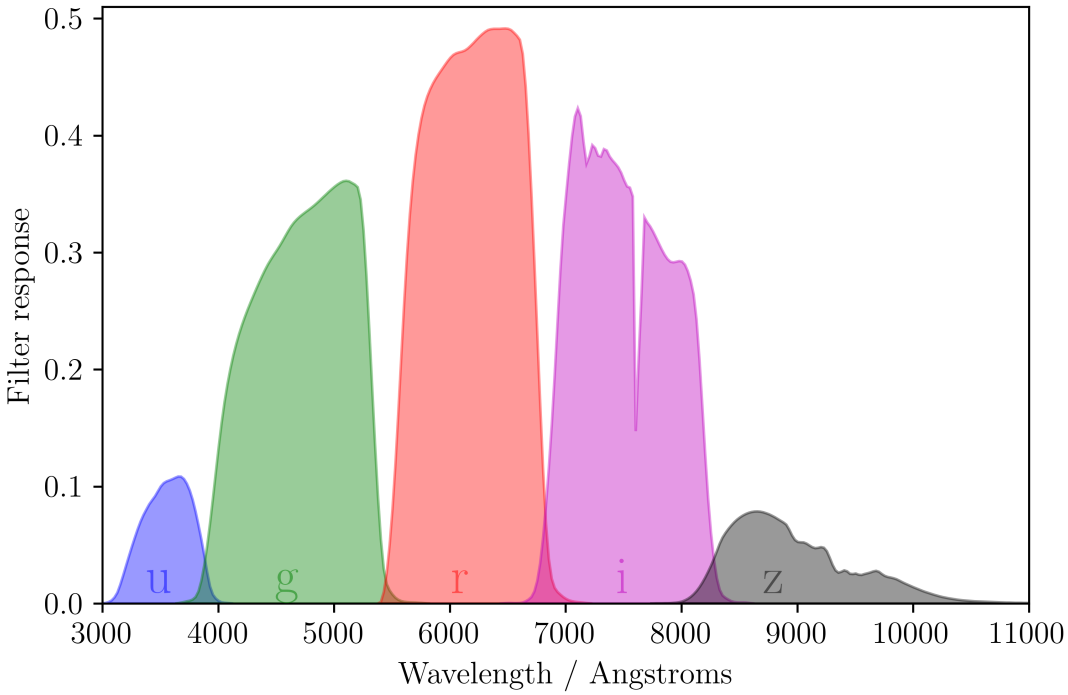

Figure 2.4: SDSS photometric bands u, g, r, i and z.

SDSS data release 18 as the main source of photometry and radius measurements of the optical objects in our catalogs.

2.2.3 NASA/IPAC Extragalactic Database

The NASA/IPAC Extragalactic Database (NED) is an online database of galaxies, quasars, radio sources and other extragalactic objects. It was founded in the late 1980s, currently funded by NASA and operated by the Infrared Processing and Analysis Center (IPAC) at Caltech, California, USA. As of March 2024, it contained more than 1.1 billion distinct objects (NASA/IPAC, 2024). It sources any available extragalactic database or catalog the NED team was able to access. This means the data size is huge but at a cost of being very much inhomogeneous (Helou et al., 1991; Cook et al., 2023).

The individual objects in NED are also cross-identified, so it is possible to search for a galaxy using its name in any database it appears in. It further provides coordinates, known redshift measurements from literature, article references and other basic information of the object. I used NED to supplement my data for galaxies, which have been missed by GOLDMine to get an even more complete sample of HI-undetected objects.

2.3 Data extraction techniques

The data from a radio telescope is quite different from the classical optical one, with the radio data cubes having a third (spectral) axis, instead of only right ascension and declination. Therefore specialized source extraction techniques are necessary. Our options are to either observe the data visually or have an

automated program analyze it for us. Both of these approaches come with their pros and cons. In this section I will describe some of these techniques and compare their feasibility, reliability and completeness.

Reliability and completeness have specific meanings in astronomy. Reliability of a data extraction technique is simply the measure of how much of the cataloged objects are actual physical object, instead of contamination by false detection due to noise or RFI artifacts. Completeness determines what percentage of the actual physical sources we detect. For example, if there are 100 physical objects in our studied region of space, but we only catalog the 20 brightest ones, we will get very high reliability but miss the majority of real objects, hence leaving our completeness low. Therefore, we want to utilize such extraction technique, which will help us maximize both. Unfortunately, there is no one single universal approach of identifying and recording HI sources, and it often comes down to a trade off between reliability and completeness. Hence, it is advantageous to have more than one person examining the data. For more information about the completeness vs. reliability issue see Taylor et al. (2013) or Taylor et al. (2014).

Another important part of radio data extraction is assignement of HI detections to their corresponding optical counterparts, which is not as straightforward as it could appear. Arecibo's beam size was 3.5 arcmin, which means the actual galaxy may be as far as 1.75 arcmin from the HI source position, if the galaxy's gas is undisturbed. If the galaxy is undergoing stripping or some other disturbance, the positional discrepancy may be even larger. This becomes more pronounced if the detection is weak. Known velocity measurements of candidate optical counterparts are often decisive in case they match the velocity measured in the HI data. In the case of faint (or otherwise uncertain) HI detections, we often rely on the optical data for verification. For example if a bright source is visible near the HI coordinates, especially if it has a matching optical redshift to the HI, the validity of the HI signal is much more likely to be real. However we do not rely on the optical emission entirely as this would bias the results of the survey. Indeed, as discussed in section 1.4.1, many HI features are known which do not have an optical counterpart at all.

2.3.1 Visual data extraction

Visual extraction methods offer complete control over the majority of the cataloging process, while at the same time allowing a very detailed inspection of the data. The reason visual methods are usually preferred is also its simplicity, in contrast to the automated extraction techniques, because designing a good and reliable automated algorithm is very difficult and requires a lot of testing. Visual methods obviously take advantage of the human eye, which has evolved to pick up on patterns and any inconsistencies in noise (e.g. allowing us to notice a predator in the distance). This means that visual inspection achieves a high level of reliability with a reasonable completeness. In practice it is standard procedure to either use visual methods entirely or at least to check and verify the sources detected by automated methods, since their reliability can often be significantly lower (Taylor et al., 2013). Visual inspection and analysis of HI data cubes requires specialist software, some of which is described below.

kvis

`kvis` comes as a part of the Karma package for Linux and it is a quick and easy way to view radio data cubes. The user can select whether they wish to view the data in any of the major orthogonal projections, that is RA/Dec (XY), RA/Velocity (XZ) or Dec/Velocity (ZY). It is also useful for overlaying contours of the data, masking the data, adding annotations and simple spectral line analysis (Gooch, 1996). However, it lacks any cataloging features. That means when creating a catalog of HI sources in a data cube the user has to record the coordinates manually, which is of course prone to typos and errors. While the user does have the ability, in combination with `Miriad` (described below in subsection 2.3.3), to mask the recorded source so as to not record it accidentally twice, it is extremely time consuming and not straightforward. This whole process should ideally be then repeated by one or two more persons to ensure the completeness and reliability of the new catalog. All of this makes any cataloging very time demanding and impractical for anything but small surveys.

Due to the lack of a better alternative at that time though, `kvis` was used to catalog the HI sources analyzed in the early AGES papers, e.g. Auld et al. (2006) through Taylor et al. (2013). These difficulties were a motivation for development of a custom-made interactive data visualization, extraction and analysis program named `FRELLED`.

FRELLED

FITS Realtime Explorer of Low Latency in Every Dimension (`FRELLED`) was developed by Taylor (2015) and its final version is now available online, Taylor (2024) in preparation. The latest version 5, which was used for this work, is a set of `Python 3` scripts run inside `Blender 2.79b`. The general idea behind `FRELLED` was to address speed and ease of cataloging, because in `kvis` it was not difficult to identify an HI detection ($\ll$ 1 s) in the data cube but only to record it. It has since become a standard HI source extraction method for AGES and WAVES analysis, e.g. Taylor et al. (2022); Deshev et al. (2022); Taylor et al. (2020).

As with `kvis`, `FRELLED` can show data in the various projections (XY, XZ or ZY) as 2D image slices, but it can also render the whole 3D data cube in real time. The full volumetric 3D display is especially convenient at the start of the cataloging process to quickly record the brightest HI sources, while the 2D mode is more useful to show the fainter detections. After identifying an HI source, the user is then able to interactively define a region fully encompassing it, which holds its exact coordinates and velocity width. This region acts as a mask to prevent the user from re-detecting a source but the visibility of the mask can be interactively controlled and/or disabled. This makes cataloging using `FRELLED` as much as 50 times faster than other viewers (Taylor, 2015).

`FRELLED` allows user to compare the HI detections with other wavelength data, such as optical information from the SDSS and NED, which is useful when assigning the optical counterparts to HI detections. I used `FRELLED` for cataloging the HI sources, constructing various contour plots of the sources, including integrated flux (moment 0) maps but also more advanced visualization methods needed for some of the more complex radio data.

Presenting data cubes, which are fundamentally three-dimensional, is difficult

in a traditional two-dimensional article. One method is to plot contours for every single spectral channel (i.e. a series of "channel maps"), a widely-used technique but which requires a great deal of space. A popular alternative in radio astronomy are "renzograms". These present the same information as in standard channel maps but condensed into a single image. In a renzogram, one plots only a single contour per spectral channel, colored according to velocity. In this way all the major features of the three-dimensional data can be effectively captured in a single two-dimensional image. Examples are shown in figure 2.5. The renzograms shown in this work always have an RA axis in HH:MM:SS and declination in DD:MM:SS.

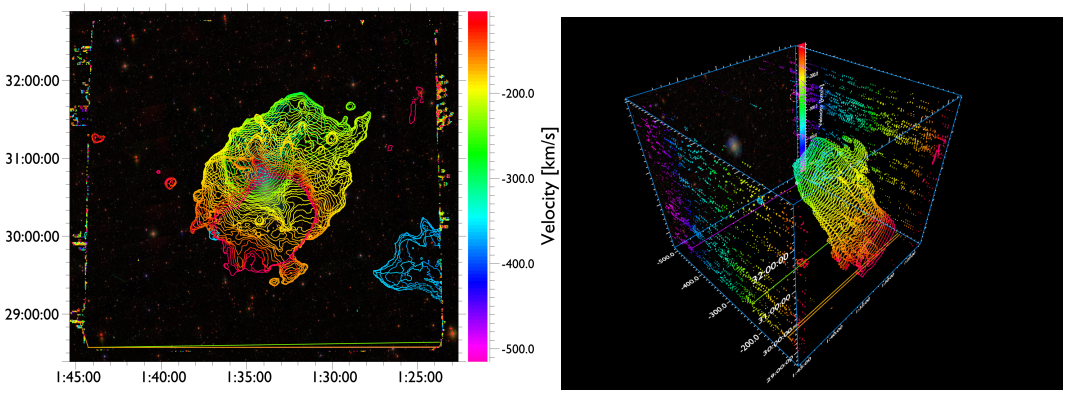

(a) (b)

Figure 2.5: (a) An example of a renzogram of galaxy M33. We can clearly see extensions and shape of the HI gas in the RA/Dec/velocity space. (b) Side-view of the data shows each velocity channel with differently colored contours. The green circle in the corner shows the 3.5 arcmin beam size. Both using the flux data cube shown using `FRELLED`, courtesy of Rhys Taylor.

One more important feature `FRELLED` has is its capability to access `Miriad`, described below in subsection 2.3.3, which allows immediate analysis of the cataloged HI sources.

2.3.2 Automatic data extraction

Automatic extraction programs, such as `SoFIA` by Serra et al. (2015), `Duchamp` by Whiting (2012) or `GLaDOS`, which was used in (Taylor et al., 2012) and Taylor et al. (2013), offer an alternative to visual extraction techniques, with the principle advantage being they are much faster to run than a visual search. The user provides the `.fits` data cube and parameters of expected HI sources, such as its S/N ratio and velocity width and runs the program. The program's algorithm then compiles its own catalog of candidate sources and then the user has to visually inspect the candidates to either accept or reject the detections. Alternatively, if the algorithm is sophisticated enough, for example based on Fourier-space matched-filtering and using templates of expected HI sources shapes, it then may not require much more interaction (for more see Saintonge 2007).

Ideally, we would only use automatic extraction algorithms due to their homogeneity, objectivity and repeatability, while also possibly reaching theoretically high completeness. They are also beneficial in case of large studies, where the

surveyed area is too large and visual methods are unpractical, like the ALFALFA survey done by Giovanelli et al. (2005). In practice these advantages are often outweighed by other factors. They are often unreliable, have poor performance in the regions affected by RFI and suffer from low completeness at low S/N values. This is important, because HI sources with low S/N are often very interesting, as they can be HI clouds or debris from galactic processes like RPS or tidal interactions. Therefore visual extraction techniques are still preferred for their robustness for AGES, WAVES and many other data sets.

All these reasons mean that for relatively small AGES and WAVES data sets, visual inspection has been the main source extraction method. Automatic techniques are of course indispensable for larger data sets, however for our purposes we use them in a more supplementary fashion: they are valuable for providing independent confirmation of visually-determined sources, but while they do usually increase our completeness levels, this is usually only to a very modest extent (Taylor et al., 2013).

GLADOS

Galaxy Line Analysis for Detection Of Sources (`GLADOS`) has been specifically developed for use with the AGES data in VC1 and VC2 regions. It is optimized for use of two `.fits` data cubes of the same region but with different polarizations. This because the HI signal is not polarized, so it should appear in both cubes with the same intensity, while the noise spike in one polarization should not appear in the other.

Unfortunately, the data of the individual polarizations required for `GLADOS` was not available for this project. However it was shown in Taylor et al. (2013) and Deshev et al. (2022) that the rate of additional detections from `GLADOS` is typically small, only a few percent of the number of visual identifications. Therefore, while `GLADOS` (or other automatic search method) may well find some individually-interesting detections, it is extremely unlikely that the result would change any of the overall statistical findings of the study, and I leave an automatic search to a future work.

2.3.3 Measurements of HI sources

Miriad

`Miriad` is a well-established radio astronomy tool for data reduction and spectral line analysis. Apart from being able to manipulate (make slices or regions of the data cube), it can also convert the FITS data cube, into its own `.mir` file format and then perform analysis on it. This is done using the *mbspect* task. The user has to specify coordinates, mask, profile and several other parameters. This can also be done directly in `FRELLED`, which automatically specifies the required input parameters based on the selected region. The following example snippet shows those parameters:

```
#INPUT PARAMETERS
in=WAVES_SE_CleanedFlux.mir
out=
```

```
coord=12:33:38.74,9:11:6.9
width=5
xaxis=
yaxis=point
xrange=300.0,3000.0
yrange=
hann=
order=-1
options=posfit,measure
profile=2063.12,2516.01
mask=2013.12,2566.01
device=/XSERVE
log=VCS_001_log.txt
comment=VCS_001
```

Most importantly, the profile defines the boundaries of the emission line and the flux is calculated between these two points. But if the signal is too strong it may affect the baseline fitting, which is necessary to measure the flux correctly. For that reason the mask is included to "mask out" the portions of the spectrum, which usually include the measured source and/or any other strong signal that may be present. These portions are clipped (ignored) during the baseline fitting. `Miriad` then calculates the HI position (when possible), line widths and total flux in Jy (Sault et al., 1995).

2.3.4 Confirmation of faint HI sources

An important aspect of data extraction is also verification of faint and uncertain sources. In previous AGES observations in case of spurious sources it was possible to perform follow-up observations, but after the Arecibo telescope collapse, it is now much more difficult to confirm the detections. For that reason we have to fall back on other methods, such as comparison of optical data or the 6.5 S/N criterion to confirm a spurious HI source. This is described in Saintonge (2007) and calculated by the equation

$$S/N = \begin{cases} \frac{F/W}{\sigma} \left(\frac{W/2}{10\ \mathrm{kms}^{-1}}\right)^{\frac{1}{2}}, W < 400\ \mathrm{kms}^{-1}, \\ \frac{F/W}{\sigma} \left(\frac{400\ \mathrm{kms}^{-1}/2}{10\ \mathrm{kms}^{-1}}\right)^{\frac{1}{2}}, W \geq 400\ \mathrm{kms}^{-1}, \end{cases} \tag{2.2}$$

where F is the integrated flux in mJy kms^{-1}, W is the line width of the HI source in kms^{-1} and σ is the rms noise in mJy. This criterion has been widely used in the AGES and ALFALFA studies.

3. Results

3.1 Catalog of HI sources

For the analysis of the WAVES region I first used `Miriad` to truncate the data cubes to the velocity range of $300 - 3000$ kms^{-1}. Below ~ 300 kms^{-1} the data is subjected to strong Milky Way emission and above ~ 3000 kms^{-1} the galaxies have too high velocities to be considered Virgo Cluster members (Binggeli et al., 1993). Next, I converted the flux data cubes into S/N cubes, by dividing along each spectral axis by its rms value. This was done because it normalizes the rms, and the uniform levels make the data cubes easier to visualize (Taylor et al., 2014). This is particularly important because, as illustrated in figure 3.1, the non-uniform noise levels would otherwise make the edges of the data appear much brighter and thus obscure the interior parts of the data where the rms is lower. This effect is also visible in figure 2.5, around the edges of the flux data cube.

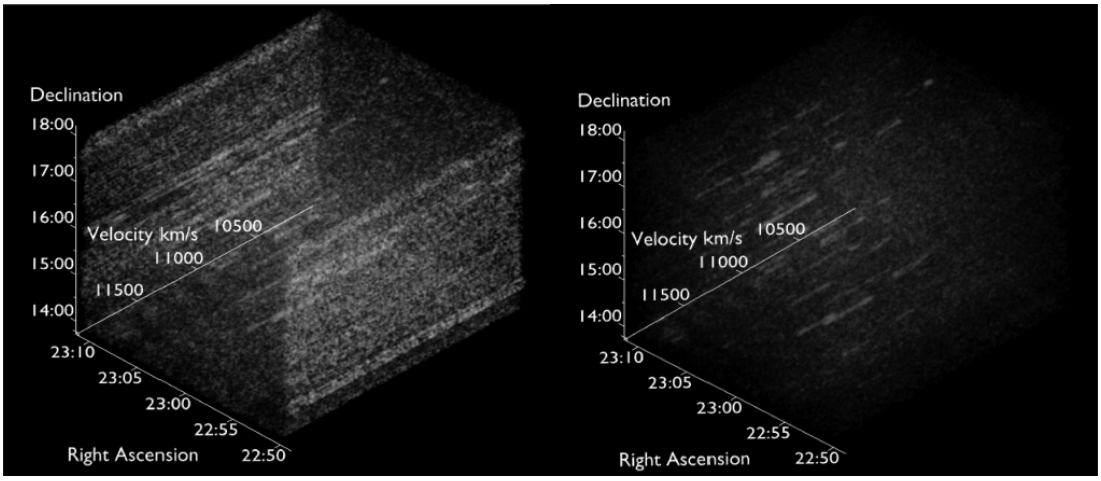

Figure 3.1: Visualization effect of converting the flux (left) data cube into S/N (right). Credit: Taylor et al. (2014)

I cataloged the HI sources in the WAVES region using `FRELLED`. First I started with the VSE data cube in the 3D view for the brightest sources, as shown in figure 3.2, and then 2D view, figure 3.3, in the XZ projection for the fainter ones. In the 3D view, the brightest HI sources are typically visible as cylindrical-shaped objects, which are easily distinguished from the noise, but identifying the HI sources in the 2D view is slightly different. In general this is done by inspecting the XZ projections composed of RA/Velocity data slices at a constant declination and noticing the brightness and number of pixels of data, and also its coherence over multiple different declination channels (usually at least 4 or 5). This indicates the detection is not just variation in noise, which normally does not span more than 1 or 2 channels, but rather a real source. For this I also utilized my prior training by visually inspecting data cubes, which were already fully cataloged.

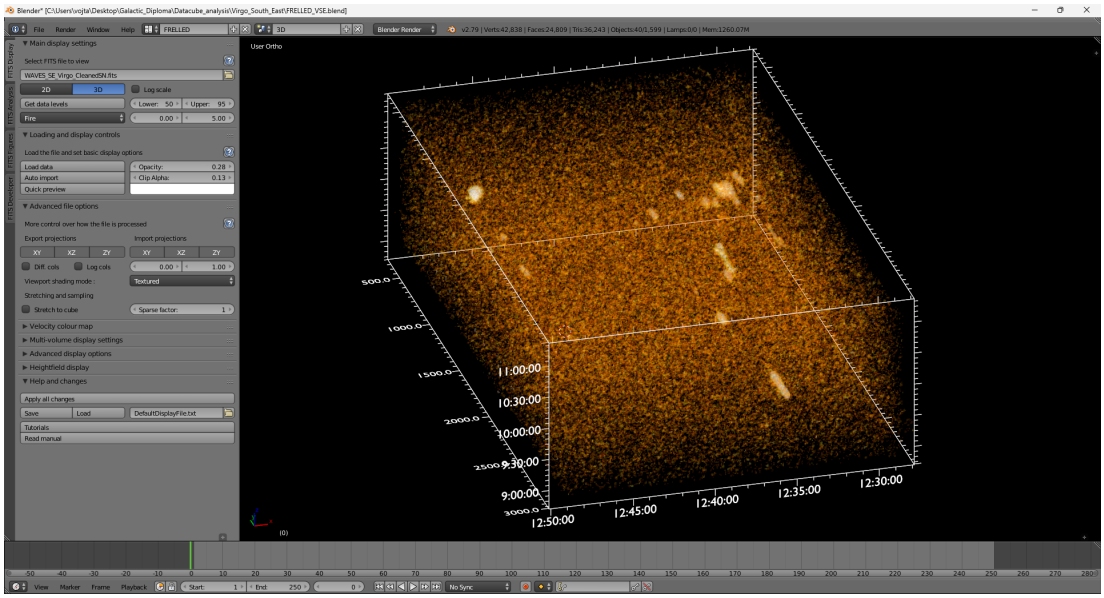

Figure 3.2: 3D view of the VSE data cube in FRELLED at the start of the cataloging process with no assigned regions yet. Note the cylindrical-shaped objects, mainly in the right part of the cube, show the brightest HI sources. Axes are RA, declination in sexagesimal degrees and velocity in kms^{-1}.

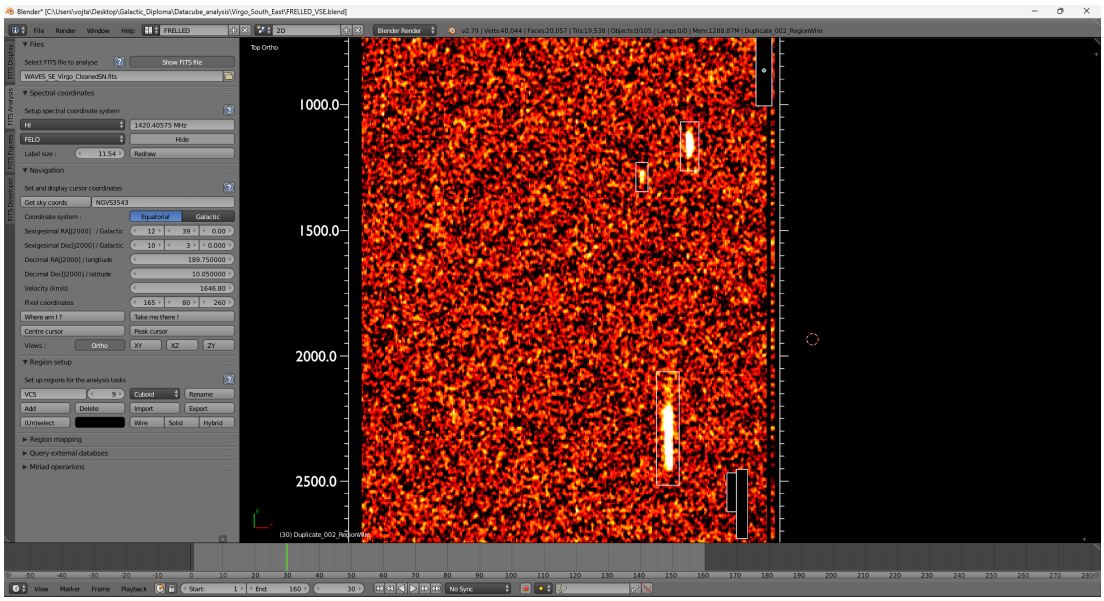

Figure 3.3: 2D view of the VSE data cube in FRELLED with some already assigned regions for the HI sources. Note the three masked regions (black rectangles) in the right upper and lower corners, and also the unmasked regions showing the typical appearance of an HI source. Axes are RA, velocity in kms^{-1} and the horizontal slider at the bottom of the figure operates the declination channel.

With this procedure I detected 23 HI sources in VSE, which includes the ALFALFA Virgo 7 complex (counted as four sources due to its irregular shape, see section 1.4.1). I repeated this process with the VSW data cube which I found contained 32 HI detections. In total I recorded 55 Virgo Cluster South (VCS) objects in the entire WAVES data region.

Next, I processed the detections using `Miriad` to measure their systemic velocities, line widths, fluxes and perform exact position fitting, where possible. For this I used the WAVES flux data cube with the velocity range from 300 kms^{-1} to 3000 kms^{-1}. If the position fitting failed, the coordinates used were reverted back to the initial ones (i.e. the initial by-eye guess). This only occurred for 4 sources: VCS 20 (AV7), VCS 36, VCS 38 and VCS 55. Some selected examples of spectra are shown in figure 3.4. The full set of spectra are in attachment A.1.

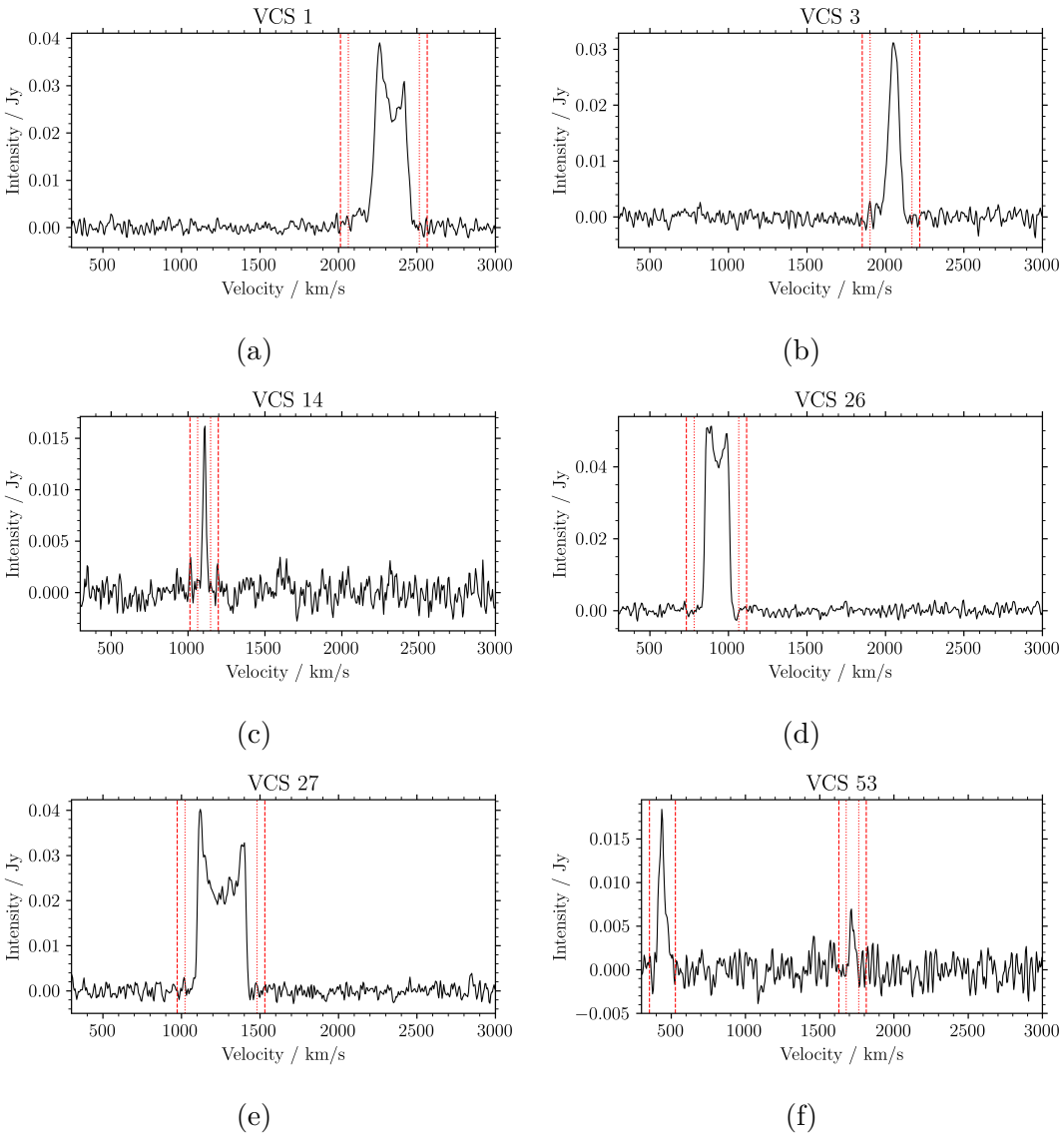

Figure 3.4: Selection of HI spectra of the VCS objects. The red dotted line represents the line profile in which the flux is measured. The red dashed line is the applied masking, in order not to affect the baseline fitting. The horizontal axis range corresponds to the data cube velocity range. Note: In (a), (d) and (e) we can see the characteristic double-horn profile caused by the galaxy's rotation.

In order to calculate the HI mass of the sources, using equation 1.5, it was also necessary to determine the distance of the objects. This was done by creating a spatial scatter plot of the Virgo Cluster objects using the GOLDMine catalog with an auxiliary axis color-coded by distance (17, 23 or 32 Mpc), see figure

3.5. VCS objects were then added (not shown in fig. 3.5) and based on their position within each individual structure their distances were assigned. Naturally, some objects were positioned on the borders of these structure, making their assignement to particular substructures more uncertain. In those cases their HI velocity measurements were also taken into account. For more details see section 2.2.1 in Gavazzi et al. (1999) and Taylor et al. (2012). In summary there are 31 HI detections at 17 Mpc (56.4% of the sample), 20 at 23 Mpc (36.3%) and 4 at 32 Mpc (7.3%).

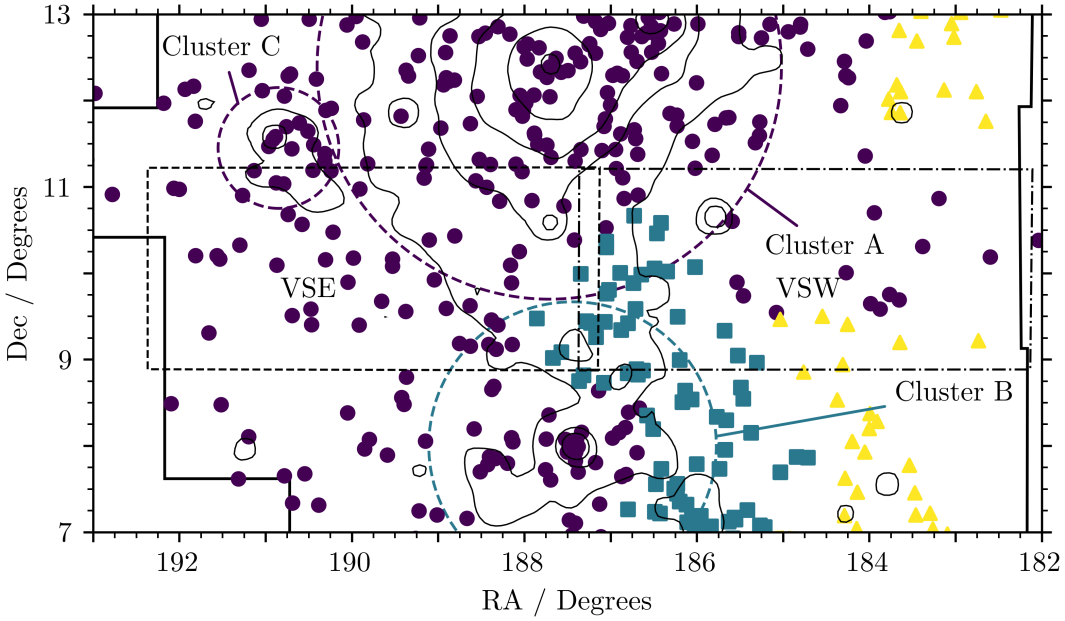

Figure 3.5: Plot of GOLDMine objects in the Virgo Cluster colored by their distance. Purple points = 17 Mpc, blue squares = 23 Mpc, yellow triangles = 32 Mpc.

With this complete, I generated 3.5 σ renzograms in `FRELLED` for each VCS object, which were used to search for extensions in the HI. By visually inspecting all 55 VCS renzograms, shown in attachment A.2, I assigned HI feature levels: 0 - distinct tail or extension, 1 - hint of a tail/disturbance, 2 - noisy contours, 3 - normal profile/too weak signal. This is especially useful for discovering environmental effects acting on the galaxies, in particular ongoing gas loss by processes such as ram pressure stripping. See figure 3.6 for examples of the four mentioned levels.

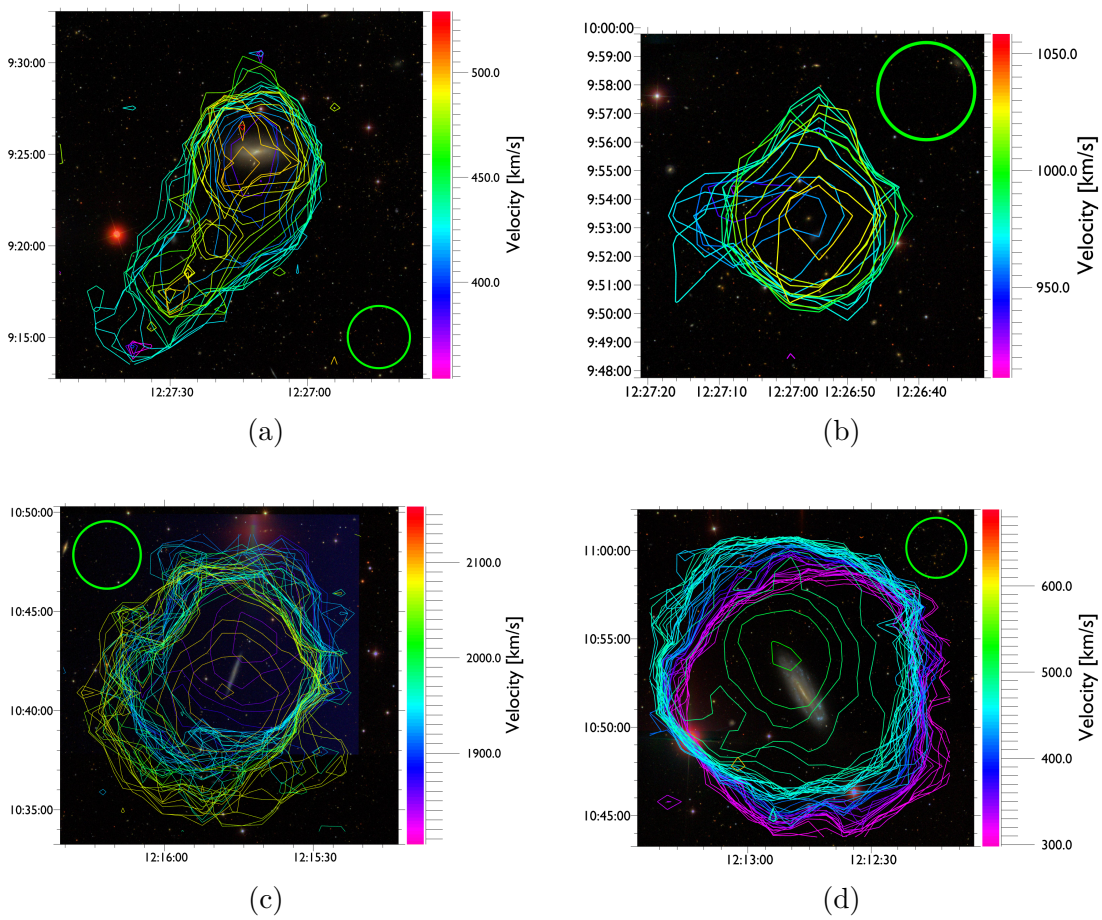

Figure 3.6: Examples of HI features in renzograms: (a) VCS 38, feature level 0 (distinct tail or extension), (b) VCS 40, feature level 1 (hint of a tail/disturbance), (c) VCS 25, feature level 2 (noisy contours) and (d) VCS 35, feature level 3 (normal profile). The green circle in the corner shows the 3.5 arcmin beam size.

The complete VCS catalog with HI velocities, widths, flux, distances, HI mass, features and integrated S/N is shown in table 3.1.

Table 3.1: VCS catalog of HI sources detected in WAVES. Objects with a white background are from VSE, while those with a light gray background are in VSW. Position fitted coordinates of the HI emissions are in J2000. The reverted original coordinates, where position fitting failed, are indicated by an absence of the error brackets. The flux is the total integrated flux of the line. The integrated S/N is calculated using the W50 and equation 2.2. Bracketed values indicate errors as computed by `Miriad`.

Name	RA_{HI} [HH:MM:SS]	Dec_{HI} [DD:MM:SS]	Velocity [kms^{-1}]	W50 [kms^{-1}]	W20 [kms^{-1}]	Flux [Jy]	Dist [Mpc]	M_{HI} [$\log(M_\odot)$]	rms [mJy]	Features	S/N
VCS 1	12:33:37.97(0.7)	+09:10:38.94(10)	2332(2)	205(5)	251(7)	6.517(0.334)	17	8.65	0.7	0	10.4
VCS 2	12:36:38.05(0.9)	+11:11:58.63(15)	2240(3)	288(7)	331(10)	6.278(0.439)	17	8.63	1.9	0	10.9
VCS 3	12:36:10.54(0.7)	+09:54:52.86(10)	2055(2)	73(5)	113(7)	2.222(0.189)	17	8.18	0.8	3	5.2
VCS 4	12:35:13.82(0.7)	+10:26:08.53(10)	1082(2)	82(4)	105(7)	1.153(0.122)	17	7.90	0.8	3	69.4
VCS 5	12:32:32.73(0.7)	+09:10:27.99(10)	1158(2)	69(4)	100(6)	1.793(0.166)	17	8.09	0.8	1	40.4
VCS 6	12:46:08.47(0.8)	+10:09:46.40(11)	1506(2)	50(4)	66(6)	0.767(0.111)	17	7.72	1.0	3	36.0
VCS 7	12:48:00.27(0.9)	+10:58:17.26(10)	1152(2)	56(4)	91(6)	3.715(0.327)	17	8.40	0.9	0	24.3
VCS 8	12:46:14.91(0.8)	+10:11:32.70(13)	1147(4)	37(7)	56(11)	0.493(0.130)	17	7.53	1.6	3	145.4
VCS 9	12:46:41.08(0.9)	+10:21:49.10(14)	1590(3)	29(7)	70(10)	0.359(0.064)	17	7.39	0.7	1	115.6
VCS 10	12:48:40.20(0.8)	+10:44:53.39(11)	1614(3)	41(6)	53(9)	0.264(0.068)	17	7.26	0.8	3	147.8
VCS 11	12:43:18.03(1.4)	+08:55:09.10(14)	1429(3)	25(6)	40(9)	0.465(0.133)	17	7.50	1.9	3	19.6
VCS 12	12:35:01.62(0.8)	+09:10:26.31(15)	1291(3)	50(6)	62(9)	0.29(0.072)	17	7.30	0.8	3	188.0
VCS 13	12:38:07.71(0.8)	+10:09:25.82(24)	1150(2)	25(5)	39(7)	0.23(0.057)	17	7.20	0.8	3	502.2
VCS 14	12:30:34.16(0.9)	+10:15:49.96(11)	1108(2)	23(4)	39(6)	0.349(0.067)	17	7.38	0.8	3	39.9
VCS 15	12:21:28.32(0.8)	+10:29:56.21(13)	997(4)	27(9)	42(13)	0.119(0.052)	17	6.91	0.8	3	98.4
VCS 16	12:28:53.38(0.9)	+09:25:02.11(11)	1055(3)	104(6)	116(8)	0.697(0.115)	23	7.94	0.9	3	24.6
VCS 17	12:34:30.30(0.7)	+09:09:12.10(10)	448(2)	89(4)	111(7)	1.36(0.132)	17	7.97	0.8	1	35.6
VCS 18	12:29:41.16(0.7)	+09:42:45.05(10)	538(2)	123(4)	143(6)	1.325(0.113)	23	8.22	0.6	0	40.3
VCS 19	12:31:25.69(0.7)	+09:18:49.68(10)	485(3)	60(6)	104(9)	0.945(0.103)	23	8.07	0.7	0	178.3
VCS 20	12:30:30.11	+09:31:23.83	499(8)	98(15)	322(23)	1.51(0.148)	23	8.28	0.9	0	72.7
VCS 21	12:31:18.95(0.7)	+09:28:36.61(11)	606(3)	52(6)	86(9)	0.826(0.116)	23	8.01	1.0	0	24.3
VCS 22	12:29:23.35(1.0)	+09:57:56.14(19)	792(10)	93(20)	164(30)	0.487(0.120)	23	7.78	1.0	3	11.5

Table 3.1 continued from previous page

Name	RA_{HI} [HH:MM:SS]	Dec_{HI} [DD:MM:SS]	Velocity [kms^{-1}]	W50 [kms^{-1}]	W20 [kms^{-1}]	Flux [Jy]	Dist [Mpc]	M_{HI} [$log(M_{\odot})$]	*rms* [mJy]	Features	S/N
VCS 23	12:40:02.25(0.8)	+09:25:38.85(12)	1394(4)	50(8)	69(12)	0.188(0.056)	17	7.11	0.7	3	6.4
VCS 24	12:45:09.04(0.8)	+10:19:49.60(24)	2204	45	96	0.177(0.065)	17	0.8	7.08	1	99.9
VCS 25	12:15:45.26(0.7)	+10:42:01.18(10)	1985(1)	209(3)	226(4)	12.678(0.616)	17	8.94	1.1	2	127.2
VCS 26	12:27:21.47(0.7)	+10:52:06.19(10)	929(1)	159(3)	173(4)	7.42(0.393)	17	8.70	0.7	2	177.0
VCS 27	12:22:41.98(0.7)	+09:20:07.34(10)	1257(1)	309(3)	324(4)	8.178(0.400)	23	9.01	0.9	1	44.3
VCS 28	12:25:50.11(0.7)	+10:27:42.02(10)	1105(2)	127(3)	148(5)	5.961(0.369)	23	8.87	0.8	0	4.9
VCS 29	12:15:30.35(0.7)	+09:34:56.39(10)	600(2)	200(4)	225(6)	5.602(0.307)	17	8.58	0.9	0	6.1
VCS 30	12:14:35.53(0.7)	+09:11:54.71(10)	1794(1)	123(3)	139(4)	3.963(0.256)	32	8.98	0.8	3	7.4
VCS 31	12:10:56.96(0.7)	+09:13:14.55(10)	2246(2)	130(4)	145(7)	1.466(0.149)	32	8.55	0.9	3	123.3
VCS 32	12:12:00.70(0.7)	+10:23:59.49(10)	1636(2)	77(4)	91(5)	0.988(0.105)	17	7.83	0.7	3	21.3
VCS 33	12:17:03.94(0.7)	+10:00:15.74(10)	1188(2)	57(3)	77(5)	3.866(0.340)	17	8.42	0.9	2	11.5
VCS 34	12:15:54.81(0.7)	+09:39:07.21(10)	2226(1)	26(3)	40(4)	4.036(0.516)	17	8.44	1.0	3	8.5
VCS 35	12:12:45.92(0.7)	+10:52:15.04(10)	384(2)	248(4)	282(6)	24.76(1.079)	17	9.23	0.7	3	25.5
VCS 36	12:26:41.14	+08:56:59.9	1278(2)	84(3)	102(5)	4.133(0.323)	23	8.71	1.2	1	32.7
VCS 37	12:28:40.79(0.7)	+09:15:40.38(10)	866(2)	209(5)	228(7)	2.322(0.185)	23	8.46	0.9	3	20.8
VCS 38	12:27:15.51	+09:22:51.85	439(2)	58(5)	97(7)	2.128(0.197)	23	8.42	0.9	0	3.9
VCS 39	12:25:22.12(0.7)	+10:00:58.12(10)	970(2)	271(5)	291(7)	2.38(0.176)	23	8.47	0.8	0	11.3
VCS 40	12:26:56.29(0.7)	+09:53:19.12(10)	990(2)	51(5)	83(7)	1.133(0.124)	23	8.15	0.8	1	11.3
VCS 41	12:15:04.23(0.7)	+09:45:25.18(10)	2199(2)	109(4)	124(6)	1.238(0.128)	17	7.93	0.8	3	60.3
VCS 42	12:19:00.59(0.9)	+08:55:12.52(13)	2468(3)	162(6)	181(8)	2.098(0.238)	32	8.71	1.5	1	12.9
VCS 43	12:16:32.79(0.7)	+10:12:35.29(10)	2072(2)	55(5)	75(7)	0.847(0.117)	17	7.76	1.0	3	17.0
VCS 44	12:14:12.60(0.7)	+08:52:35.17(21)	1934(2)	84(4)	99(7)	3.291(0.431)	32	8.90	3.3	3	7.2
VCS 45	12:15:28.05(0.7)	+10:30:33.66(10)	2000(3)	53(6)	91(9)	0.746(0.091)	17	7.71	0.7	0	33.1
VCS 46	12:21:11.72(0.7)	+10:37:45.63(10)	2613(2)	39(5)	57(7)	0.464(0.078)	17	7.50	0.8	3	12.8
VCS 47	12:10:23.27(0.7)	+10:11:35.90(11)	502(3)	82(6)	91(10)	0.591(0.148)	17	7.61	1.4	1	20.3

Table 3.1 continued from previous page

Name	RA_{HI} [HH:MM:SS]	Dec_{HI} [DD:MM:SS]	Velocity [kms^{-1}]	W50 [kms^{-1}]	W20 [kms^{-1}]	Flux [Jy]	Dist [Mpc]	M_{HI} [$log(M_{\odot})$]	rms [mJy]	Features	S/N
VCS 48	12:22:04.76(0.7)	+09:02:43.90(10)	1053(4)	310(7)	324(11)	1.545(0.194)	23	8.29	1.0	3	31.9
VCS 49	12:25:35.04(1.0)	+10:35:44.89(14)	1719(5)	24(10)	56(16)	0.075(0.035)	23	6.97	0.7	3	43.5
VCS 50	12:28:15.91(0.7)	+09:26:17.87(12)	431(5)	101(9)	124(14)	0.517(0.107)	23	7.81	0.9	3	44.5
VCS 51	12:23:33.63(1.0)	+09:31:22.70(15)	964(4)	24(8)	34(13)	0.137(0.072)	23	7.23	1.2	3	39.0
VCS 52	12:27:35.71(1.0)	+10:00:20.76(11)	881(3)	51(7)	61(10)	0.215(0.078)	23	7.43	1.1	3	37.9
VCS 53	12:27:29.20(0.9)	+09:20:10.40(13)	1719(5)	33(10)	55(16)	0.208(0.080)	23	7.41	1.1	3	25.6
VCS 54	12:27:35.73(0.9)	+09:51:33.31(16)	954(6)	68(11)	85(17)	0.292(0.099)	23	7.56	1.0	3	84.0
VCS 55	12:25:32.53	+11:10:45.88	903(4)	85(9)	92(13)	0.39(0.200)	17	7.42	2.4	3	7.9

Once I completed this initial inspection, the masked cube was given to R. Taylor for additional visual search for potentially missed sources, which is a common practice for AGES and WAVES studies, as mentioned in section 2.3. This resulted in a small number (12) of additional candidate detections, but all of these were marginal with low integrated S/N. With one exception (VCS 15), all were without optical counterparts. The table of these potential sources is in attachment table A.3. Only one object (VCS 15) was accepted as a real source, mainly thanks to its relatively high peak and integrated S/N and presence of an optical counterpart VCC 476.

Next, I visually assigned optical counterparts to the HI sources (for full discussion of the optical parameters see section 3.3). This was done by examining the HI coordinates in the optical image using the SDSS visual tools. If there was an object visible within 1.75 arcminutes (half the WAVES beam), which could have been anything from a bright spiral to a faint blue irregular blob, I queried its velocity in NED. If its velocity matched the HI velocity from WAVES, it was assigned confidence level 0 (almost certainly associated with the HI). If a possible optical counterpart was present, but had no previous velocity measurement, its confidence level was 1. If there were multiple possible objects without a velocity measurement or there was no object at all, as in the case of gas clouds, I assigned confidence level 2.

While the VCC provides a convenient source of homogeneous morphological classification, not all HI detections here have galaxies listen in the VCC. I therefore decided to use the VCC morphology wherever available but supplemented this with my own visual classification (using the SDSS images) for non-VCC objects. This approach is consistent with Taylor et al. (2012). For simplicity, I only assigned 4 possible types for the manual classification: lenticular (1), elliptical (0) and spiral (5) and irregular (12), as shown in table 1.1. This applied for 10 VCS objects.

The VCS catalog with the assigned optical counterparts and coordinates, morphological types and HI extension confidence levels are shown in table 3.2

Table 3.2: VCS catalog with optical properties. VCS objects are shown with their common catalog (CC) names, where available. RA_{opt} and Dec_{opt} are coordinates of the optical counterparts as given by the SDSS. Objects with a forward slash (/) indicate pairs of galaxies with indistinguishable HI emission. "Type" indicates morphology according to table 1.1, taken from the VCC, unless specified otherwise. Pairs of galaxies cannot be assigned a single morphology so for those objects the parameter is left blank.

Name	CC name	RA_{opt} [HH:MM:SS]	Dec_{opt} [DD:MM:SS]	Type	Conf. level
VCS 1	VCC 1516	12:33:39.71	+09:10:30.1	6	0
VCS 2	VCC 1676/1673	12:36:32.70	+11:15:28.7	–	0
VCS 3	VCC 1654	12:36:10.58	+09:55:21.2	12	0
VCS 4	VCC 1605	12:35:13.91	+10:25:53.3	9	0
VCS 5	VCC 1437	12:32:33.50	+09:10:25.2	17	0
VCS 6	VCC 2034	12:46:08.04	+10:09:45.1	12	0
VCS 7	VCC 2062/2066	12:47:59.92	+10:58:14.9	–	0
VCS 8	VCC 2037	12:46:15.31	+10:12:26.6	16	0

Table 3.2 continued from previous page

Name	CC name	RA_{opt} [HH:MM:SS]	Dec_{opt} [DD:MM:SS]	Type	Conf. level
VCS 9	AGC 226178	12:46:43.99	+10:22:28.5	–[1]	2
VCS 10	–[3]	12:48:40.34	+10:44:15.8	12	1
VCS 11	VCC 1964	12:43:18.12	+08:55:18.8	-1	2
VCS 12	VCC 1596	12:35:00.96	+09:11:09.9	12	0
VCS 13	VCC 1744	12:38:06.89	+10:09:56.0	17	0
VCS 14	VCC 1295	12:30:32.30	+10:15:40.5	20	0
VCS 15	VCC 476	12:21:28.92	+10:29:08.7	12	1
VCS 16	VCC 1141	12:28:54.95	+09:25:16.0	17	0
VCS 17	VCC 1566	12:34:30.99	+09:09:20.1	9	0
VCS 18	AV7[12]	12:29:41.16	+09:42:45.05	–	2
VCS 19	AV7[12]	12:31:25.69	+09:18:49.68	–	2
VCS 20	AV7[12]	12:30:30.11	+09:31:23.83	–	2
VCS 21	AV7[12]	12:31:18.95	+09:28:36.61	–	2
VCS 22	VCC 1179	12:29:22.66	+09:59:17.8	16	0
VCS 23	–[3]	12:40:03.09	+09:24:49.0	12	1
VCS 24	VCC 2015	12:45:11.83	+10:19:27.5	17	0
VCS 25	VCC 162	12:15:46.27	+10:41:57.4	9	0
VCS 26	VCC 995	12:27:22.28	+10:52:00.6	7	0
VCS 27	VCC 576	12:22:42.24	+09:19:56.9	6	0
VCS 28	VCC 849	12:25:50.67	+10:27:32.6	6	0
VCS 29	VCC 152	12:15:30.51	+09:35:05.6	8	0
VCS 30	VCC 117	12:14:35.67	+09:11:59.2	12	0
VCS 31	VCC 31	12:10:57.10	+09:13:09.9	20	0
VCS 32	VCCA 46[3]	12:12:01.21	+10:23:54.4	5	0
VCS 33	VCC 217	12:17:04.23	+10:00:20.1	12	0
VCS 34	VCC 169	12:15:56.32	+09:38:57.6	12	0
VCS 35	VCC 66	12:12:46.33	+10:51:54.9	7	0
VCS 36	VCC 905/939	12:26:38.68	+08:52:30.1	–	0
VCS 37	VCC 1118	12:28:40.52	+09:15:34.1	7	0
VCS 38	VCC 979	12:27:11.84	+09:25:12.3	3	0
VCS 39	VCC 792	12:25:22.16	+10:01:00.5	4	0
VCS 40	VCC 952	12:26:55.72	+09:52:56.0	12	0
VCS 41	VCC 130	12:15:04.01	+09:45:13.2	17	0
VCS 42	VCC 318	12:19:03.84	+08:51:29.1	8	0
VCS 43	VCCA 59[3]	12:16:34.03	+10:12:22.8	12	0
VCS 44	VCCA 52[3]	12:14:13.79	+08:54:29.8	5	0
VCS 45	VCCA 56[3]	12:15:27.33	+10:30:44.4	12	0
VCS 46	VCCA 79[3]	12:21:13.23	+10:37:32.0	12	0
VCS 47	VCC 21	12:10:23.09	+10:11:18.8	-3	0
VCS 48	VCC 524	12:22:05.67	+09:02:37.0	6	0
VCS 49	VCC 825	12:25:39.34	+10:35:02.0	12	0
VCS 50	VCC 1086	12:28:15.93	+09:26:10.7	18	0
VCS 51	VCC 651	12:23:34.53	+09:30:54.9	-1	1
VCS 52	VCC 1021	12:27:33.48	+10:00:13.5	12	0
VCS 53	VCC 1013	12:27:30.16	+09:20:28.9	12	0

Table 3.2 continued from previous page

Name	CC name	RA_{opt} [HH:MM:SS]	Dec_{opt} [DD:MM:SS]	Type	Conf. level
VCS 54	–[4]	12:27:35.73	+09:51:33.31	–	2
VCS 55	VCCA 31[3]	12:25:31.46	+11:09:29.8	12	0

In total the VCS catalog includes 3 early-type galaxies, 45 late-type galaxies, 3 pairs of galaxies with unresolvable HI content, 1 previously unknown dark cloud (VCS 54), the ALFALFA Virgo 7 complex and 1 gas cloud with detected star formation (VCS 9). The latter is a special case, see section 3.6.

[1]Objects with ambiguous optical counterparts or star-forming clouds. Their listed coordinates are the HI coordinates, not optical.

[2]AV7 = ALFALFA Virgo 7 complex.

[3]Not a VCC object, its morphological type was assigned manually.

[4]Dark cloud. Listed coordinates are HI, not optical

3.2 Catalog of HI-undetected objects

To understand the processes affecting galaxy evolution (as described in section 1.2) in the WAVES region, it was also necessary to obtain a catalog of galaxies without an HI detection. For this I began with the GOLDMine catalog. First, I selected all the galaxies located in an area slightly larger than the HI data region, described in section 2.1.2, to make sure I include all the possible objects. This initial table numbered 409 entries.

To exclude the background objects I reduced this to objects with velocities less than 3000 kms^{-1}, a well defined upper boundary for Virgo galaxies given by Binggeli et al. (1993). Objects without velocity measurements were excluded. Of the remainder, to ensure only reliable velocity measurements, only those with high quality spectroscopy (quality flag 1, 2 and 3) were included. This reduced the total number of objects to 158. The resulting objects were also cross-matched with the VCS objects' optical coordinates with a 20 arcsec sky separation and any which were present in the VCS were removed. Finally, I trimmed the table according to the proper WAVES boundaries. This gave a final table of 73 HI non-detected VCC galaxies.

In order to achieve as high completeness of the optical catalog as possible, I supplemented this catalog of HI non-detected galaxies with a galactic NED query using the same coordinate and velocity constraints as above. The query returned 240 objects, of which only 113 had a spectroscopic measurement of velocity. The method used for the velocity measurement was given by one of the flags, with descending quality: SPEC (classic spectral lines fitting - high quality spectra), SST (statistically acquired value), SLS (multiple spectral lines fitting), S1L (single spectral line), SUN (unknown spectroscopic method), UUN (unknown method) and PHOT (photometric measurements). The objects with PHOT flag were discarded due to relatively high error given by photometric measurements. The SUN and UUN objects were slightly more complicated, because they were often big, bright and well known galaxies, whose velocity was in fact well known. However after closer inspection, I found that all of these objects were already present either in the GOLDMine or the VCS catalogs.

Due to its automated nature, some of the objects returned by the NED query were not necessarily galaxies and/or had poor photometric data, e.g. image artifacts, galaxies with a obscuring foreground star, etc. In order to filter these out I inspected the SDSS optical images of all 113 entries and discarded any unsuitable objects, which brought the number down to 102. Then it was necessary to filter out the VCC, IC and NGC galaxies, which were already included in the GOLDMine catalog. This resulted in 32 objects in the supplementary NED table. After cross-matching with the VCS catalog using the 1.75 arcmin sky separation again, the final number of NED supplementary objects was 13. For these objects I also manually assigned their morphological classifications as discussed in the previous section.

In total, the optical catalog of objects without any HI detection contains 86 objects, of which 73 are VCC and 13 were found from a NED search, and is shown in table 3.2

Table 3.3: The table of optical objects without an HI detection in the WAVES region. 73 objects are taken from the GOLDMine catalog (white background) and 13 objects are from the NED query (light gray background). Coordinates are in J2000. Distance and type is either from the GOLDMine catalog or from manual assignments as discussed earlier.

Object	RA [HH:MM:SS]	Dec [DD:MM:SS]	Vel. [kms^{-1}]	Dist [Mpc]	Type
VCC 1003	12:27:26.50	+11:06:27.0	1130	17	2
VCC 1039	12:27:44.30	+11:12:52.0	1442	17	-1
VCC 1062	12:28:03.90	+09:48:13.0	517	23	1
VCC 1075	12:28:12.30	+10:17:52.0	1844	23	-1
VCC 1076	12:28:12.80	+10:31:34.0	1828	17	-1
VCC 1078	12:28:11.30	+09:45:37.0	475	23	-1
VCC 1079	12:28:12.00	+10:21:55.0	1468	23	-1
VCC 1164	12:29:08.10	+09:26:38.0	1040	23	-1
VCC 1175	12:29:18.20	+10:08:09.0	70	23	0
VCC 118	12:14:36.80	+09:41:22.0	1292	17	-1
VCC 1209	12:29:40.60	+10:23:06.0	1454	17	-1
VCC 1261	12:30:10.30	+10:46:46.0	1850	17	-1
VCC 1273	12:30:16.90	+09:05:06.0	2015	23	12
VCC 1303	12:30:40.60	+09:00:56.0	875	23	1
VCC 1377	12:31:39.00	+10:50:26.0	634	17	12
VCC 1412	12:32:06.20	+11:10:35.0	1342	17	3
VCC 1422	12:32:14.20	+10:15:05.0	1372	17	0
VCC 1444	12:32:35.90	+09:53:11.0	1769	17	-1
VCC 1446	12:32:39.00	+10:05:31.0	2235	17	-1
VCC 1481	12:33:09.00	+10:50:10.0	1957	17	-1
VCC 1488	12:33:13.40	+09:23:50.0	1157	17	0
VCC 1489	12:33:13.80	+10:55:44.0	80	17	-1
VCC 1496	12:33:18.80	+09:07:14.0	1303	17	-1
VCC 1509	12:33:31.60	+09:27:33.0	817	17	-1
VCC 1521	12:33:45.00	+10:59:45.0	1212	17	0
VCC 1549	12:34:14.80	+11:04:18.0	1357	17	-1
VCC 1567	12:34:31.30	+09:37:24.0	1440	17	-2
VCC 1629	12:35:38.00	+09:35:29.0	790	17	-1
VCC 1647	12:35:56.50	+10:56:12.0	86	17	-1
VCC 1661	12:36:24.80	+10:23:05.0	1400	17	-1
VCC 1684	12:36:39.40	+11:06:07.0	694	17	-3
VCC 1704	12:37:09.70	+10:16:20.0	263	17	-1
VCC 1720	12:37:30.50	+09:33:18.0	2284	17	1
VCC 1743	12:38:06.80	+10:04:56.0	1279	17	-1
VCC 1762	12:38:32.20	+10:22:36.0	192	17	-1
VCC 1767	12:38:37.60	+09:40:31.0	1472	17	-1
VCC 1803	12:39:37.70	+10:58:33.0	1336	17	-1
VCC 1813	12:39:55.90	+10:10:34.0	1834	17	3
VCC 1826	12:40:11.20	+09:53:46.0	2033	17	-1
VCC 1857	12:40:53.10	+10:28:34.0	634	17	-1
VCC 1861	12:40:58.50	+11:11:04.0	683	17	-1

Table 3.3 continued from previous page

Object	RA [HH:MM:SS]	Dec [DD:MM:SS]	Vel. [kms^{-1}]	Dist [Mpc]	Type
VCC 1869	12:41:13.30	+10:09:21.0	1864	17	2
VCC 1881	12:41:29.50	+10:45:46.0	138	17	-1
VCC 1891	12:41:48.90	+11:11:29.0	1016	17	-1
VCC 1895	12:41:52.00	+09:24:10.0	1032	17	-1
VCC 1896	12:41:54.60	+09:35:05.0	1731	17	-3
VCC 1919	12:42:18.90	+10:34:04.0	1869	17	-1
VCC 1936	12:42:46.00	+09:30:38.0	985	17	-3
VCC 1948	12:42:58.00	+10:40:55.0	1672	17	-1
VCC 1958	12:43:10.30	+11:02:12.0	1049	17	-1
VCC 1971	12:43:30.90	+11:02:50.0	1376	17	-1
VCC 2000	12:44:32.00	+11:11:26.0	1115	17	0
VCC 2042	12:46:38.40	+09:18:25.0	1765	17	-1
VCC 2048	12:47:15.30	+10:12:12.0	1095	17	-3
VCC 2066	12:48:15.10	+10:59:01.0	1181	17	20
VCC 216	12:17:01.10	+09:24:27.0	1325	23	-1
VCC 227	12:17:14.50	+08:56:32.0	1304	23	10
VCC 275	12:18:11.00	+09:29:59.0	1733	23	12
VCC 394	12:20:08.60	+09:28:05.0	1789	23	-1
VCC 407	12:20:18.80	+09:32:43.0	2078	17	-2
VCC 458	12:21:12.70	+08:57:47.0	1563	23	-1
VCC 504	12:21:50.10	+09:44:21.0	497	17	-1
VCC 529	12:22:08.60	+09:53:40.0	1563	17	-1
VCC 546	12:22:21.60	+10:36:07.0	2067	17	-1
VCC 695	12:24:05.30	+10:04:04.0	1370	23	-1
VCC 698	12:24:05.00	+11:13:05.0	2106	17	1
VCC 747	12:24:47.80	+08:59:29.0	955	23	-1
VCC 756	12:24:53.10	+09:29:37.0	728	23	-1
VCC 856	12:25:57.90	+10:03:14.0	972	23	-1
VCC 920	12:26:34.80	+09:58:54.0	443	23	-1
VCC 931	12:26:44.00	+10:54:17.0	559	17	-1
VCC 944	12:26:50.60	+09:35:03.0	832	23	1
VCC 949	12:26:54.50	+10:39:57.0	1276	23	-1
VCCA 38	12:30:02.62	+09:24:11.9	899	23	-1[2]
WISEA J121341.44+090040.4	12:13:41.43	+09:00:40.3	1801	23	0[2]
WISEA J121443.02+103159.2	12:14:43.04	+10:31:59.1	2086	17	12[2]
WISEA J121453.51+094011.5	12:14:53.53	+09:40:11.8	1707	17	12[2]
WISEA J122020.13+094750.1	12:20:20.14	+09:47:50.2	1189	23	12[2]
WISEA J123955.45+095520.4	12:39:55.46	+09:55:20.7	1434	17	12[2]
WISEA J124533.24+102925.8	12:45:33.30	+10:29:25.7	986	17	0[2]

Table 3.3 continued from previous page

Object	RA [HH:MM:SS]	Dec [DD:MM:SS]	Vel. [kms^{-1}]	Dist [Mpc]	Type
IC 3711	12:44:09.37	+11:10:35.8	1660	17	0[2]
VCC 2012[1]	12:45:05.66	+10:54:03.2	1066	17	-1
IC 3767	12:46:55.48	+10:10:56.7	1245	17	0[2]
SDSS J124101.06+094306.3	12:41:01.07	+09:43:06.3	1361	17	12[2]
VCC 1357[1]	12:31:24.42	+09:28:28.0	607	23	12
VCC 1804[1]	12:39:40.14	+09:23:55.8	1884	17	16

In total in WAVES South field, there are 72 early-type galaxies and 14 late-type galaxies without a detectable HI content. 62 of these objects are at a distance of 17 Mpc (72.1% of the sample), 19 are at 23 Mpc (22.1%) and only 5 are at 32 Mpc (5.8%).

3.3 Optical parameters

The process of acquiring the photometry and radius measurements was similar for both the VCS and the optical catalog. In the VCS, a few cases do not have optical counterparts and therefore no optical parameters can be measured, specifically VCS 9, VCS 18–21 (ALFALFA Virgo 7 complex) and VCS 54. There were also three pairs of galaxies with a seemingly common and/or indistinguishable HI emission (VCS 2, VCS 7 and VCS 36). This was either because they are interacting and exchanging gas or we are simply not able to resolve the HI emission due to their proximity. That made them unsuitable for studying how the relation between the HI and optical components is affected by environment. Hence, I discarded them as well, bringing the total number of VCS objects with optical parameter measurements to 46. 28 of these objects were at a distance of 17 Mpc (60.9% of this refined sample), 14 were at 23 Mpc (30.4%) and 4 at 32 Mpc (8.7%).

The extraction of the data from the SDSS database itself was not straightforward, since the SDSS does not reliably accept the common object names as an input. Instead, I used the coordinates to return the closest object with the type "galaxy" for each of the VCS and optical entries. For photometry I used the g and i bands for the magnitudes and the Petrosian radius, which contains 90% of the g-band luminosity (R_{P90}), to be consistent with a similar analysis done by Deshev et al. (2022). The query however sometimes returned measurements which were obviously not the correct galaxy, but rather some other galactic object located closer to the provided coordinates. For example, while typically the R_{P90} values exceed 10", a few cases returned values of the implausibly low 1" (0.08 kpc at 17 Mpc distance).

In order to correct these false results, I identified all the suspicious objects with $R_{P90} \lesssim$ 10", added them in a separate list and ran another query, which returned all the galactic objects within 1 arcmin of their coordinates. I then

[1]Despite being present in the GOLDMine catalog, these objects were initially discarded due to low quality flags (larger than 3). They were later supplemented by the NED query.

[2]Not a VCC object, its morphological type was assigned manually.

sorted through the results to obtain the valid object and its corresponding measurements. This was done by inspecting the radii and their errors and comparing it to the optical image to check whether such measurement is plausible. Despite this, for some objects, the SDSS simply could not provide good data. In those cases I downloaded the SDSS' `.fits` images in g and i bands and performed my own measurements manually in the `SAOImageDS9` program. The color of the galaxy $(g-i)$ was calculated by subtracting m_i from m_g.

Finally, I obtained the R_{P90} from the SDSS, but for calculation of HI deficiency it was more preferential to use the radius (or diameter) a, used in the GOLDMine catalog, computed from surface brightness of 25th magnitude / arcsec^2. Following the procedure of Deshev et al. (2022), I assumed a simple linear relation between them: $a = R_{P90} \times A + B$. For this calculation I used the objects from the optical catalog, which had both a and R_{P90}. However some of those objects were very bright early-type galaxies, for which the Petrosian radius is likely unsuitable, e.g. because of their steeper more cusp-like light profiles, resulting in outliers. Given their low number I decided to discard them from this conversion process. In total, I was able to obtain the radius measurements of 56 objects, see fig. 3.7.

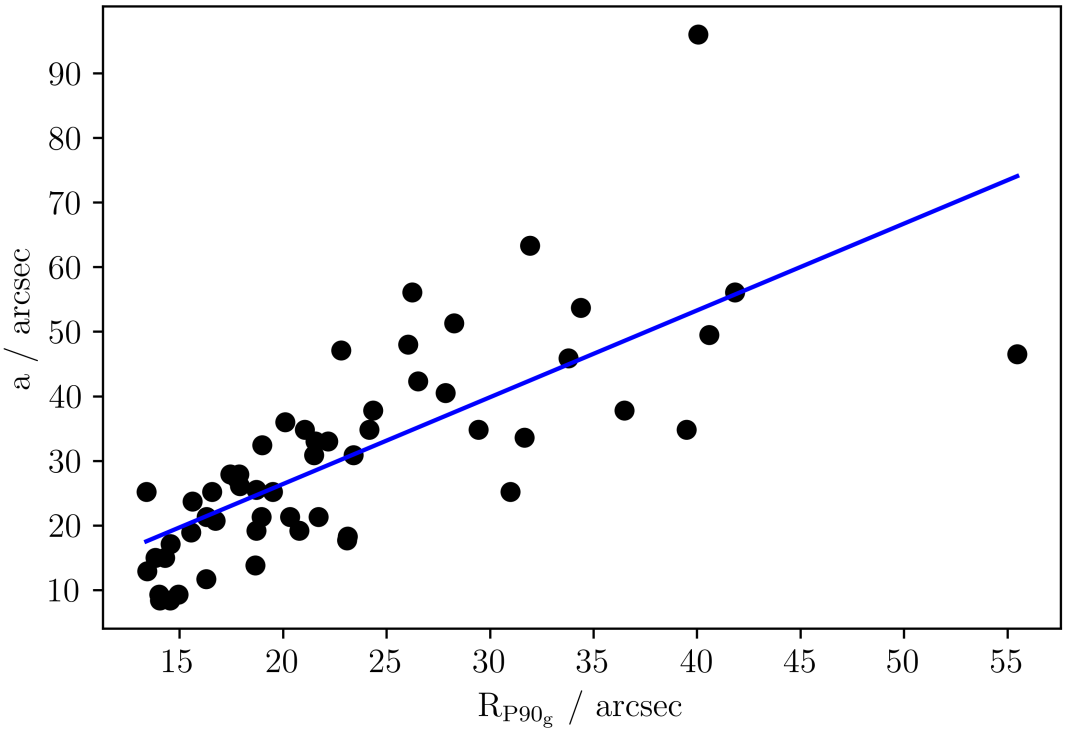

Figure 3.7: Relationship between the GOLDMine a and the SDSS R_{P90} radii. The blue line is the fitted linear regression.

The resulting conversion relationship is given by the equation

$$a = R_{P90} \times 1.344 - 0.481. \tag{3.1}$$

It should be noted however that this relation is only valid for values of $R_{P90} \gtrsim 10$ arcsec. Using the equation above I converted all the R_{P90} radii into an a-equivalent radius, which I named R_g and used in all the related analysis.

Finally, I wrote a simple Python script which queried the NED Extinction Calculator for each object with a photometry measurement. NED then returned the foreground Galactic extinction in the appropriate band using the Schlafly and Finkbeiner (2011) recalibration of the extinction map by Schlegel et al. (1998). The extinction values were then subtracted from both photometric magnitudes in all cases.

The VCS catalog with corrected photometry and converted R_g radius is shown in table 3.4.

Table 3.4: Optical VCS objects with photometry and radius measurements. Radius measurements were done using the m_g band. The $g-i$ column indicates the object's color, with lower values bluer and greater values redder. The errors in brackets are given by the SDSS. If there are no error brackets, the photometry or radius was obtained manually from the SDSS fits file of the corresponding band. The HI deficiency is discussed in subsection 3.5.8.

Name	m_g [mag]	m_i [mag]	$g-i$ [mag]	R_g [arcsec]	D_{HI}
VCS 1	12.745(0.002)	11.762(0.002)	0.984(0.003)	216.8(8.7)	0.69
VCS 3	15.905(0.005)	15.522(0.009)	0.383(0.010)	45.8(1.5)	0.17
VCS 4	17.054	16.426	0.628	40.9	0.82
VCS 5	14.707(0.002)	14.066(0.002)	0.641(0.003)	33.1(0.3)	0.06
VCS 6	17.470(0.023)	16.750(0.017)	0.720(0.029)	31.1	0.83
VCS 8	16.368(0.008)	15.849(0.010)	0.519(0.013)	60.4(3.2)	1.00
VCS 10	18.500(0.016)	18.704(0.046)	-0.203(0.049)	15.6(1.3)	0.42
VCS 11	17.395	16.943	0.451	39.4	–
VCS 12	17.558(0.016)	17.170(0.020)	0.388(0.025)	31.1(2.3)	0.81
VCS 13	16.405	16.254	0.151	26.3	1.24
VCS 14	18.060	17.234	0.827	23.984	1.00
VCS 15	18.066(0.023)	17.414(0.025)	0.652(0.034)	40.6(4.8)	1.37
VCS 16	16.215(0.004)	15.559(0.004)	0.656(0.006)	29.4(0.6)	0.32
VCS 17	15.190(0.005)	14.605(0.010)	0.585(0.011)	55.0(1.1)	0.50
VCS 22	15.465(0.004)	14.978(0.008)	0.487(0.009)	48.7(2.6)	0.80
VCS 23	18.155(0.010)	17.844(0.016)	0.311(0.019)	15.8(1.0)	0.57
VCS 24	16.076(0.004)	15.615(0.006)	0.461(0.007)	37.8(0.8)	1.15
VCS 25	14.943(0.004)	14.274(0.008)	0.669(0.009)	111.7(3.3)	-0.02
VCS 26	15.430(0.004)	14.922(0.005)	0.509(0.006)	83.1	0.47
VCS 27	13.494(0.002)	12.185(0.002)	1.309(0.003)	128.5(3.0)	0.19
VCS 28	13.221(0.002)	12.552(0.002)	0.669(0.003)	115.0(1.3)	0.26
VCS 29	13.227(0.002)	12.027(0.002)	1.200(0.002)	100.5(1.3)	0.27
VCS 30	16.503(0.006)	16.060(0.008)	0.443(0.010)	42.6(0.9)	-0.27
VCS 31	15.639(0.003)	14.994(0.004)	0.645(0.005)	26.8(0.2)	-0.14
VCS 32	17.734(0.010)	17.354(0.020)	0.381(0.022)	32.0(1.8)	0.30
VCS 33	17.370(0.021)	16.863(0.029)	0.506(0.036)	44.4	0.35
VCS 34	16.393	16.067	0.325	64.2	0.57
VCS 35	12.710(0.002)	11.757(0.002)	0.953(0.003)	177.3(3.8)	-0.02
VCS 37	13.139(0.002)	12.241(0.002)	0.897(0.003)	86.5(3.4)	0.49
VCS 38	12.376(0.002)	11.525(0.002)	0.851(0.003)	151.3(2.4)	0.88
VCS 39	12.917(0.002)	11.715(0.002)	1.202(0.002)	145.3(0.8)	0.80

Table 3.4 continued from previous page

Name	m_g [mag]	m_i [mag]	$g-i$ [mag]	R_g [arcsec]	$D_{\rm HI}$
VCS 40	16.856(0.010)	16.645(0.019)	0.210(0.022)	36.3(1.6)	0.25
VCS 41	16.767(0.006)	16.326(0.010)	0.441(0.011)	27.6(0.8)	0.11
VCS 42	14.878(0.003)	14.705(0.005)	0.173(0.006)	108.7(2.5)	0.60
VCS 43	17.385(0.005)	17.150(0.007)	0.235(0.009)	13.3(0.3)	-0.19
VCS 44	17.222	17.045	0.176	28.6	-0.01
VCS 45	17.484(0.007)	17.236(0.014)	0.248(0.016)	16.6(4.2)	0.00
VCS 46	18.762(0.030)	18.407(0.045)	0.355(0.054)	24.2(2.3)	0.45
VCS 47	14.760(0.003)	14.123(0.003)	0.637(0.004)	58.2(0.7)	–
VCS 48	12.972(0.002)	11.629(0.002)	1.343(0.003)	178.4(7.6)	1.12
VCS 49	16.268(0.007)	15.625(0.008)	0.644(0.011)	49.0(1.2)	1.62
VCS 50	13.644(0.002)	12.502(0.002)	1.142(0.003)	126.7(0.7)	1.38
VCS 51	17.551(0.020)	17.021(0.021)	0.530(0.029)	33.0(2.4)	–
VCS 52	15.537(0.006)	14.807(0.022)	0.730(0.023)	57.3(1.1)	1.26
VCS 53	16.840(0.014)	16.254(0.051)	0.586(0.053)	47.8(1.6)	1.16
VCS 55	17.500(0.011)	17.028(0.015)	0.473(0.018)	29.3(2.2)	0.64

The same exact procedure was repeated with the HI non-detected objects, which are shown in table 3.5.

Table 3.5: Non-HI detected objects with photometry and radius measurements. Radius measurements were done using the m_g band. The $g-i$ column indicates the object's color, with lower values bluer and greater values redder. The errors in brackets are given by the SDSS. If there are no error brackets, the photometry or radius was obtained manually from the SDSS fits file of the corresponding band.

Name	m_g [mag]	m_i [mag]	$g-i$ [mag]	R_g [arcsec]
VCC 1003	11.381(0.002)	10.059(0.001)	1.322(0.002)	185.1(2.8)
VCC 1039	17.141(0.012)	16.202(0.013)	0.938(0.017)	36.7(1.7)
VCC 1062	11.118(0.001)	9.906(0.001)	1.212(0.002)	108.8(4.7)
VCC 1075	14.723(0.003)	13.840(0.003)	0.883(0.004)	182.0(3.1)
VCC 1076	16.941(0.015)	16.085(0.015)	0.856(0.022)	36.2(2.1)
VCC 1078	15.752(0.004)	15.329(0.010)	0.424(0.011)	50.1(0.7)
VCC 1079	16.972(0.014)	16.121(0.014)	0.851(0.020)	61.1(4.2)
VCC 1164	16.690(0.011)	15.850(0.010)	0.839(0.015)	53.7(2.7)
VCC 1175	15.338(0.003)	14.764(0.004)	0.573(0.005)	45.9(0.8)
VCC 118	16.145(0.009)	15.399(0.015)	0.746(0.018)	47.2(1.0)
VCC 1209	17.293(0.013)	16.458(0.018)	0.835(0.022)	36.8(2.1)
VCC 1261	13.302(0.002)	12.386(0.002)	0.915(0.003)	111.5(1.9)
VCC 1273	15.063(0.004)	14.365(0.006)	0.698(0.007)	77.6(1.9)
VCC 1303	12.802(0.002)	11.647(0.002)	1.154(0.002)	83.9(1.2)
VCC 1377	16.440(0.010)	15.668(0.011)	0.772(0.015)	61.2(2.0)
VCC 1412	11.838(0.002)	10.643(0.001)	1.195(0.002)	127.1(2.4)
VCC 1422	13.434(0.002)	12.517(0.002)	0.917(0.003)	108.1(0.7)
VCC 1444	15.960(0.007)	15.094(0.010)	0.865(0.012)	64.0(2.8)
VCC 1446	15.983(0.005)	15.070(0.005)	0.913(0.007)	51.5(0.9)

Table 3.5 continued from previous page

Name	m_g [mag]	m_i [mag]	$g-i$ [mag]	R_g [arcsec]
VCC 1481	17.759(0.015)	16.969(0.016)	0.790(0.022)	39.2(3.5)
VCC 1488	14.837(0.003)	14.219(0.003)	0.619(0.004)	64.5(1.8)
VCC 1489	15.801(0.005)	14.948(0.005)	0.853(0.007)	50.0(1.4)
VCC 1496	17.895(0.019)	17.041(0.018)	0.854(0.026)	35.2(4.8)
VCC 1509	16.756(0.009)	15.908(0.009)	0.849(0.013)	40.9(2.7)
VCC 1521	13.690(0.002)	12.587(0.002)	1.104(0.003)	69.6(4.1)
VCC 1549	14.456(0.003)	13.406(0.002)	1.050(0.003)	25
VCC 1567	14.578(0.003)	13.579(0.007)	0.999(0.008)	148.2(4.1)
VCC 1629	17.265	16.433	0.832	40.942
VCC 1647	16.053(0.008)	15.103(0.008)	0.950(0.011)	49.3(1.3)
VCC 1661	16.141(0.006)	15.131(0.006)	1.010(0.008)	53.1(1.2)
VCC 1684	15.078(0.003)	14.421(0.004)	0.656(0.005)	84.2(4.6)
VCC 1704	16.299(0.010)	15.430(0.013)	0.869(0.016)	41.0(1.3)
VCC 1720	12.171(0.002)	10.994(0.002)	1.177(0.002)	104.0(0.4)
VCC 1743	15.495(0.004)	14.611(0.004)	0.884(0.006)	56.8(1.2)
VCC 1762	16.271(0.006)	15.464(0.007)	0.807(0.010)	46.8(1.3)
VCC 1767	16.642(0.008)	15.826(0.008)	0.816(0.011)	54.9(1.9)
VCC 1803	16.187(0.006)	15.284(0.006)	0.903(0.009)	49.2(1.5)
VCC 1813	11.499(0.002)	10.174(0.001)	1.324(0.002)	137.0(3.6)
VCC 1826	15.561(0.003)	14.639(0.003)	0.922(0.004)	47.1(0.7)
VCC 1857	14.995(0.004)	14.243(0.004)	0.751(0.006)	75.0(1.7)
VCC 1861	14.503(0.002)	13.483(0.002)	1.020(0.003)	97.1(0.9)
VCC 1869	11.883(0.002)	10.666(0.001)	1.217(0.002)	104.9(15.0)
VCC 1881	16.136(0.007)	15.249(0.009)	0.887(0.012)	49.3(1.2)
VCC 1891	16.956(0.008)	16.034(0.007)	0.921(0.011)	37.5(1.6)
VCC 1895	14.929(0.003)	14.012(0.004)	0.917(0.005)	69.0(0.7)
VCC 1896	14.927(0.003)	13.928(0.002)	1.000(0.004)	73.9(0.9)
VCC 1919	16.992(0.010)	16.181(0.010)	0.811(0.014)	48.3(2.6)
VCC 1936	15.700(0.004)	14.779(0.003)	0.921(0.005)	61.9(1.0)
VCC 1948	15.501(0.004)	14.652(0.005)	0.850(0.007)	57.0(0.9)
VCC 1958	16.707(0.007)	15.830(0.007)	0.876(0.010)	42.8(1.5)
VCC 1971	16.469(0.007)	15.573(0.008)	0.896(0.011)	42.8(1.4)
VCC 2000	11.626(0.001)	10.466(0.001)	1.160(0.002)	67.2(4.0)
VCC 2042	15.189(0.004)	14.424(0.004)	0.765(0.006)	70.3(4.3)
VCC 2048	13.562(0.002)	12.581(0.002)	0.981(0.003)	84.9(9.4)
VCC 2066	11.961(0.002)	11.376(0.002)	0.585(0.002)	106.7(4.7)
VCC 216	14.992(0.003)	14.081(0.003)	0.911(0.004)	60.3(1.0)
VCC 227	15.293(0.004)	14.485(0.003)	0.809(0.005)	55.6(1.5)
VCC 275	14.772(0.006)	14.145(0.010)	0.627(0.012)	91.5(3.2)
VCC 394	17.378(0.013)	16.672(0.014)	0.706(0.019)	36.7(3.1)
VCC 407	14.537(0.004)	13.642(0.006)	0.895(0.007)	78.2(1.0)
VCC 458	16.846(0.020)	15.985(0.023)	0.861(0.031)	43.6(2.0)
VCC 504	16.897(0.009)	16.208(0.012)	0.690(0.015)	44.0(2.4)
VCC 529	17.595(0.022)	16.774(0.021)	0.821(0.031)	38.1(4.7)
VCC 546	15.733(0.005)	14.974(0.006)	0.759(0.008)	56.4(0.8)

Table 3.5 continued from previous page

Name	m_g [mag]	m_i [mag]	$g-i$ [mag]	R_g [arcsec]
VCC 695	15.974(0.006)	15.151(0.006)	0.823(0.008)	82.3(3.1)
VCC 698	12.968(0.002)	11.882(0.002)	1.086(0.002)	121.8(4.5)
VCC 747	17.408(0.018)	16.547(0.016)	0.861(0.024)	38.2(2.3)
VCC 756	17.091(0.013)	16.416(0.015)	0.674(0.020)	35.0(1.3)
VCC 856	14.288(0.002)	13.348(0.002)	0.940(0.003)	89.8(0.8)
VCC 920	17.441(0.013)	16.808(0.015)	0.632(0.019)	44.0(11.2)
VCC 931	16.367(0.007)	15.535(0.007)	0.831(0.010)	57.4(1.6)
VCC 944	11.745(0.002)	10.580(0.001)	1.165(0.002)	88.0(4.2)
VCC 949	15.493(0.005)	14.500(0.004)	0.993(0.006)	105.2(5.1)
VCCA 038	17.330(0.008)	16.549(0.008)	0.782(0.011)	27.9(1.1)
WISEA J121341.44+090040.4	17.539(0.012)	16.696(0.013)	0.843(0.018)	30.9(1.8)
WISEA J121443.02+103159.2	18.072(0.010)	17.587(0.013)	0.485(0.016)	18.8(1.0)
WISEA J121453.51+094011.5	17.245(0.007)	16.890(0.010)	0.355(0.012)	21.3(0.8)
WISEA J122020.13+094750.1	17.781(0.011)	17.322(0.014)	0.459(0.018)	23.4(1.7)
WISEA J123955.45+095520.4	17.724(0.007)	17.331(0.008)	0.393(0.010)	11.2(0.4)
WISEA J124533.24+102925.8	18.291(0.019)	17.438(0.031)	0.852(0.036)	21.7(1.4)
IC 3711	15.716(0.005)	14.705(0.004)	1.011(0.007)	51.7(1.0)
VCC 2012	14.653(0.003)	14.048(0.004)	0.606(0.006)	55
IC 3767	15.771(0.007)	14.866(0.007)	0.905(0.010)	58.2(2.3)
SDSS J124101.06+094306.3	17.749(0.008)	17.321(0.011)	0.428(0.013)	19.3(1.0)
VCC 1357	18.926	18.321	0.605	31.871
VCC 1804	15.812(0.005)	15.152(0.005)	0.660(0.007)	46.1(2.2)

3.4 New non-VCC objects

I detected 14 VCS objects (see table 3.2) and 10 non-HI galaxies (see table 3.3) in the WAVES region, which have not been detected by the VCC. This is interesting, because VCC is a volume-limited survey of the Virgo Cluster, which means it is supposed to be complete to a photographic magnitude 18, which is roughly equivalent to SDSS' g-band (Taylor et al., 2012). Moreover, in case of the VCS objects, we are not optically-biased, because we primarily look for HI and only then the optical counterpart. That means the HI gas may more easily indicate a presence of a faint galaxy, which would otherwise be missed in the visual band.

Out of the 14 mentioned VCS objects 8 were galaxies, with 7 at 17 Mpc, only one at 32 Mpc and all of them either spiral or irregular. They are all also blue and rather faint ($m_g \gtrsim 15.5\ mag$), which could explain their absence from the VCC. Their HI masses are typically $\sim 10^7$ $M_\odot$, but one of them, VCS 44, is also the

most gas-rich VCS objects with $M_{HI} \approx 8.0 \times 10^8$ $M_\odot$ (for more see subsections 3.6.4 and 4.3.3).

Generally, the non-VCC objects were also fainter ($m_g \gtrsim 16.5\ mag$) than the majority of the sample, with 7 of them at 17 Mpc, 2 at 23 Mpc and 1 at 32 Mpc. They were all marked as either elliptical or irregular, according to my own classification, but their low surface brightness may have affected this.

Taylor et al. (2012) detected 95 HI sources in the VC1 region, out of which 26 had non-VCC counterparts and 14 of them were actually brighter than the VCC completeness limit. That translated into $\sim 5\%$ of the total 285 galaxies in VC1. For comparison, out of the 18 non-VCC objects I detected, 13 were brighter than the $g = 18$ limit, which corresponds to roughly 4% of the total number of 296 VCC objects in the WAVES region. This fraction is practically the same as in VCC and reasonable given the VCC's limitations.

Lastly, in addition to the above objects I detected 6, which had no optical counterpart whatsoever and I was only able to detect them in the HI emission. These are either completely dark clouds (VCS 54) or star-forming gas clouds (VCS 18–21 and VCS 9). I will further discuss these objects in sections 3.6 and 4.3.

3.5 Statistical analysis

To infer how galaxy evolution proceeds we have to look at different galaxies which are at different points in their evolution and compare them statistically. I do this here by comparing the WAVES region with the VC1 region studied by AGES by Taylor et al. (2012). I will start with the broad statistical properties of the sample before moving on to specific trends in the data.

3.5.1 Data verification

The HI mass and velocity width histogram of the 46 VCS objects with optical counterparts, see table 3.2, compared to the 81 VC1 HI-detected galaxies with reliable optical measurements is shown in figure 3.8.

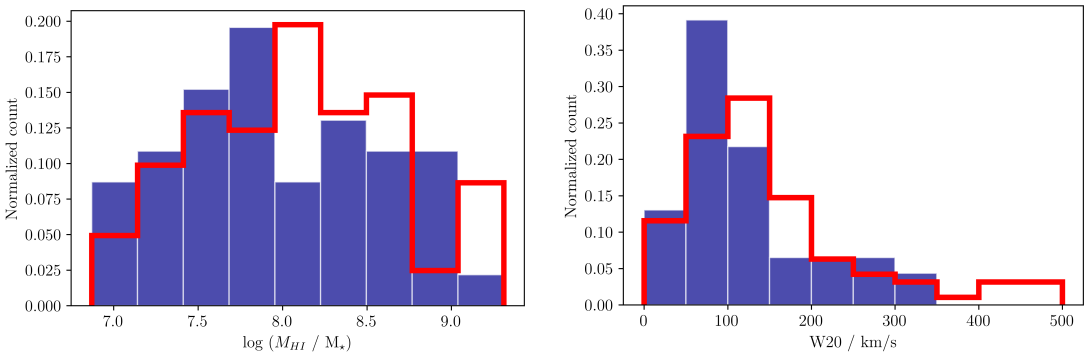

Figure 3.8: (a) HI mass histogram (in logarithmic units) and (b) HI W20 histogram for 46 optical VCS objects (blue bars) and 81 HI-detected VC1 objects (red outline).

We can see the distributions of WAVES and VC1 objects are in general agreement and are not fundamentally different, which is consistent with results from the Kolmogorov-Smirnov (KS) and Mann-Whitney (MW) tests.

Both of these distributions serve as good sanity checks to confirm the validity of my data. To further verify the accuracy of my results, specifically the HI line measurements, I compared the HI masses of the WAVES VCS objects to one's recorded by the ALFALFA survey by Giovanelli et al. (2005). For that I obtained the complete HI catalog from the ALFALFA website, cross-matched it with the VCS catalog using the 1.75 arcmin sky separation and velocity difference < 200 kms^{-1} to obtain 42 objects which were present in both catalogs. Then, after discarding an outlying VCS 35, because it was not fully in the WAVES data cube, as seen in figure A.4, I plotted the calculated masses of the resulting 41 objects from both catalogs, shown in figure 3.9.

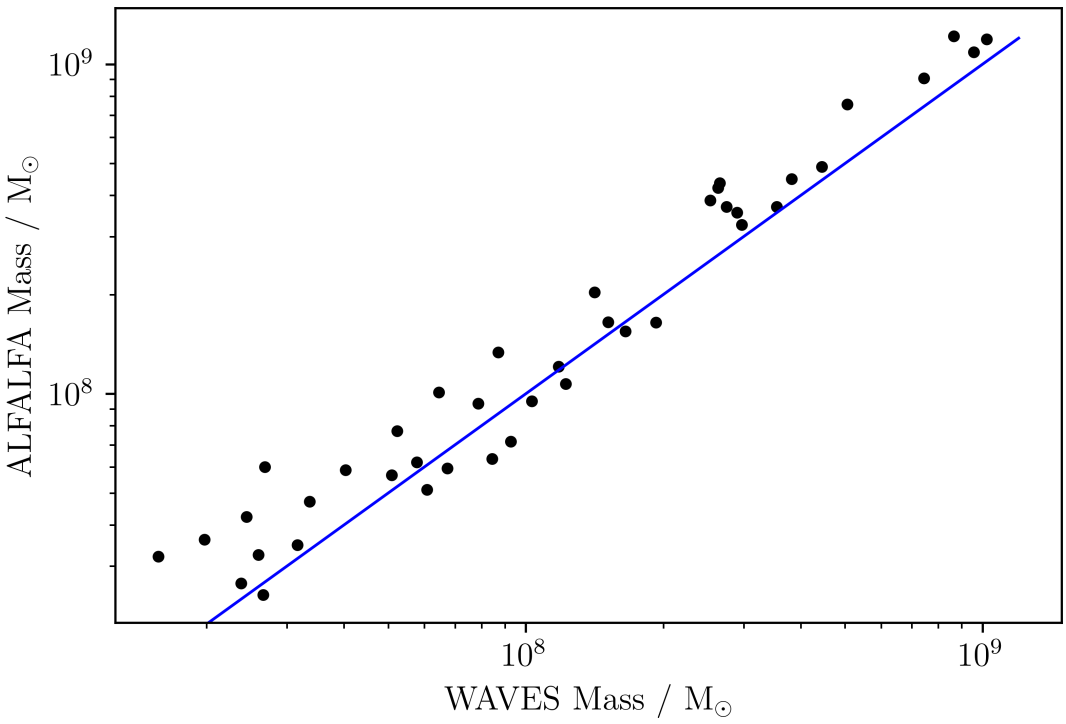

Figure 3.9: Mass comparison of the WAVES objects and the corresponding ALFALFA objects. The line shows a linear regression fit.

The points follow a tight linear trend, with correlation of 0.987. And while WAVES detected 13 extra objects, the mass estimates are in good agreement with ALFALFA. This demonstrates that WAVES is indeed benefitting from its extra sensitivity and that it has been calibrated accurately.

3.5.2 Spatial distribution

The spatial distribution of the VCS objects with an HI detections and objects without an HI detection, using coordinates from tables 3.1 and 3.3 is shown in figure 3.10. We can see that while overall the objects are distributed quite evenly, the HI detected objects are somewhat clumped in two regions. One of the clumps is located near the center of the data and the second one is directly west between $182 < RA < 185$.

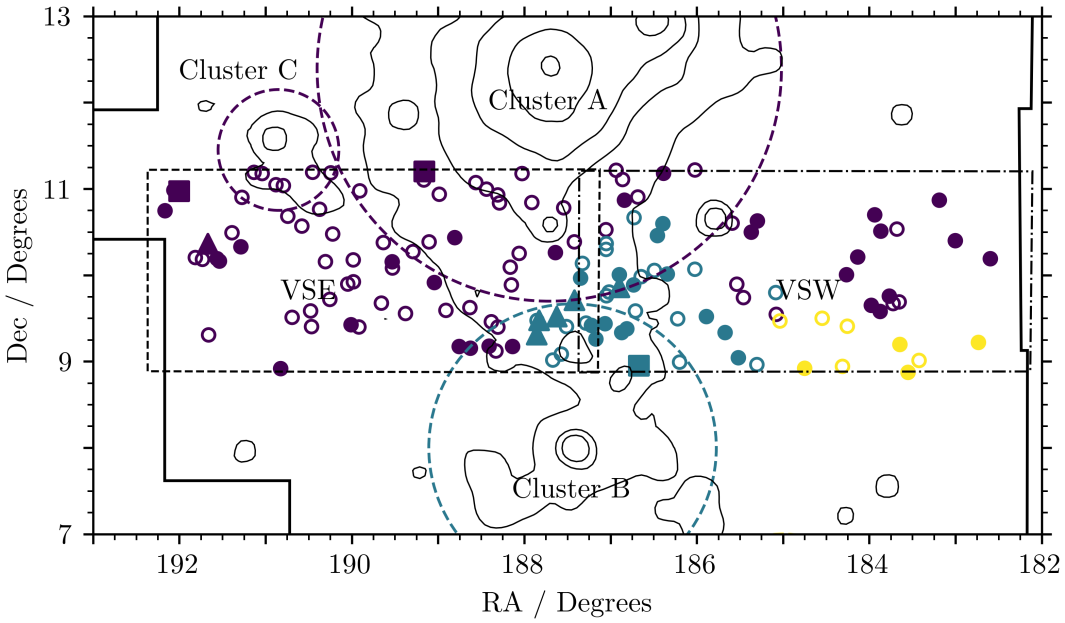

Figure 3.10: Spatial plot of the HI detected and undetected objects. The circles show HI detected galaxies, open circles show HI non-detected galaxies, squares show pairs of galaxies with unresolvable HI envelope and triangles show gas clouds. The colors indicate distance: purple = 17 Mpc, blue = 23 Mpc and yellow = 32 Mpc.

I further selected all the Virgo Cluster members from the GOLDMine catalog in WAVES and VC1, without any further filtering by velocity or photometry, and got 296 and 282 galaxies respectively. This was done only here to compare the crude statistics of the total number of objects in the two regions and any further filtering could have biased either region, for example because the VC1 region is more complete in terms of velocity measurements. In the rest of my analysis I utilized the more strict filtering, because velocities were needed to confirm the membership of each galaxy, but here it is sufficient to use the approximate distances given by Binggeli et al. (1985). Of course, there are more actual galaxies than the VCC objects, but given their low number in catalog of HI non-detected objects in WAVES (13 out of total 86), their contribution should not significantly impact this. Especially, if a similar fraction of non-VCC objects is found in VC1. For more see section 4.1.1.

3.5.3 RA and declination distributions

Here, I show the RA and declination distributions of the 46 VCS objects with single optical counterparts, which allow us to study the distribution of objects along each axis. The RA and declination histograms of the HI and non-HI detections are shown in figure 3.11.

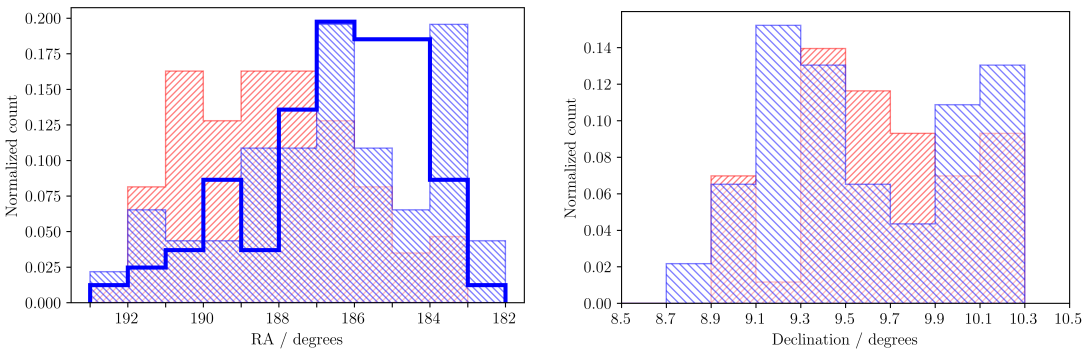

(a) (b)

Figure 3.11: The blue bars represent the HI-detected objects, red bars the HI non-detected objects. Both histograms are in normalized counts. (a) RA histogram, bin size is 1 degree. The horizontal axis is inverted to be consistent with figure 3.10. The blue outline shows the VC1 HI-detected objects. (b) Declination histogram, bin size is 0.2 degree.

Again, as in the case of the spatial distribution plot, we can see from the RA histogram, the HI detections are more clumped, while the objects without an HI follow a rather more continuous, perhaps even normal-like, distribution. I support this with KS and MW statistical tests, which claim the two populations of HI and non-HI detected objects are indeed different to a 99.99% significance level.

The declination histogram however is slightly more ambiguous. We can see the HI-detection population is more continuous, while the non-HI objects have a noticeable dip around $\delta \approx 9.2$ degrees. The ambiguity is also fueled by the fact that the MW test claims the difference to a 96% confidence level, while the KS test is inconclusive with a p-value of 0.1.

The RA histogram also compares the HI source distribution in the WAVES and AGES VC1 regions. The distributions, despite the drop in WAVES' objects around $RA \approx 185$ deg, follow roughly the same shape, which is consistent with the MW and KS tests (p-values are 0.74 and 0.55 respectively).

However, the WAVES and AGES areas sample galaxies in different substructures, i.e. at different distances. To correct for this I also show the RA histogram exclusively at these distances in figure 3.12.

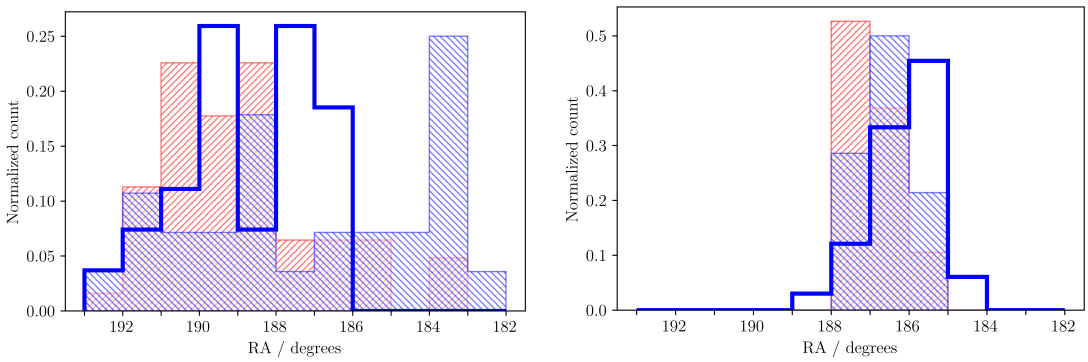

(a) (b)

Figure 3.12: RA histograms of only: 17 Mpc (a) and 23 Mpc (b) objects. Blue bars indicate HI detected objects, red bars the HI non-detected objects. The blue outline shows the VC1 HI detected objects. Bin size is 1 degree.

In case of the 17 Mpc plot the HI detected objects in WAVES shows objects missing from the region $188 > RA > 184$, which are those objects found at 23 Mpc. The latter plot also shows that at 23 Mpc the objects from WAVES and VC1 occupy similar RA, but according to the MW and KS tests they are still different to a 98% confidence level.

3.5.4 Morphological distribution

The morphological distribution of the all the detected galaxies, with or without HI content, is shown in figure 3.13. These distributions are typically consistent with HI being present mainly in late-type galaxies, and galaxies with no HI detections are usually early-type. However, there are some outliers in the form of ETG with HI and LTG without HI, which might indicate either incorrect morphological assignement or peculiarity of those objects, but I will discuss this later in more depth.

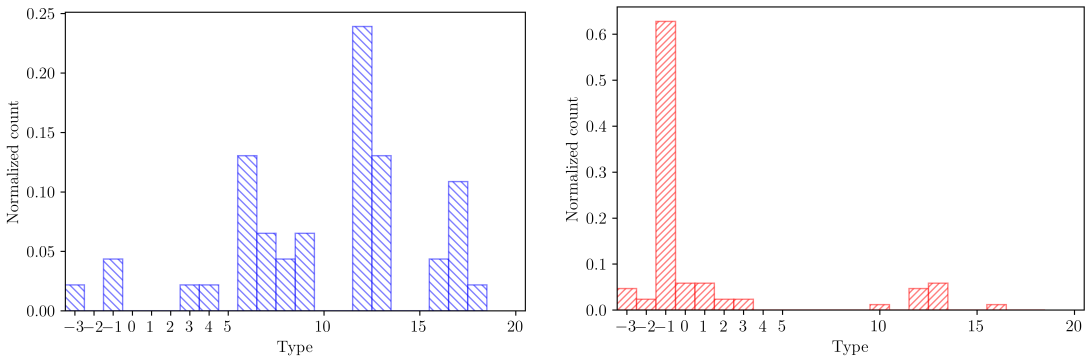

Figure 3.13: Morphological distribution of galaxies with HI content (left) and without HI content (right).

3.5.5 Velocity distribution

Studying the velocity histograms of the cataloged populations can tell us about the structure of the cluster, i.e. how the cluster is currently assembling. For

example, if we see more high-velocity objects, that could mean they belong to a cloud infalling on the main body, implying the region is still forming. The velocity histogram of 46 HI and 86 non-HI detected galaxies from WAVES and 81 HI detected galaxies from VC1 at all distances is shown in figure 3.14.

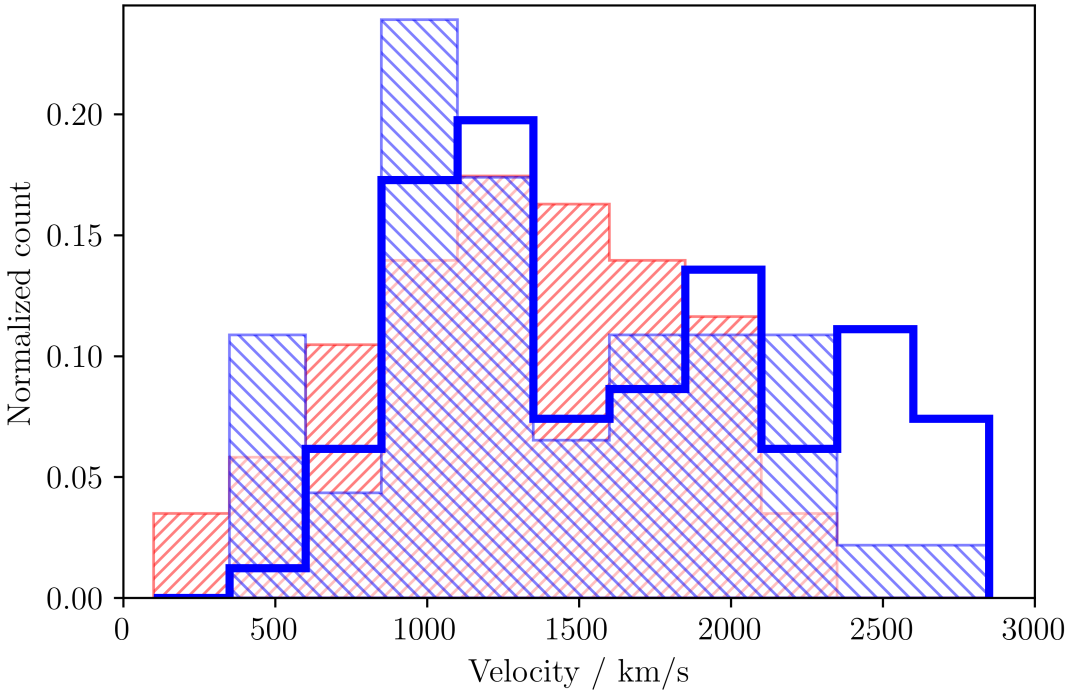

Figure 3.14: Velocity histogram of the 46 WAVES HI (blue bars) and 86 non-HI (red bars) galaxies with 81 HI detected galaxies from the VC1 region (blue outline) at 17, 23 and 32 Mpc distances. Bin size is equal to 250 kms^{-1}.

We can see from figure 3.14 that the two WAVES populations are similar and, according to the statistical tests, with p-value equal of 0.48 according to MW and 0.16 from the KS test, could be from the same distributions. In contrast, the VC1 objects, while still occupying similar velocity range, have an additional contribution in the form of a high-velocity tail ($v \gtrsim 2300$ kms^{-1}). This suggests that the HI populations of WAVES and VC1 are likely not exactly the same, which is further supported to a 96% confidence level by the MW test, although the KS test is inconclusive.

This result is not unexpected, since the VC1 region contains primarily objects which belong to the infalling clouds at greater distances, and therefore with greater velocity. If we limit the histogram to only show objects at 17 Mpc (the main body of the cluster), the distributions are rather more similar, as is shown in figure 3.15. In this case both the KS and MW tests cannot refute the null hypothesis of the populations being drawn from the same distribution.

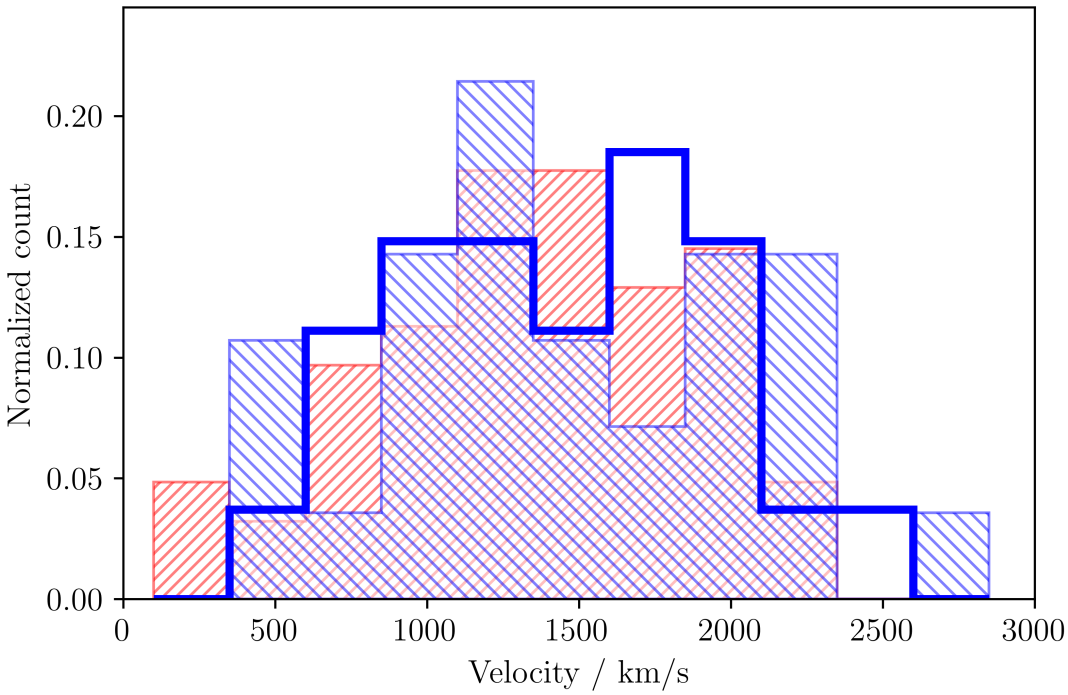

Figure 3.15: Velocity histogram with 28 HI detected objects (blue bars), 62 non-HI detected objects (red bars) and 27 VC1 HI detected objects (blue outline) at 17 Mpc. Bin size is equal to 250 kms^{-1}.

3.5.6 Color-magnitude diagram

The color-magnitude diagram (CMD) can help us understand galaxies based on their color, brightness and morphology, much like the stellar Hertzsprung-Russel diagram. The CMD is constructed by doing a scatter plot of early-type (red) and late-type (blue) galaxies with an absolute magnitude in g-band on the horizontal axis and $g - i$ magnitude (color) on the vertical axis. A lower value of $g - i$ indicates the object is more blue and higher value indicates more red. They show that while the early-type galaxies generally form a rather narrow red sequence, the late-type galaxies are usually more scattered and bluer. This is because ETGs are normally more evolved and without significant HI content, which would fuel star formation, leaving them "red and dead". In contrast LTGs can be still evolving and often have prominent star-forming regions, which gives them more variation in terms of color and magnitude.

I have used tables 3.2 and 3.3 for morphology and tables 3.4 and 3.5 for the magnitude measurements. I calculated the absolute magnitude of the galaxies by using the distance modulus equation

$$M \ = m - 5 \log \frac{d}{\mathrm{Mpc}} - 25, \tag{3.2}$$

where the distance d the distance is taken from tables 3.1 and 3.3. The resulting CMD of galaxies in the WAVES region is shown in figure 3.16.

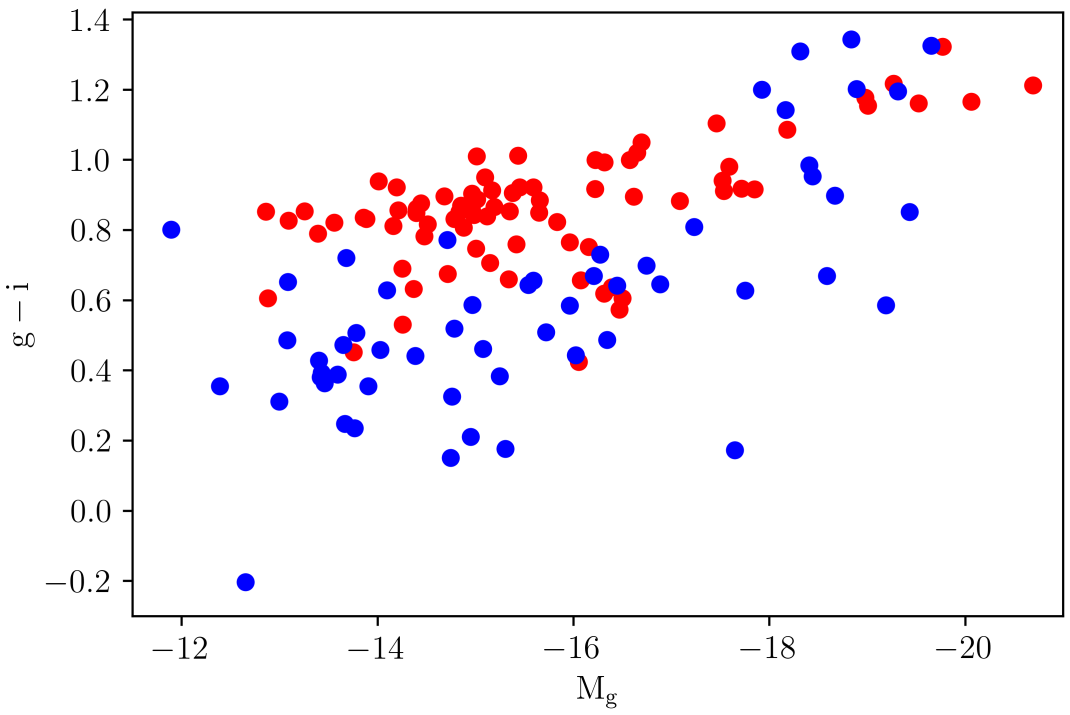

Figure 3.16: Color-magnitude diagram of HI detected and non-HI detected objects in the WAVES region. Blue points indicate late-type galaxies and red early-type galaxies.

The individual populations of early-type and late-type galaxies are shown in figure 3.17.

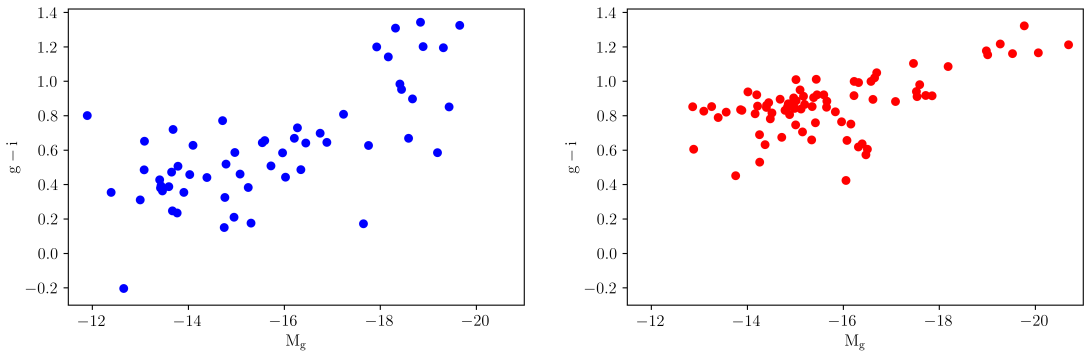

(a) (b)

Figure 3.17: Color-magnitude diagrams of only late-type galaxies (left) and early-type galaxies (right).

The outliers, like the surprisingly blue LTG with $g - i \approx -0.2$ or some early-type galaxies forming vertical "tails" coming down from the red sequence, were all checked to make sure the photometric data is correct.

3.5.7 Mass-to-light ratio diagram

While color relates to star formation, this only relates to gas content indirectly. We can study this more directly using the mass-to-light ratio diagram. This is a scatter plot with the logarithmic horizontal axis as the stellar mass of the galaxy and the logarithmic vertical axis as a fraction of HI mass and stellar mass. Here I used the values of HI mass and the i-band in tables 3.1 and 3.4. I converted the apparent magnitude into absolute using the distance modulus equation 3.2, and then used those values to calculate the total i-band luminosity by using the Pogson equation

$$L = 10^{\frac{M - M_\odot}{-2.5}} \times L_\odot, \tag{3.3}$$

where M and $M_\odot$ are the absolute magnitudes of the given galaxy and the Sun, respectively and $L_\odot$ is the solar luminosity. For this calculation I used the value $M_{i\odot} = 4.58$ given by Willmer (2018). We can further convert the luminosity into stellar mass estimate (in solar units) using the equation given by Taylor et al. (2011)

$$M_\star = 10^{-0.68 + 0.7 \times (g-i)} \times L_i, \tag{3.4}$$

where L_i is the total luminosity in the i-band. The resulting mass-to-light ratio diagram is shown in figure 3.18.

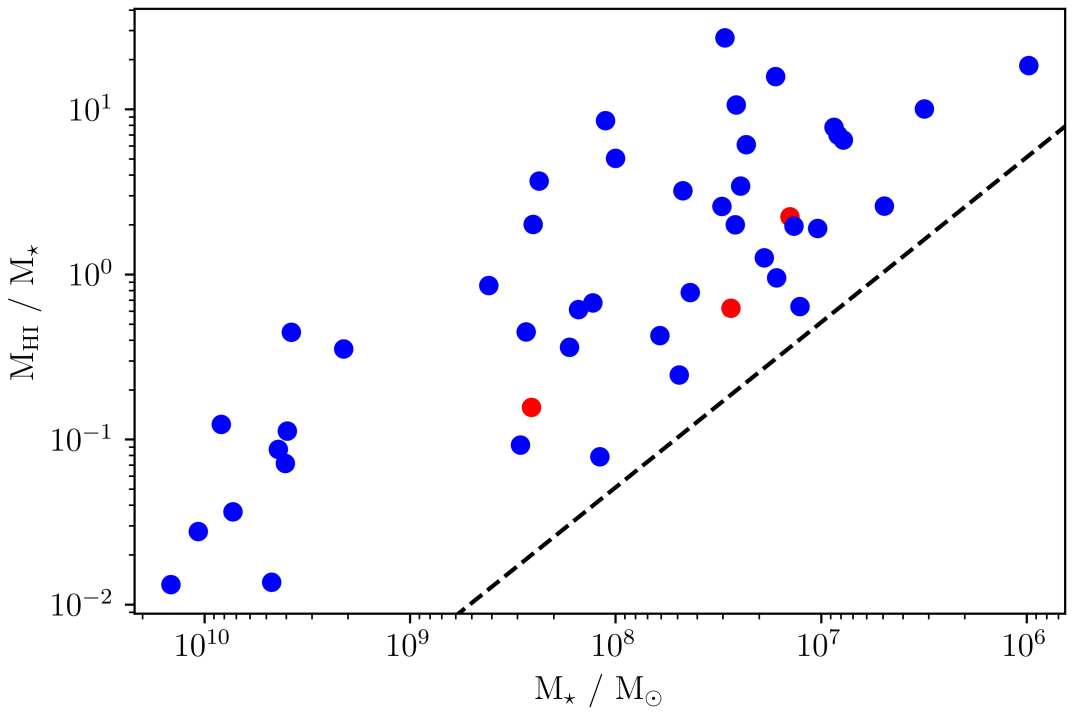

Figure 3.18: Mass-to-light ratio diagram with stellar mass. Blue points indicate late-type galaxies and red points the early-type galaxies. Both axis are logarithmic. The dashed line indicates the lowest sensitivity limit of the WAVES survey at 17 Mpc, 50 kms^{-1} width and 1 mJy *rms*.

We can see the overall trend is rising, but is partially a selection effect, since the fainter and less massive galaxies need more HI gas to be detected.

3.5.8 HI Deficiency

Besides the gas fraction, we can also study how much gas a given galaxy is thought to have lost. This is given by HI deficiency, which offers another look at how the environment may be affecting the galaxies. HI deficiency of the VCS objects was calculated using the equation 1.1 and the HI mass and radius R_g values from tables 3.1 and 3.4. The expected HI mass was calculated using the equation 1.2, with general-morphology parameters $a = 7.51$ and $b = 1.460$ given by Solanes et al. (1995). However it is important to mention that the parameters can be rather arbitrary and other authors, such as Gavazzi et al. (2005) and Haynes and Giovanelli (1984), suggested different values. While there is likely not one "correct" set of parameters, the ones used in this work are consistent with Boselli and Gavazzi (2009) and Taylor et al. (2013). The early-type galaxies were discarded from this analysis as very few of them have HI detections and they do not have reliable, well-established parameters for predicting their typical HI masses. The calculated HI deficiency was shown in table 3.4. Lastly, I included the 74 HI detected late-type galaxies in VC1 with good photometry (excluding 7 early-type galaxies) and plotted their HI deficiency distributions in figure 3.19

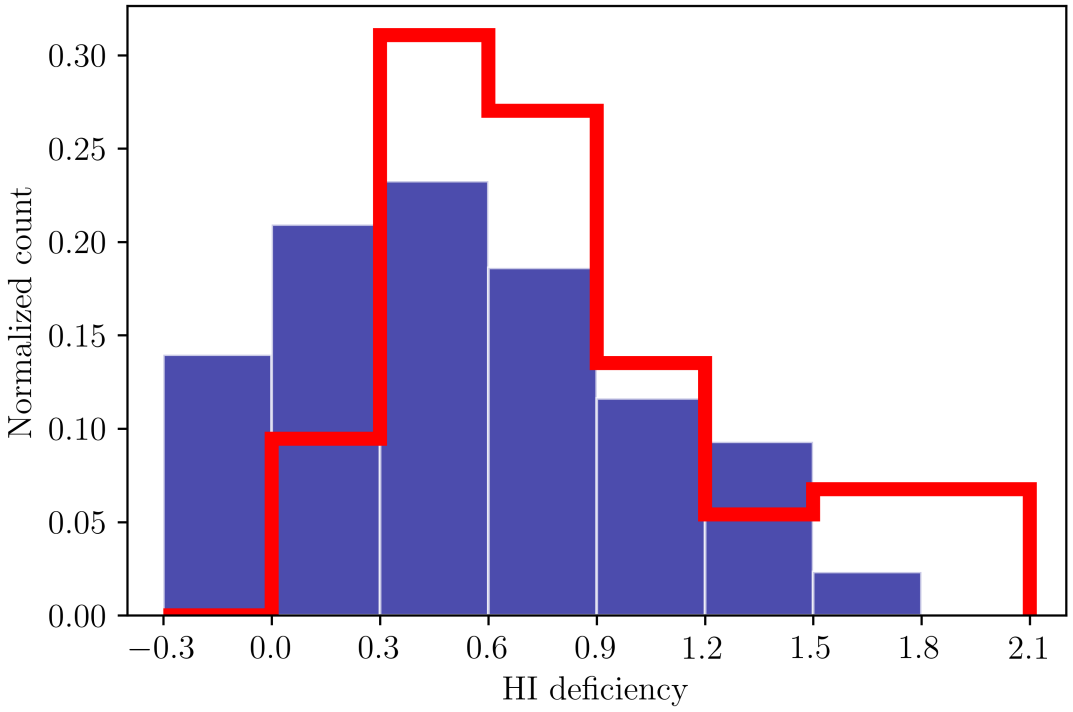

Figure 3.19: Normalized HI deficiency histogram. Blue bars show HI deficiency of 43 late-type VCS objects from table 3.4 and red outline shows the VC1 objects (74 in total).

The two distributions are rather different, with VC1 containing more HI deficient objects (27.0% objects with $D_{\mathrm{HI}} > 1$) than the WAVES region (only 23.3% objects with $D_{\mathrm{HI}} > 1$). This is further confirmed by the MW and KS statistical tests up to a 98.3% confidence level.

In order to get a better understanding of how the HI deficiency changes with the position within the cluster we can make a spatial scatter plot with HI defi-

ciency as auxiliary axis. This is shown in figure 3.20.

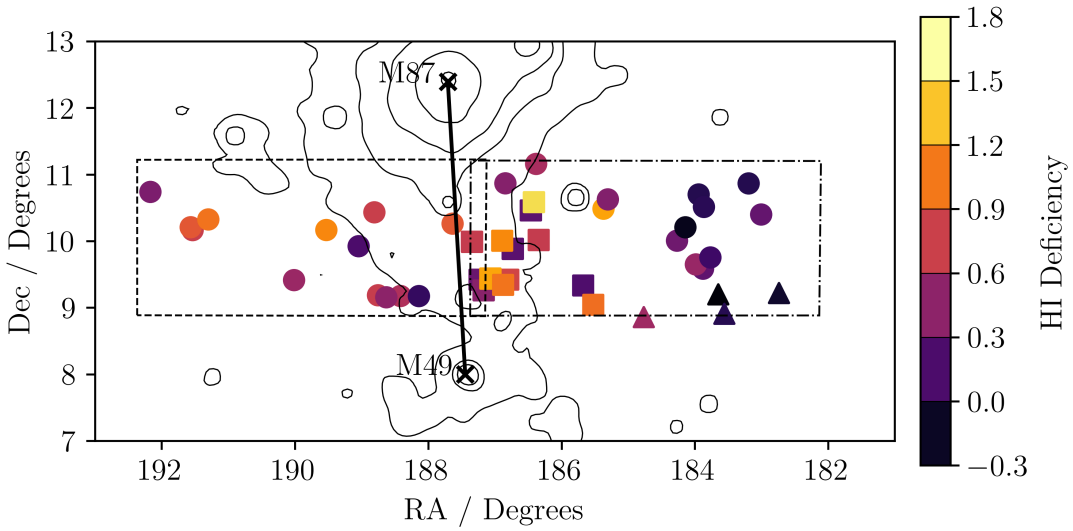

Figure 3.20: Spatial scatter plot of VCS objects with HI deficiency shown in color. The galaxies M87, M49 and the line, which represents the filament spine connecting them are shown. Symbols indicate the distance: circles = 17 Mpc, squares = 23 Mpc and triangles = 32 Mpc.

We can see the majority of the highly HI deficient objects are located closer to the denser parts of the cluster, with the less deficient galaxies on the outskirts. To show this more clearly we can also plot the HI deficiency as a function of distance either from: the center of the cluster A M87, center of the cluster B M49 or the filament spine connecting them, as shown in figure 3.20. These scatter plots, as well as their comparisons with the VC1 objects, are shown in figure 3.21. I also split every plot into 2 or 3 equally wide distance bins and calculated the median deficiency in each of them to better show the descending trend.

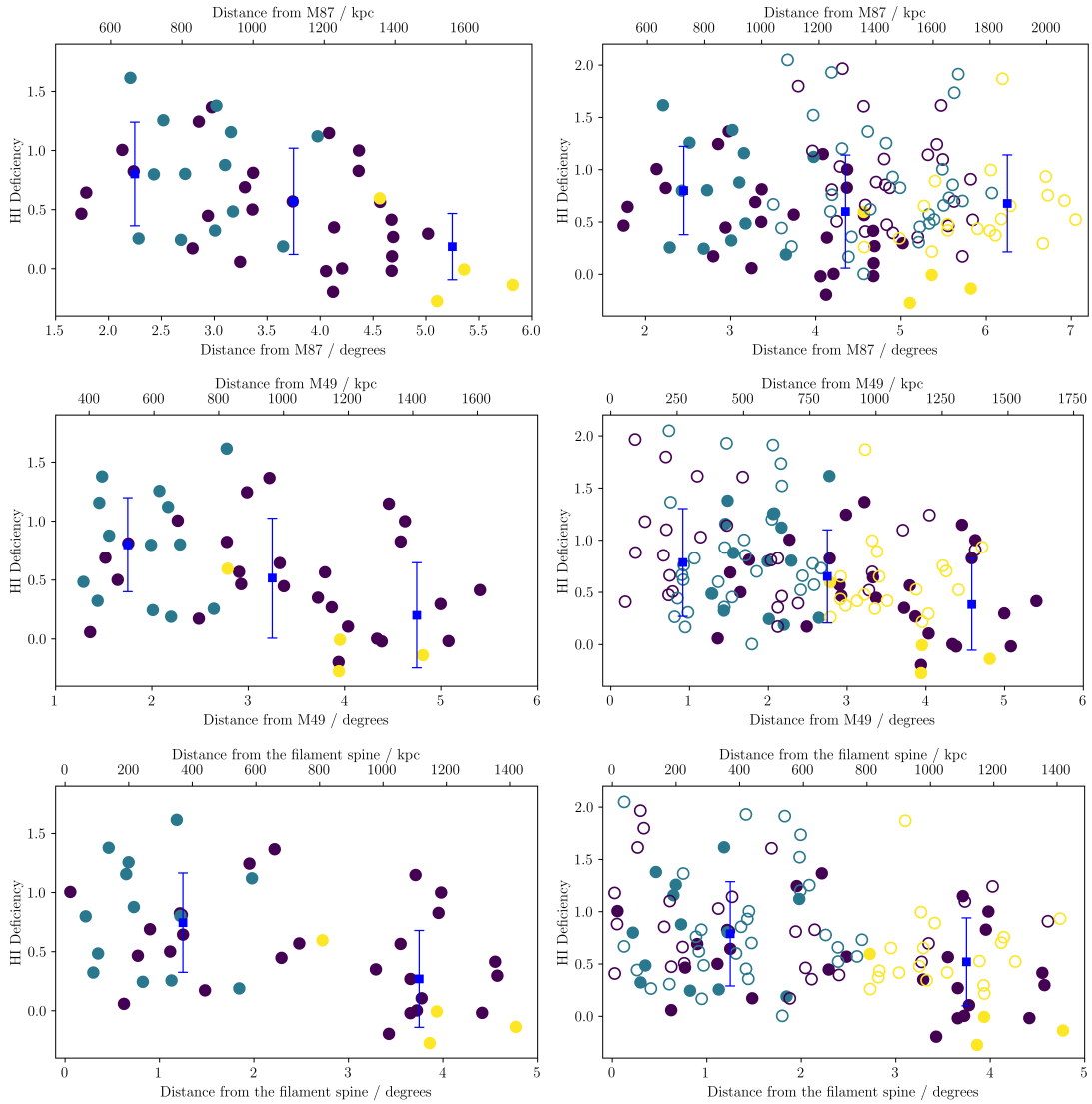

Figure 3.21: HI deficiency as a function of projected distance from M87, M49 and the filament spine. The projected distance is shown in degrees and kpc at the distance of 17 Mpc. The blue squares indicate a median deficiency in each bin with the error bars given by the standard deviation of that population. Colors of points indicate distance from us: purple = 17 Mpc, blue = 23 Mpc and yellow = 32 Mpc. **Left**: WAVES objects (filled circles). **Right**: WAVES (filled circles) and VC1 (open circles) objects. Note the different horizontal axis ranges.

For every first and last bin population I conducted a statistical t-test to confirm the descending trend. On WAVES (left) this was confirmed up to a 99.9% confidence level (except the M49 plot, which had only 93.7%). And on the WAVES and VC1 plots, the confidence levels were both 99.8% for the M49 and spine plots. The M87 plot was inconclusive probably because of too large distance of the VC1 region to M87.

3.5.9 Stacking

Basics of stacking

I detected 55 objects with an HI content in the WAVES region, including 3 early-type galaxies (VCS 11, VCS 47 and VCS 51). This is interesting, because as mentioned in section 1.1, the ETGs usually do not have much or any HI gas. So the question one should ask is whether these three galaxies are somehow special, or do all early-type galaxies have some HI but simply not enough to be detected with our sensitivity limit? The mass sensitivity is set by the distance of HI and the technical properties of the WAVES survey, but can be improved using "stacking". This is a well-tested method which has been done several times before with the ALFALFA and AGES surveys (Fabello et al., 2011; Taylor et al., 2012). It does not guarantee any new detection, but it does not require any new data and is potentially useful for placing a stronger constraint on the HI mass of the non-detected galaxies.

Stacking is done by combining the spectra of HI undetected galaxies. For that we need to know their redshifts from other measurements (usually optical) and center the spectra on the potential signal. The spectra are then added together and averaged (or "stacked"). Of course the spectra have to have the same velocity range so they span the same number of channels, and must also have the same channel width. In an ideal case, this will result in amplification of the systemic signal and decrease of random noise, hence lowering the rms. This way we lose information about the individual galaxies but we can learn whether the bulk of the population has some detectable HI content with our new better sensitivity.

Ideal example

To illustrate this I created a synthetic spectrum with random noise from a uniform distribution and injected a 1.5 σ signal in the middle five channels, as shown on figure 3.22 (a). From such spectrum one cannot for sure tell whether it is a real source or not. But if we stack 60 spectra like this, as shown in figure 3.22 (b), we can clearly see a detection.

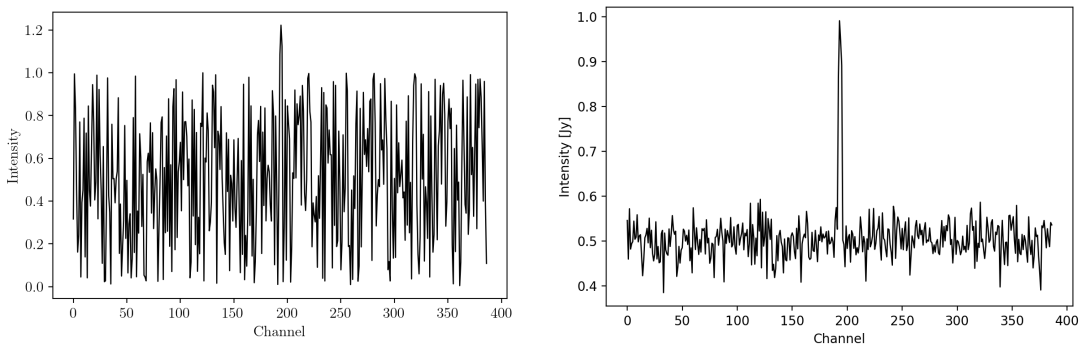

(a) (b)

Figure 3.22: Stacking example. (a) A synthetic spectrum of random uniform noise with a 1.5 σ injected signal in the 5 middle channels. (b) Result of stacking 60 spectra with a 1.5 σ injected signal.

Different approaches to stacking and weighting

In practice the measured spectra are not as perfect as in the idealized case described above. They can often be subjected to high rms, artifacts, baseline ripple or additional sources detected, which can affect the stacking process. To deal with this I employed several different approaches for the actual stacking. The first was to perform 3 σ clipping of all the stacked spectra, which helped lower the rms in case of spectra with baseline ripple or additional sources. For the stacking itself, I started with the easiest method, which is to simply add the spectra and divide the stack by the number of spectra, as shown in equation

$$S_{stacked} = \frac{1}{N} \sum_{i=1}^{N} S_i, \tag{3.5}$$

where S_i is each individual spectrum and N is the total number of them. I refer to this as "unweighted" stacking. The resulting noise can be estimated using the following equation

$$rms = \frac{rms_1}{\sqrt{N}}, \tag{3.6}$$

where rms_1 is the rms of a single spectrum. In practice this can be the mean (or median) rms of all the spectra, provided a they are not too different. We can also use the minimum or maximum rms levels for rms_1 here, which will predict the theoretical best and worst sensitivity levels we can achieve: i.e. the best possible sensitivity would be reached if all spectra had the lowest rms level, while the worst would occur if all had the highest rms level.

This method is simple and fast, but if there is a spectrum with an unusually high rms, then its contribution to the stack unfairly outweighs the other spectra. The solution to this is to introduce weights w_i, which lower the contribution of the spectra with higher rms and instead of dividing by the number of spectra, we divide by the sum of the weights. This is shown in equation

$$S_{stacked} = \frac{1}{\sum_{i=1}^{N} w_i} \sum_{i=1}^{N} S_i w_i. \tag{3.7}$$

I tried using two different weighting systems. The first was the "variance-defined" (VD) weights, which is done by recording rms of all the spectra in an array, raising all the values to some general power of k and then inverting them, as shown in equation

$$w_i = \frac{1}{rms_i^k}. \tag{3.8}$$

This weighting method was also utilized by Taylor et al. (2012). The theoretical rms of the stacked spectrum is then predicted as

$$rms = \sqrt{\frac{1}{\sum_{i=1}^{N} w_i}}, \tag{3.9}$$

which simplifies to equation 3.6 for homogeneous rms levels and $k = 2$.

The second weighting system uses normalized (N) weights given by the equation

$$w_i = \left(\frac{rms_{min}}{rms_i} \right)^k , \tag{3.10}$$

where rms_{min} is the lowest rms of all the spectra and k is again an integer constant (Taylor, 2010). The predicted rms using the normalized weights is given by the equation

$$rms = \frac{\sqrt{\sum_{i=1}^{N} rms_i^2 w_i}}{\sum_{i=1}^{N} w_i} \tag{3.11}$$

The purpose of these different approaches was to try and predict the behavior of the rms and confirm whether the stacking improves the sensitivity as expected. In reality, while the stacking utilizing the weights did show an improvement over the unweighted approach, there was no significant difference between using variance-defined or normalized weights. Therefore, given its relative simplicity, I decided to use the variance-defined weighting in all the actual stacking. For the actual value of k I set $k = 2$, following the choice done by Taylor et al. (2012) and Fabello et al. (2011). I also found that the actual stacked rms does not reach the upper or lower theoretical limits defined by the predicted rms curves. The behavior of the rms level with increasing number of spectra stacked is shown graphically in figure 3.23, accounting for both weighting methods.

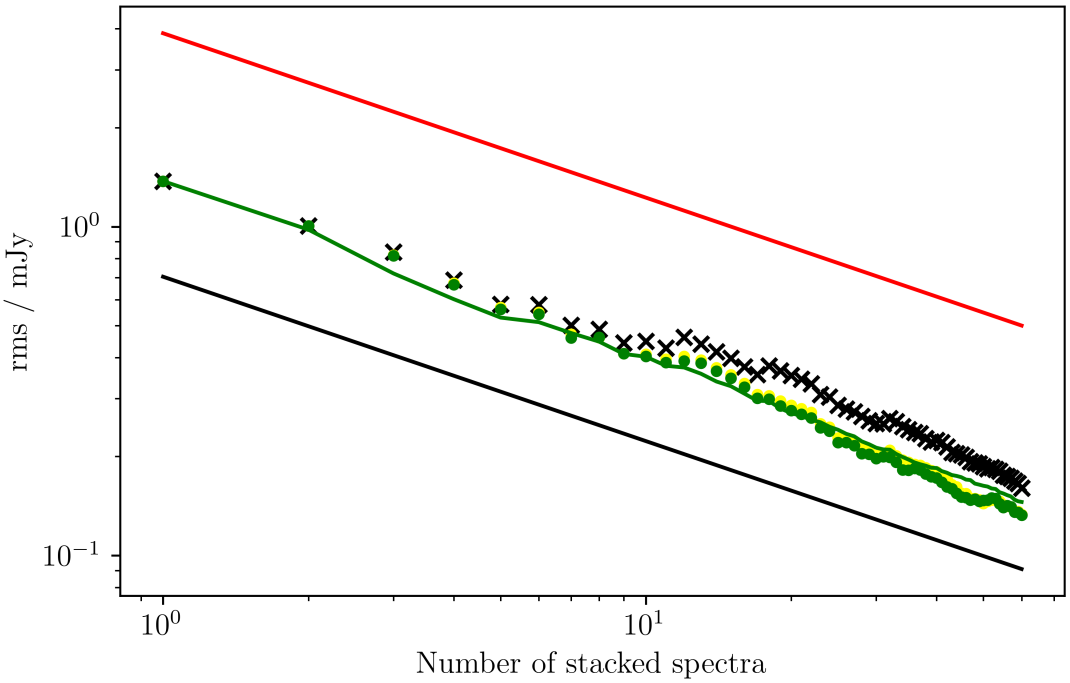

Figure 3.23: Effect of stacking up to 61 real undetected galaxies from the WAVES and VC1 regions. The red and black lines indicate the theoretical upper and lower rms limits respectively, using equation 3.6. The green curve shows the predicted rms behavior of the VD-weights. Black crosses, green and yellow points show the actual rms of the stack without weighting, with VD and N weighting respectively. Both axes are logarithmic.

Stacking results

For stacking the HI undetected galaxies in the WAVES region I used the GOLD-Mine catalog for the coordinates and velocity measurements. The filtering process was similar (but separate and more inclusive) to one described in section 3.2, with the same slight spatial overlap and the velocity range. I used the WAVES data cube to obtain majority of spectra, but I also used the AGES data cube, provided by R. Taylor, for the few objects which near the border where WAVES and AGES regions overlap to include as many spectra as possible. However, I did not stack all the objects from the full VC1 region, because that was already done by Taylor et al. (2012). I then cross-matched all these objects against VCS objects, using their optical coordinates and 1.75 arcmin separation. Lastly, I divided the sample into two groups, one only with late-type objects (27) and another one only with early-type objects (92). I did not trim either sample to the WAVES region, because for stacking it was preferential to try and stack as many objects possible, including the ones which could have been in the VC1 region.

For the actual stacking I created a pipeline composed of three `Python` scripts. The first script accepted the coordinates, velocity, the spectral range (total width of the spectrum) and then accessed `Miriad`, which measured the emission line using the supplied FITS data cubes. All measured parameters, including the spectrum were then saved in a `.txt` log file. If the object was partially or fully outside the used data cube (either WAVES or AGES), it was skipped. This was repeated for all the objects in the selected table.

The second script would generate `.png` images of all the spectra from the `.txt` log files. I manually inspected all of the images and decided whether or not to include the corresponding object in the stacking itself. Given the blind HI search discussed in section 3.1, it was unlikely that any new detections would result from this. However it is possible that some weak detections might be found that are more easily visible in the spectra than in the FITS data, as per Fabello et al. (2011); Taylor et al. (2012, 2013). If a spectrum was not suitable for stacking, e.g. it contained the Milky Way emission, I would discard its log file.

The third script would then perform the actual stacking using the `.txt` log files with the variance-defined weighting with $k = 2$. I tried many different combinations of stacked objects based on their morphology (late-type or early-type), data cube (WAVES or VC1) and their distance. Initially, I used a 2000 kms^{-1} spectral width, but many of the resulting objects had such a low velocity that their spectra contained Milky Way emission, which led to their elimination. For that reason I lowered the spectral width to 1000 kms^{-1} and stacked every combination again. That led to an increase of the number of stacked spectra by up to $10 - 25\%$. A larger bandpass allows for more accurate of the spectral baseline, but 1000 kms^{-1} should be sufficient for this (Taylor et al., 2012). Given the width of a single spectral channel 5 kms^{-1}, this accounts to roughly 200 channels (or 400 in case of the 2000 kms^{-1} bandpass). By contrast the typical spectral width of galaxies $\sim$ 100 kms^{-1}, as seen in figure 3.8, would correspond to roughly 20 spectral channels.

Selected examples of spectra of individual galaxies used in stacking in the WAVES region with the 1000 kms^{-1} spectral range is shown in figure 3.24.

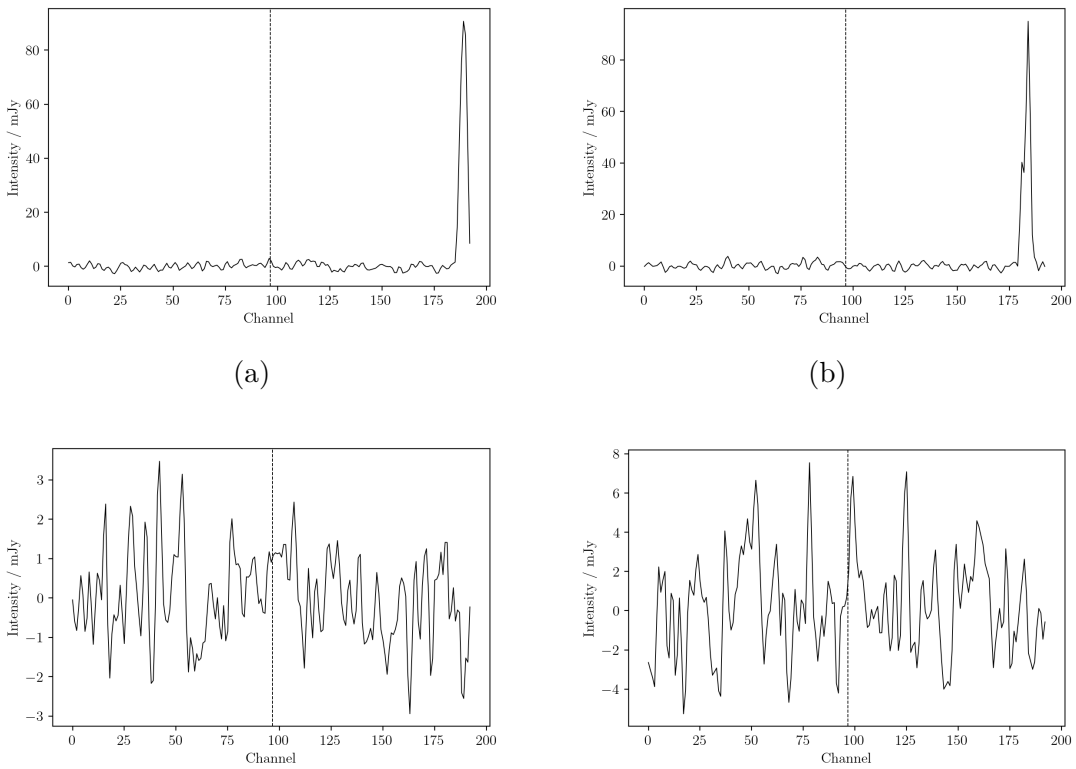

Figure 3.24: Individual measured spectra of galaxies obtained during the stacking process. (a) VCC 1078 and (b) VCC 920 were rejected due to the Milky Way emission, because of their low velocities. (c) VCC 856 and (d) VCC 1861 were both used for stacking. The horizontal channel axis is reversed in respect to velocity, which means the velocity is decreasing with channels. The dashed line shows the middle channel of the spectrum.

The resulting spectrum after stacking is shown in figure 3.25.

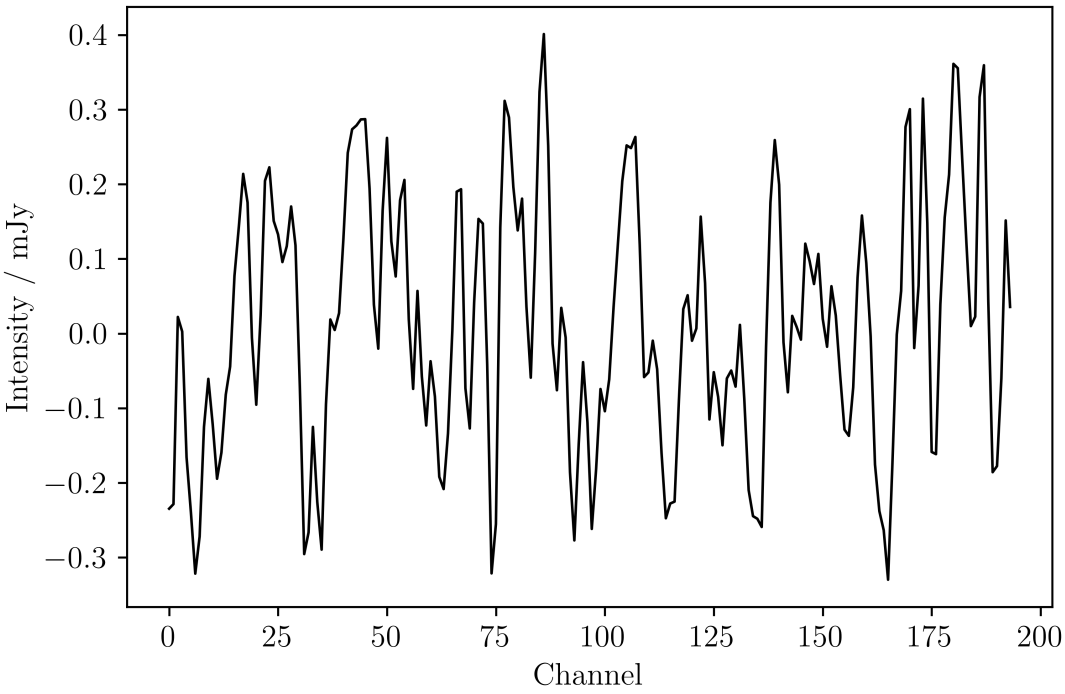

Figure 3.25: The resulting stacked spectrum from stacking 58 early-type galaxies in the WAVES region at all the distances. The horizontal channel axis is reversed in respect to velocity, which means the velocity is decreasing with channels.

The results showed no detection despite the *rms* decreasing to 0.17 mJy. This translates to a mass sensitivity of 1.72×10^6 $M_\odot$ assuming a 3 σ top-hat profile with a width of 50 kms^{-1} at 17 Mpc, using equation 1.5. The main results, including the combination description, how many spectra were stacked, achieved *rms* and mass sensitivity, are shown in table 3.6.

The combinations of stacked galaxies were based on morphology, distances and data set. The relation of gas and morphology has been well established. Late-type galaxies are worth stacking because they are much more likely to contain at least some gas, some of which could have been stripped or lost in some other way. And by stacking we usually hope to detect the remaining content. On the other hand, as early-type galaxies are much less likely to have any detectable HI, by stacking we can put a constraint on the amount of this gas, but the chance of finding a real detection remains low. Another factor is the distance due to the $\sim d^2$ dependence in equation 1.5. This can cause major changes in mass sensitivity at different distances while *rms* can remain unchanged. For that reason I also tried stacking only the closest objects at 17 Mpc, where we should achieve the best sensitivity. Other combinations of stacked objects, such as stacking all the early-type or all the late-type objects in the VC1 region, were already done by Taylor et al. (2012) and Taylor (2010), so I do not repeat them here.

Table 3.6: Main stacking results. The 2000 kms^{-1} and 1000 kms^{-1} show the spectral range of the stacking. The combination column describes what was stacked: LTG = late-type galaxies, ETG = early-type galaxies, N = the number of stacked spectra. The *rms* was calculated after performing 3 σ clipping on the resulting stacked spectrum. Mass sensitivity M_{HI} was calculated by assuming a 3 σ top-hat profile with a width of 50 kms^{-1} at 17 Mpc.

Combination	1000 kms^{-1}			2000 kms^{-1}		
	N	*rms* [mJy]	M_{HI} [$\times 10^6 M_\odot$]	N	*rms* [mJy]	M_{HI} [$\times 10^6 M_\odot$]
LTG, WAVES	10	0.410	4.19	9	0.448	4.58
ETG, WAVES	58	0.169	1.72	45	0.161	1.65
LTG, ETG, WAVES	69	0.148	1.52	54	0.146	1.49
LTG, AGES	2	0.981	10.00	2	0.965	9.87
LTG, ETG, WAVES, AGES	80	0.129	1.32	60	0.133	1.36
LTG, WAVES, 17 Mpc	6	0.561	5.73	5	0.596	6.10
ETG, WAVES, 17 Mpc	44	0.171	1.75	36	0.175	1.79
LTG, ETG, WAVES, 17 Mpc	50	0.150	1.55	41	0.166	1.70

None of the stackings revealed a detection, but I was able to put a constrain the average gas mass of the stacked populations, as shown in the table 3.6.

3.6 Notable objects

In this section I present objects which are in some way interesting or have previously unmentioned features. That includes the gas clouds, pairs of galaxies with unresolvable HI content, early-type galaxies with HI or other objects which do not follow the general trends.

3.6.1 Gas clouds in WAVES

VCS 9 (AGC 226178)

VCS 9 (AGC 226178) is a peculiar object located in the eastern part of the WAVES region at roughly 17 Mpc from us, with a velocity of 1580 kms^{-1} and an estimated HI mass of 2×10^7 $M_\odot$. VCS 9 is not an ordinary galaxy, but rather appears to be a cloud of stripped gas with very low surface brightness with stellar population consisting of detectable blue blobs. There are two theories trying to explain its origin, first considers the nearby galaxy NGVS 3543 to be the source of this gas, whereas the other one claims it is actually the more distant VCC 2034. I will expand more on this in chapter 4. The renzogram of VCS 9 is shown in figure 3.26.

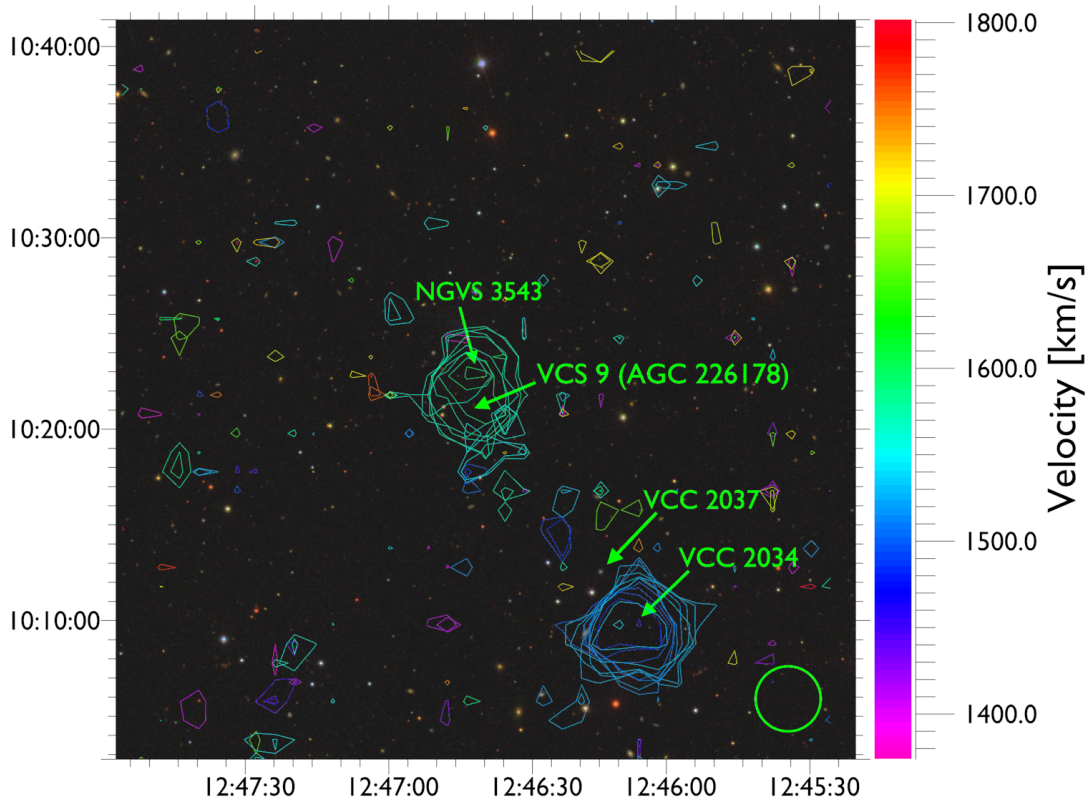

Figure 3.26: Renzogram of VCS 9. The green circle in the corner shows the 3.5 arcmin beam size.

VCS 18–21 (ALFALFA Virgo 7 complex)

As mentioned in section 1.4.1, the ALFALFA Virgo 7 complex is an unusually massive and extensive gas cloud in the Virgo Cluster. For a thorough analysis, using the same WAVES data as used here, see Minchin et al. (2019). The renzograms of the four objects which form the AV7 complex are shown here for completeness in figure 3.27.

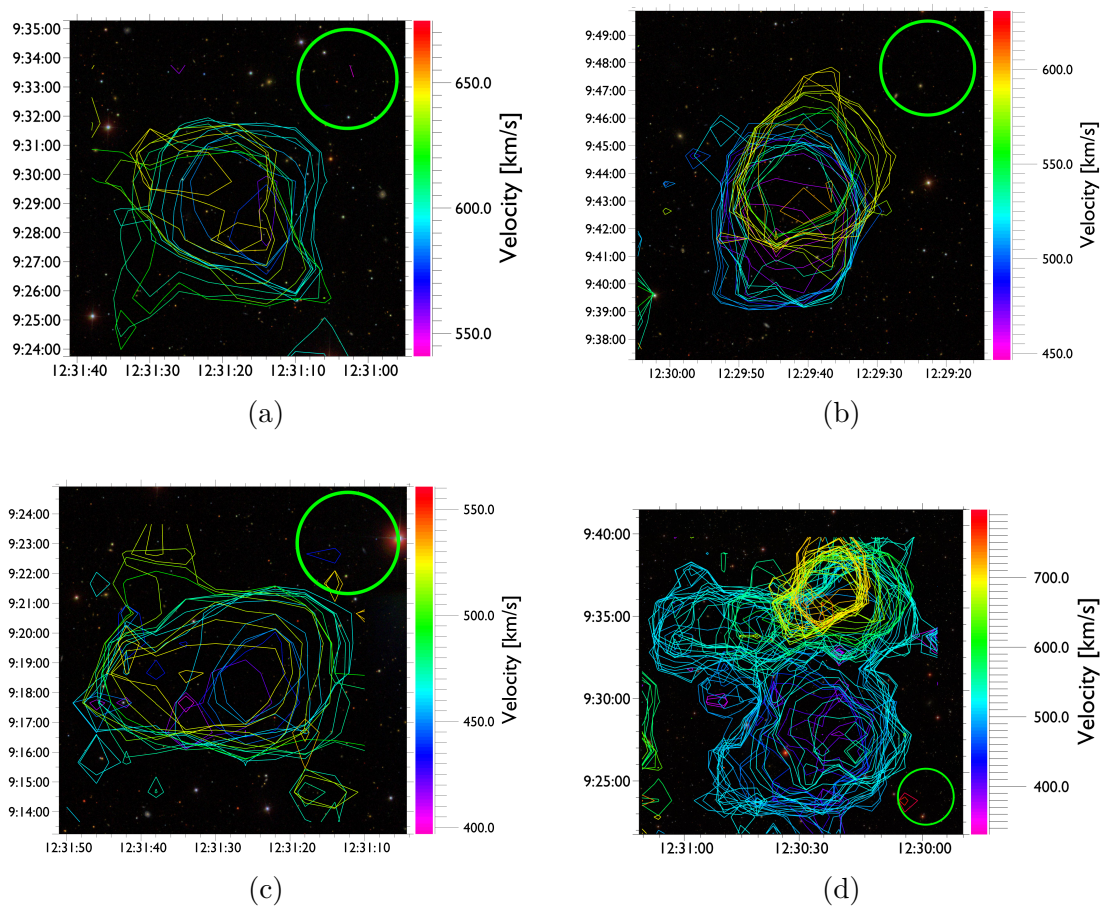

Figure 3.27: Renzograms of the four regions, which contain the ALFALFA Virgo 7 complex: (a) VCS 21, (b) VCS 18, (c) VCS 19 and (d) VCS 20. The green circle in the corner shows the 3.5 arcmin beam size.

Due to its odd nature I did not consider it a "typical" dark cloud, especially with its recent discovery of star forming region by Jones et al. (2024). A renzogram of the entire complex is shown in figure 3.28.

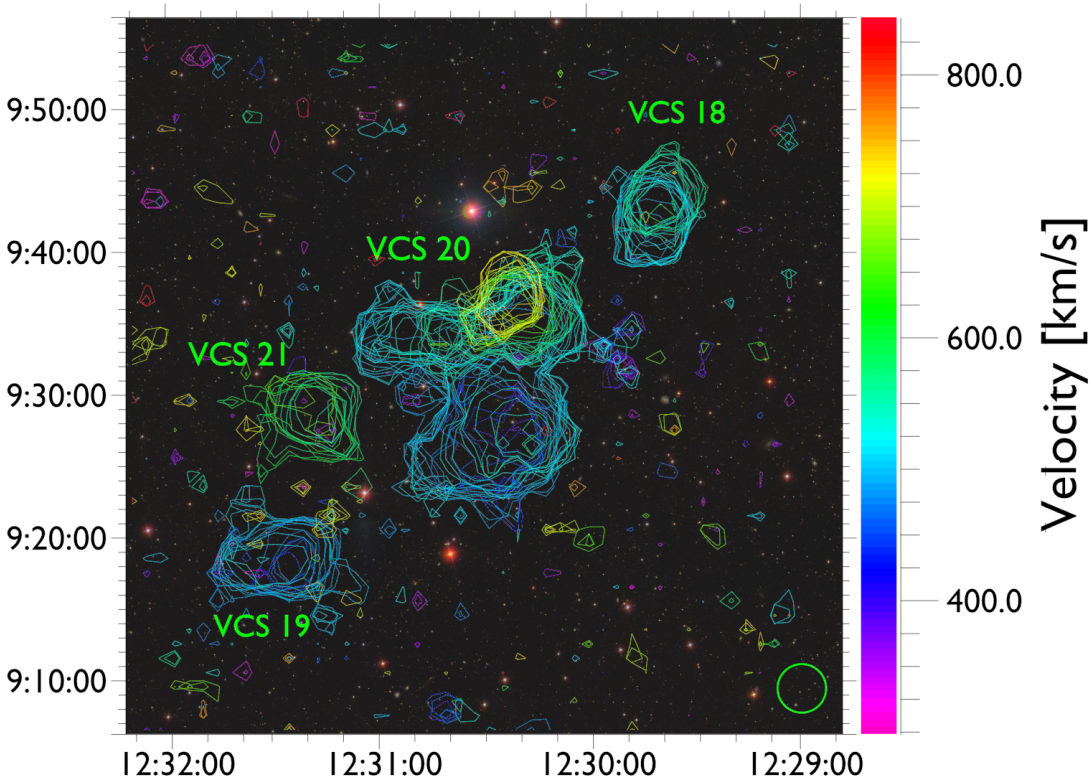

Figure 3.28: Renzogram of the entire ALFALFA Virgo 7 complex. The green circle in the corner shows the 3.5 arcmin beam size.

VCS 54

VCS 54 is located in the center region of the WAVES data set at a distance of 23 Mpc, has a mass of 3.6×10^7 $M_\odot$ and velocity of 954 kms^{-1}. It does not appear to have an optical counterpart, which makes it the only dark cloud I detected in the WAVES region. It is most likely associated with a late-type galaxy VCS 40 (VCC 952), which is $\sim$ 10 arcmin (or 66 kpc) due SW, as seen in figure 3.29.

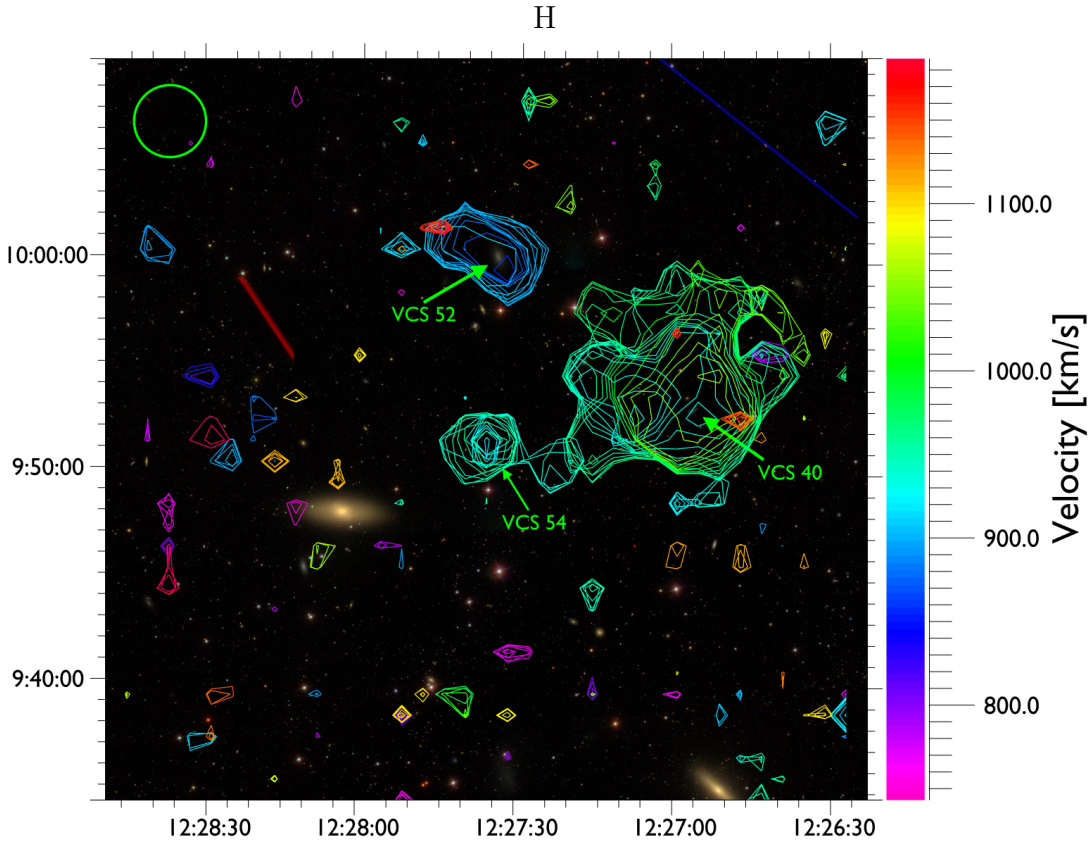

Figure 3.29: Renzogram of VCS 54, VCS 40 and the surrounding region. The data cube was Hanning smoothed along the velocity axis over 5 channels. The green circle in the corner shows the 3.5 arcmin beam size.

3.6.2 Pairs of galaxies with unresolved HI gas

VCS 2 (VCC 1676/1673)

VCC 1676 and VCC 1673 are a pair of spiral late-type galaxies located at the northern edge of the WAVES data cubes 17 Mpc from us. They are in the early stages of merging, with high star-formation rates in the contact regions and are currently exchanging gas (Kaneko et al., 2010). I detected their HI emission as VCS 2, with a mass of 4.3×10^8 M and a velocity of 2240 kms^{-1}. But due to being at the edge of the data cube, it is partially cut off, as is seen in figure 3.30.

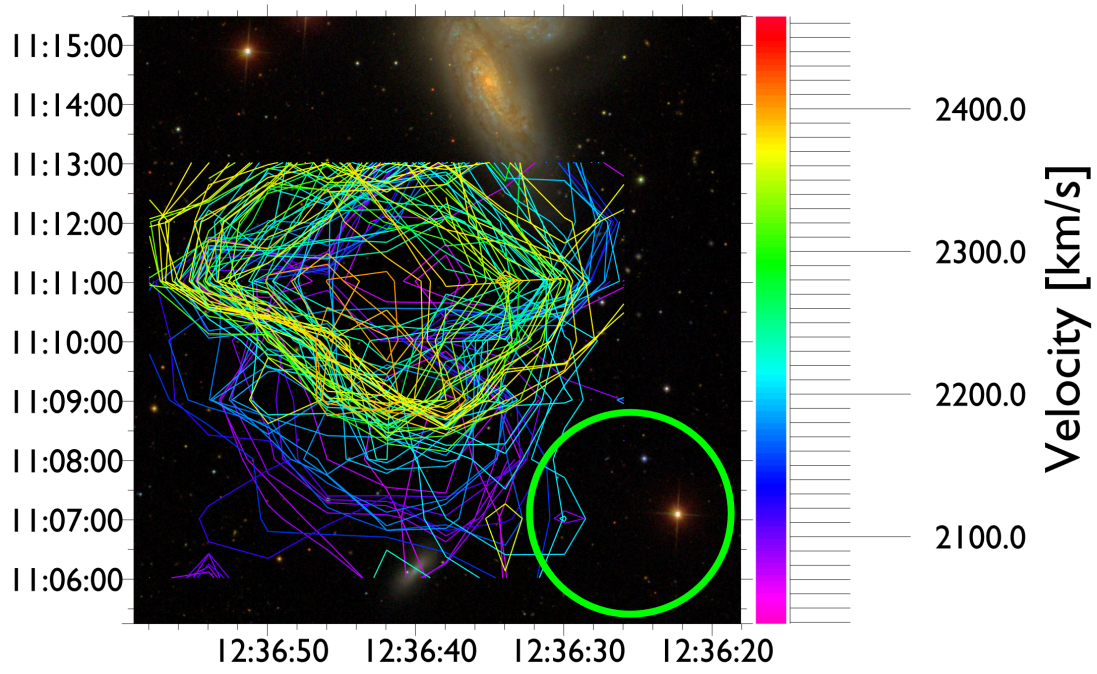

Figure 3.30: Renzogram of VCS 2. The green circle in the corner shows the 3.5 arcmin beam size.

Because we cannot distinguish which portion of the HI gas is associated with which galaxy, they were not suitable for analysis of how gas relates to galaxy evolution.

VCS 7 (VCC 2062/2066)

VCC 2066 is a disturbed lenticular galaxy associated with a faint dwarf galaxy VCC 2062, located in north-western part of the WAVES region, with velocity of 1160 kms^{-1} and approximately 17 Mpc from us. On the sky, they are separated by roughly 4 arcmin ($\sim$ 20 kpc), which makes their HI emission unresolvable in the WAVES data. Their common renzogram is shown in figure 3.31.

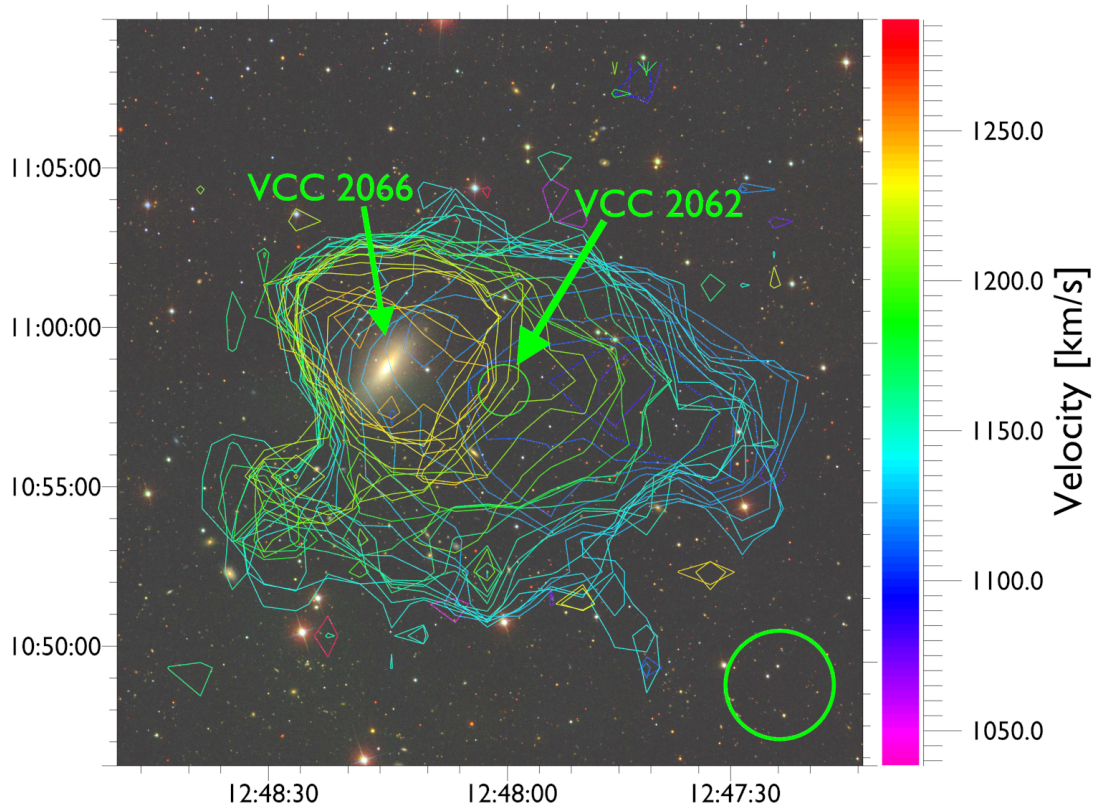

Figure 3.31: Renzogram of VCS 7 (VCC 2066/2062). The green circle in the corner shows the 3.5 arcmin beam size.

VCS 36 (VCC 905/939)

VCC 905 and VCC 939 are a pair of face-on, visually similar spiral galaxies, at the southern edge of the WAVES region at the distance of 23 Mpc. They are separated by ~ 4 arcmin (~ 27 kpc), which makes their HI emission unresolvable in the WAVES survey. The total HI mass is estimated at 5.2×10^8 $M_\odot$ and its velocity of 1278 kms^{-1}. The renzogram of VCS 36 is shown in figure 3.32.

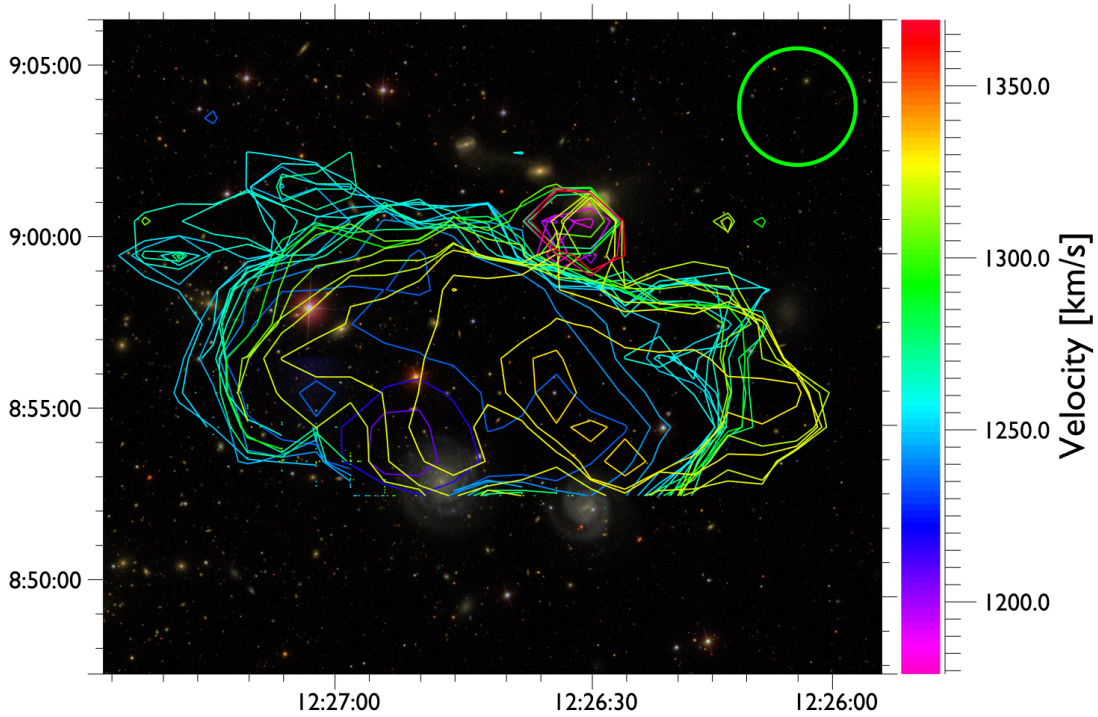

Figure 3.32: Renzogram of VCS 36. The green circle in the corner shows the 3.5 arcmin beam size.

3.6.3 Early-type galaxies with HI

VCS 11 (VCC 1964)

VCS 11 is located in the SE part of the WAVES data region, at roughly 17 Mpc away, with a velocity of 1429 kms^{-1} and an HI mass of 3.2×10^7 M$_\odot$. It is associated with an ultra diffuse galaxy candidate VCC 1964 but the gas itself seems to be offset from the optical emission, perhaps as a result of ram pressure, as is shown in figure 3.33.

VCC 1964 is classified as an early-type galaxy, specifically dwarf elliptical, making it one of only 3 ETGs with an HI content in the WAVES region. This in combination of the fact that there are not many UDG candidates in the Virgo Cluster and its disturbed gas, make it an important object of study.

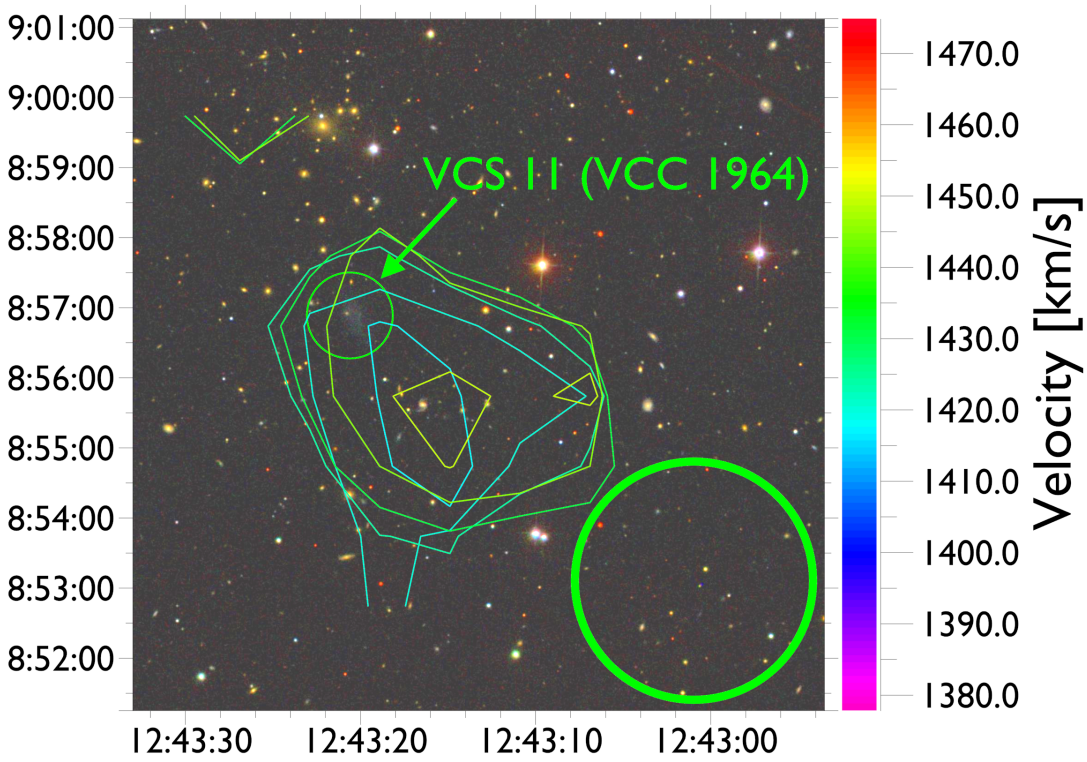

Figure 3.33: VCS 11 renzogram. The green circle in the corner shows the 3.5 arcmin beam size.

VCS 47 (VCC 21)

VCS 47 is located in the western part of the WAVES region, has a velocity of 502 kms^{-1}, HI mass of 4.0×10^7 M$_\odot$ and it is 17 Mpc away from us. It is another early-type galaxy, specifically a dwarf spheroidal. Its renzogram is shown in figure 3.34.

VCS 51 (VCC 651)

VCS 51 is located lower-center part of the WAVES region roughly 23 Mpc away with a velocity of 964 kms^{-1} and an HI mass of 1.7×10^7 M$_\odot$. This final early-type galaxy detected in HI is a classed as a dwarf elliptical. Its renzogram is shown in figure 3.34.

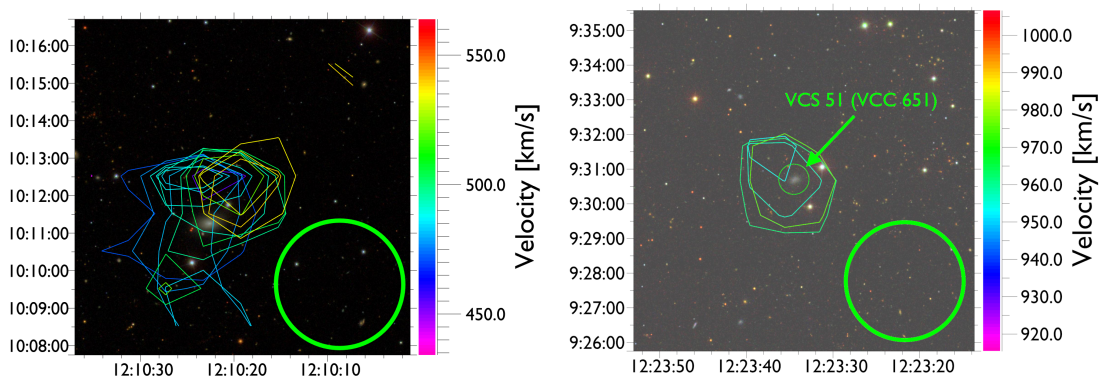

(a) (b)

Figure 3.34: Renzograms of VCS 47 (a) and VCS 51 (b). The green circle in the corner shows the 3.5 arcmin beam size.

3.6.4 Other exotica

VCS 10

VCS 10 is a blue irregular galaxy located in the NW part of the WAVES region at 17 Mpc distance from us. It is optically very small but has an HI mass of 1.7×10^7 $M_\odot$ and a velocity of 1614 kms^{-1}. That makes it the bluest object in the VCS catalog with $g - i = -0.2$, also visible in the CMD in figure 3.16. This is further consistent with its relatively high HI to stellar mass fraction of ≈ 18.5, as compared to more typical $\sim 0.01 - 5$ with the rest of the VCS objects. Its renzogram is shown in figure 3.35.

VCS 44 (VCCA 52)

VCS 44 is a late-type galaxy located at the SW edge of the WAVES region, with velocity of 1934 kms^{-1}, HI mass of 8.0×10^8 kms^{-1} at a distance of 32 Mpc from us. It is particularly interesting because it has the highest HI to stellar mass fraction of ≈ 27.1. Photometry for this object was measured manually, which should assure its correctness. Its renzogram is shown in figure 3.35.

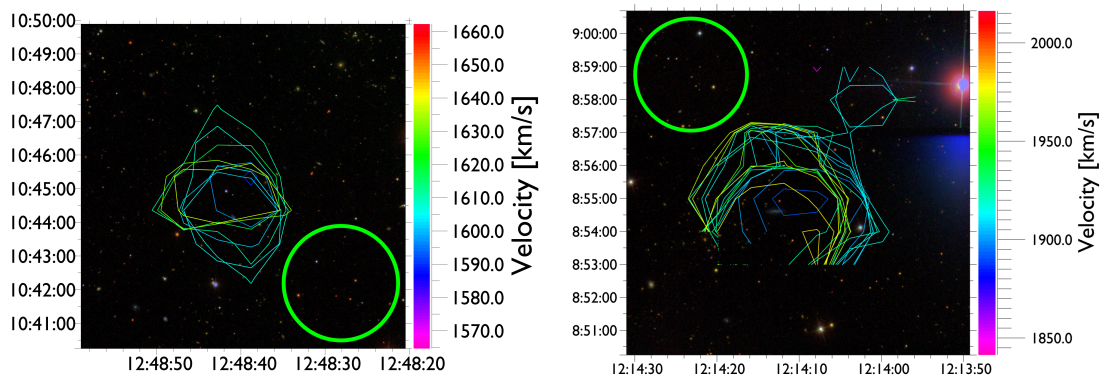

(a) (b)

Figure 3.35: Renzograms with SDSS images of VCS 10 (a) and VCS 44 (b). The green circle in the corner shows the 3.5 arcmin beam size.

4. Discussion

I used the data from the 21 cm emission line survey WAVES, conducted by the Arecibo radio telescope prior to its collapse. The surveyed area used in this work was 2×10 deg^2 centered on the filament spine between M87 and M49 in the Virgo Cluster. The mean rms of the survey was 1 mJy. Using this data I cataloged 55 HI sources, for which I also assigned optical counterparts where possible. In total the VCS catalog includes 45 late-type galaxies, 3 early-type galaxies, 1 previously unknown dark cloud, 1 gas cloud with detected star formation and the ALFALFA Virgo 7 complex. To provide a comparison sample of HI non-detected objects, I complied a catalog using the GOLDMine catalog (73 objects) and NED (13 objects) database, which accounted for 86 galaxies, 72 early-types and 14 late-types. I obtained radius and photometry measurements from SDSS for objects in both the HI and non-HI catalogs, filtering the VCS catalog to only include galaxies with good photometry measurements. This resulted in a final table of 46 HI detected galaxies and 86 non-detected galaxies with good photometric data. In this section I use these catalogs throughout the analysis unless stated otherwise.

4.1 WAVES and VC1 comparison

4.1.1 Spatial and velocity distributions

As galaxy evolution is not observable in real time, it is necessary to observe galaxies at different stages of their evolution to understand it. For that reason I compare the results from the WAVES region to the VC1 region, which is centered on the Cluster B and M49, directly south of the WAVES region. These two regions are similar in their total area covered and the same technological setup used to observe them. This means we can use these data sets to easily make a direct comparison of these two regions of the Virgo Cluster.

WAVES and VC1 are also similar in physical properties of the objects they host. The HI mass and the W20 distributions are not fundamentally different as is seen in figure 3.8. This is further supported by the MW and KS test, which cannot reject the null hypothesis of the same distribution. As shown in subsection 3.5.1, this demonstrates the successful ability of WAVES to recover sources at a comparable sensitivity to AGES and with a similar accuracy. In fact, the WAVES area even contains a larger fraction of low-mass objects, so the slightly lower sensitivity of WAVES (relative to AGES' 0.6 mJy) is clearly not an issue. The VC1 area includes 81 galaxies detected in HI with good photometry measurements (74 late-type and 7 early-type), a sample which has had similar filtering done as with the sample of 46 VCS galaxies with good photometry used in this work (43 late-type and 3 early-type).

The spatial distribution of HI detected and HI non-detected galaxies in the WAVES region, as seen in figure 3.10, shows that overall they are distributed rather uniformly, but galaxies with HI content seem to be clumped close to the filament spine of the cluster and then directly west of it between $182 < RA < 185$. This is somewhat surprising, as on the large-scale HI detections tend to be more uniform than the non-detections (Dressler, 1980). The galaxies in a clump near

the filament spine are likely due to the contribution of Cluster B objects at 23 Mpc. The group to the west of the spine consists exclusively of objects at 17 Mpc, which may be recent arrivals (as I discuss later) infalling into the main body of the cluster. This is visible from the 17 and 23 Mpc RA histogram plots, shown in figure 3.12. They also show the 23 Mpc HI-detected objects occupy roughly the same RA, although the statistical tests claim otherwise. But their result may be skewed due to the VC1 region containing more than twice as many objects at 23 Mpc and hence changing the shape of the distribution enough for the tests to reject it.

It is important to account for the unreliability of distance measurements, especially of Cluster B and the M49 galaxy in this case. While in its sky position M49 lies directly in the center of Cluster B, the distance claimed for M49 itself is substantially different for other members of Cluster B. Gavazzi et al. (1999) and Boselli et al. (2014) both claim the Cluster B is at 23 Mpc, whereas M49, along with many objects which are projected within the bounds of Cluster B are all at 17 Mpc. This is particularly visible in figure 3.5. Gavazzi et al. (1999) acknowledged this problem and proposed an alternative division of the Virgo Cluster into slightly different substructures, where M49 is a member of "Cloud S" (see figure 6 in Gavazzi et al. 1999). In this work I followed the structure laid out by Boselli et al. (2014), who also claims that M49 is the central galaxy of Cluster B but does not elaborate on this further. There is no clear resolution to this in the literature, and this is still a prime example of how uncertain the extragalactic distance measurements are and how we need be aware of large inconsistencies.

Based on the total number of VCC members and HI detections (here including those at all velocities regardless of photometric measurements), the projected galaxy densities equal roughly 14.8 and 14.1 for WAVES and VC1 respectively, which is very similar. But the fraction of HI detected galaxies to the total number of galaxies in the WAVES region ($\approx 15.5\%$) is much smaller than in the VC1 region ($\approx 28.7\%$). Such a large difference may signify that the WAVES region is more relaxed and evolved, as its objects have had more time to lose their gas through environmental processes, most likely ram pressure stripping.

Out of the 81 HI-detected galaxies in VC1, there are 27 at 17 Mpc (33.3% of the total sample), 33 at 23 Mpc (40.7%) and 21 at 32 Mpc (26.0%). In contrast, most of the HI-detected galaxies in the WAVES region are concentrated in the main body of the cluster at 17 Mpc (60.9% of the sample with good photometry). This likely reflects the fact that VC1 contains more objects from the infalling clouds which have higher velocities. The difference in distributions can also be inferred from the velocity histogram in figure 3.14, in form of the high-velocity tail of the VC1 HI detected population. Compared to the HI detected objects in WAVES the difference is confirmed by the MW test (although KS test is inconclusive). The presence of infalling clouds, which have not yet merged with the rest of the cluster further suggests that the VC1 region is likely still forming and is hence less evolved relative to the WAVES region. This is not definitive evidence, but it is consistent with the idea of WAVES being more relaxed. This difference in distributions disappears when constricting the velocity histogram to the main body objects as is seen in figure 3.15.

4.1.2 Dark cloud populations and gas loss

Besides the velocity distributions, the signs of relaxation are perhaps also seen by the presence of dark clouds. Taylor et al. (2012) reported on 8 dark[1] clouds within the VC1 region, with median HI mass of 2.15×10^7 $M_\odot$. These clouds were isolated without a clear galaxy of origin, typically more than 100 kpc from the nearest galaxy. If WAVES were to detect dark clouds at a similar rate to those found in VC1 (8 out of 95 detections), we would expect to find about 4 or 5 dark clouds here. However, this is not the case as WAVES contains only genuinely one dark cloud (VCS 54), which does not appear to have any optical counterpart and is not as isolated (see below). Even if we included the VCS 9 gas cloud (see subsection 4.3.1), which is not dark but contains star-forming regions, there would still be a discrepancy. Especially since WAVES contains more objects at 17 Mpc than VC1, which gives us better mass sensitivity.

While VCS 54 has a similar HI mass (3.6×10^7 $M_\odot$) it is markedly different from VC1 dark clouds because VCS 54 is not isolated: it is connected via a stream to VCS 40 (VCC 952), as seen in figure 3.29. This likely indicates it is being stripped via tidal interactions or ram pressure stripping (although the precise nature of the gas removal mechanism still needs to be confirmed). The absence of more dark clouds is consistent with the idea of relaxation of the WAVES region, as other clouds would have had enough time to disperse or collapse. The fact we are observing VCS 54 might be because VCS 40 only recently started losing gas, i.e. if it is a new arrival to the cluster.

VCS 40, the likely parent of VCS 54 is an irregular late-type galaxy with an HI mass of 1.4×10^8 $M_\odot$, $M_{HI}/M_\star$ of 6.1 and an HI deficiency of 0.25 (containing a roughly normal amount of gas). If we add the VCS 54 HI mass to VCS 40, then its HI deficiency decreases to 0.15 and the $M_{HI}/M_\star$ raises to 7.7, which is not unreasonable compared to the rest of the sample. This shows that while a galaxy can lose a considerable amount of gas, it does not necessarily make it HI deficient. Vice versa, HI deficiency alone, while related, is not evidence for currently ongoing stripping (Taylor et al., 2020). In fact most ($\sim 69\%$ of the total 13) of the galaxies with a recorded HI tail (or a hint of one) are less deficient than 0.6, as shown in figure 4.1. This means the galaxies that are currently undergoing gas stripping have relatively low HI deficiency, while the rest must have already lost their gas in the past (Köppen et al., 2018).

For the particular case of VCS 40 / VCS 54, an alternative explanation is possible. It could be that VCS 54 is a dwarf galaxy merging with VCS 40, rather than VCS 40 losing gas. However no optical counterpart is visible for VCS 54, and its additional gas would not imply VCS 40 was (initially) unusually gas-rich. Given the rarity of mergers in clusters due to their high velocity dispersion, gas removal seems a more likely explanation for this system. It is also interesting that VCS 40 is not more HI deficient since it is located very close to the filament spine, which is filled with the dense X-ray gas, and the RPS should be most effective there. This is evident from figure 4.1.

[1]Although recent VLA observations by Minchin and Taylor (2023) located faint optical counterparts in two of these clouds, the following comparison is still fair as I followed the same procedure as Taylor et al. (2012).

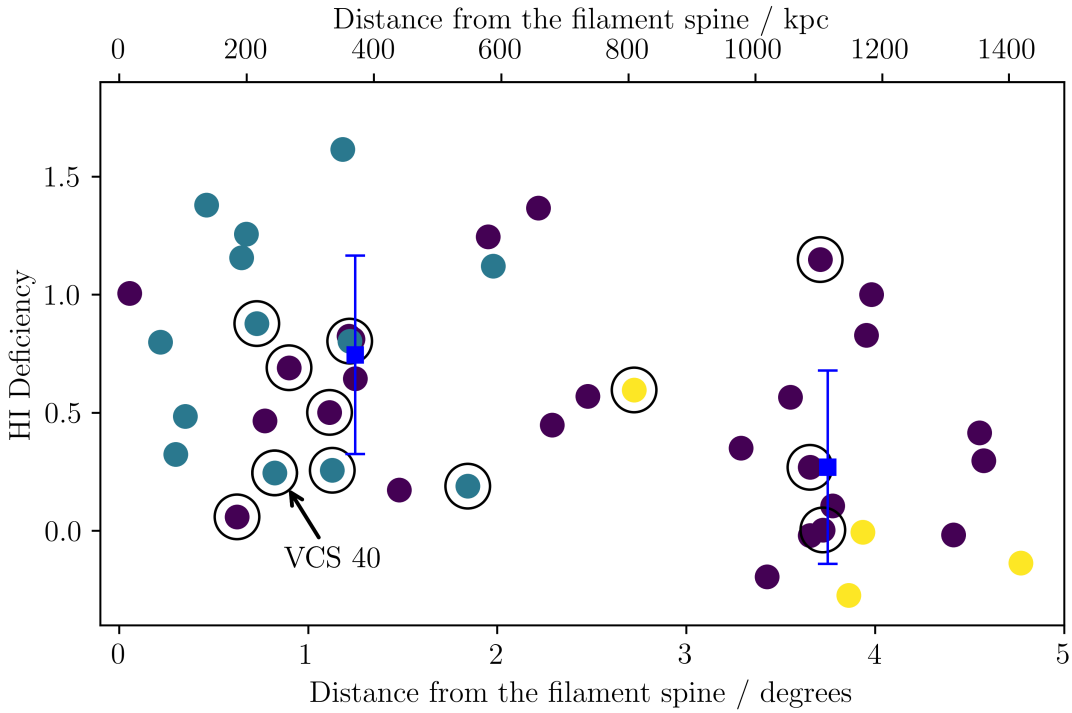

Figure 4.1: HI deficiency as a function of distance from the filament spine in degrees and projected distance at 17 Mpc in kpc. VCS 40 is shown. Colors show distances: purple = 17 Mpc, blue = 23 Mpc and yellow = 32 Mpc. Encircled points show galaxies with an HI tail or a hint of one (13 in total).

4.1.3 Distribution of HI deficiency

The figure 4.1 likely shows the effect of density of the hot ICM on the efficiency of RPS, as we have two groups in two different environments separated at around 3 degrees from the filament spine. The group closest to the spine is embedded in the ICM, where the RPS is expected to be relatively strong. In contrast the other group still lies on the outskirts and their galaxies contain a more typical amount of HI gas. The effect of the hot ICM gas is further evident from the plots in figure 3.21, which include both WAVES and VC1 data, especially those plotting distance from M49 and the filament spine. We see that around the M49 galaxy the deficiency of VC1 objects is the highest and decreases with distance throughout the WAVES region. The M87 plot does not show any clear trend because of its greater distance from VC1.

We can also see in figure 3.21 that the HI deficiency decreases with the distance from M49, M87 or the filament spine throughout all the different subclusters, despite their different distances (each is roughly 1 Mpc in diameter but separated by $\sim 6 - 9$ Mpc) This is also visible in plots in figure 3.21. This seems strange since each subcluster is rather independent of each other, likely embedded in its own different X-ray gas cloud, and should hence show different trends.

The HI deficiency-distance plots (see figure 3.21) have high scatter which can be for a number of reasons. For one, a given galaxy might have lost its gas and become HI deficient in the past and only later moved to the outskirts, where we see it now. Or on the other hand, it could have lost its gas and become

gas-poor before even entering the cluster, an effect known as "pre-processing" (for more see Lopes et al. 2024). Another reason might be uncertainty of the distance estimations used in this work, as discussed in section 3.1. Nevertheless, the general trends of HI deficiency decreasing with the distance from the dense parts of the cluster (M87, M49 or the filament spine) are generally clear and confirmed by the t-test up to a 99.8% confidence level.

On the other hand, the spatial HI deficiency scatter plot, in figure 4.2, clearly shows that the most deficient objects are members of the Cluster B at 23 Mpc, while the 17 Mpc objects have more typical amounts of gas. This seems to be contradictory to the relaxation hypothesis proposed earlier. But most of the 17 Mpc HI-rich objects are actually on the outskirts of the cluster (as projected on the sky) whereas the objects in the inner parts of the cluster at the same distance are completely devoid of HI and only detected in the optical VCC catalog. Once we account for the projected distance, we see that the 17 Mpc galaxies here are indeed likely recent arrivals and so not likely to have lost much of their gas. It seems that in this particular region, the galaxies at 17 Mpc are of two different populations: the non-detected galaxies, which may have arrived earlier in the cluster and so already lost their gas, and the detected galaxies, which are mainly on the outskirts and still infalling. This is in contrast to VC1, which contains populations at many different stages of their evolution within the cluster.

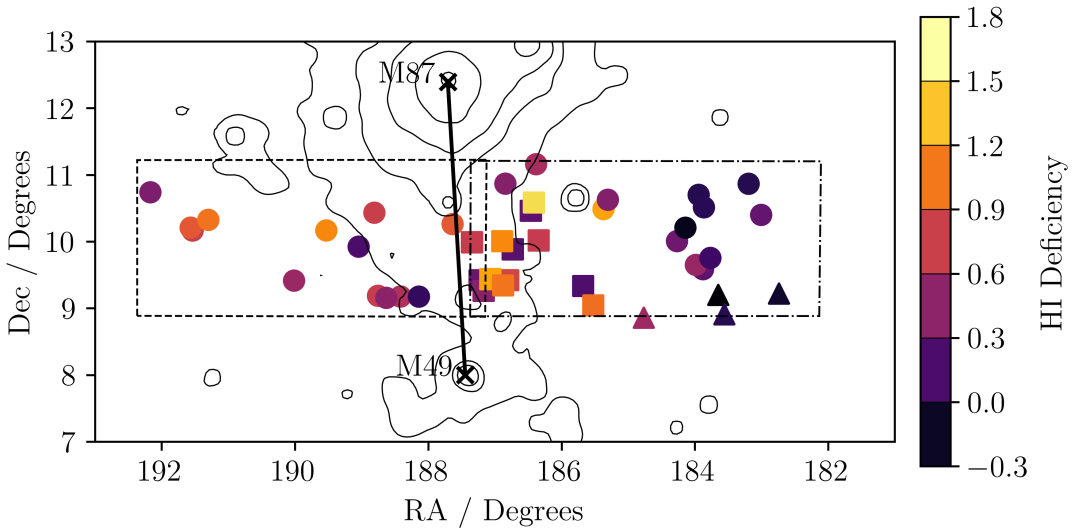

Figure 4.2: HI deficiency scatter plot. Symbols show distances: circles = 17 Mpc, squares = 23 Mpc and triangles = 32 Mpc.

4.2 Gas-loss driven galaxy evolution

4.2.1 Dwarf elliptical and spheroidal galaxies

The morphology distributions of HI detected and non-detected objects follow the general expected trends, but include some outliers, as seen in figure 3.13. The first early-type galaxy is the dwarf elliptical (dE) VCS 11 (VCC 1964) is also an ultra diffuse galaxy (UDG) candidate. While potentially interesting on its own, it would require a dedicated study to confirm and it should not affect any of the

following discussion, but it might have consequences for understanding UDGs in clusters. The other two early-type galaxies are the dE VCS 51 (VCC 651) and the dwarf spheroidal (dS0) VCS 47 (VCC 21). There is of course a possibility of morphology misclassification as the VCC morphology types assigned by Binggeli et al. (1985) used photographic plates rather than a modern CCD camera and visual inspection is always subject to errors and uncertainties. And this issue is only amplified with low surface brightness objects, such as the aforementioned dwarf galaxies, even with modern instruments. However, this seems unlikely in this case as from the brief examination of the SDSS images they do appear quite smooth and without any significant structure.

Additionally, VCS 11, 47, and 51 contain relatively low HI-to-stellar mass ratios when compared to their stellar masses, as illustrated in the mass-to-light ratio diagram shown in figure 4.3. This is in contrast to the VC1 region, where Taylor et al. (2012) also identified several dE galaxies but with significantly higher gas fractions. Taylor et al. (2012) suggested that the gas-rich dE galaxies are either recent arrivals to the cluster or, given their similarities to dI galaxies, were merely misclassified as dE. If classified correctly, these findings would somewhat contradict the model proposed by Boselli et al. (2008), which supposes that dwarf irregular galaxies within clusters transition into dwarf elliptical galaxies as a result of gas removal, rendering them relatively gas-poor. While definitive conclusions cannot be drawn from a handful of objects, the identification of dE galaxies with low gas fractions in this study provides supporting evidence for this notion of gas-loss-driven evolution of dwarf irregular galaxies.

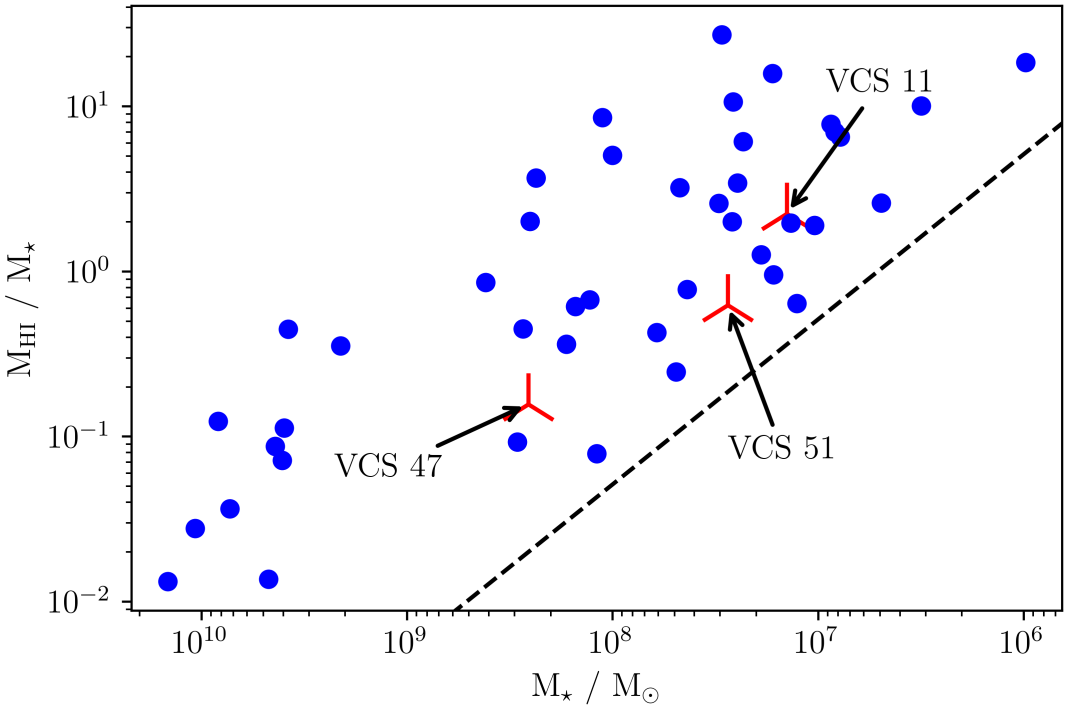

Figure 4.3: Mass-to-light ratio diagram with stellar mass. Blue points are the VCS late-type galaxies and the red tri-axial symbols are the VCS early-type galaxies.

More information is offered by the color-magnitude diagram, shown in figure

4.4. It shows that the three early-type galaxies with HI content are indeed different from the other ETG as they lie well within the blue cloud, making them some of the bluest early-type galaxies in the WAVES region. This fact together with the low gas fractions of VCS 11 and VCS 51 and their low HI mass suggests that if the gas removal really occurred, it must have happened fairly recently. However, further research, such as deeper imaging or study of their star formation activity, is required to determine the actual scenario that took place. Either way, this is again in contrast to the dE galaxies detected in the VC1 region, where they were, apart from being gas-rich, also much redder and in fact located on the red sequence, as is seen in figure 4.4. It also further suggests that they are different from the dE objects detected in this work.

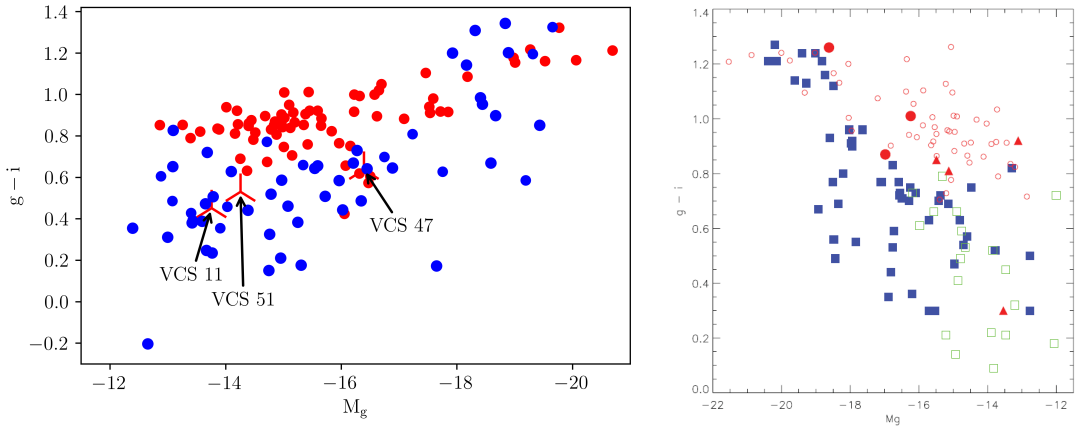

(a) (b)

Figure 4.4: (a) Color-magnitude diagram of the WAVES region with highlighted early-type galaxies with HI, VCS 11, 47 and 51. Red and blue points show early and late type galaxies respectively, whether or not they contain HI. (b) Color-magnitude diagram of the VC1 region by Taylor et al. (2012). Blue squares show late-type objects, red open circles show early-types, filled red circles are S0s, green open squares are non-VCC objects and red triangles are dE galaxies detected in HI. Note that the horizontal axis is inverted with respect to figure (a).

Moreover, from the figure 4.5 VCS 11 seems to have disturbed gas, although this is marginal, mainly indicated by the optical galaxy being off-center from the HI emission. This could signify active stripping of gas, although stronger evidence is needed to confirm. Meanwhile, VCS 47 shows a slight hint of disturbance and VCS 51 does not show any disturbance at all, rather a typical HI profile, as shown in figure 4.6. So, while they also may be in the process of gas removal, it is not possible confirm this due to their weak signals. Or, if either one is moving along our line of sight, it may be stripping, but the tail would be oriented towards or away from us, hence rendering it indistinguishable to us.

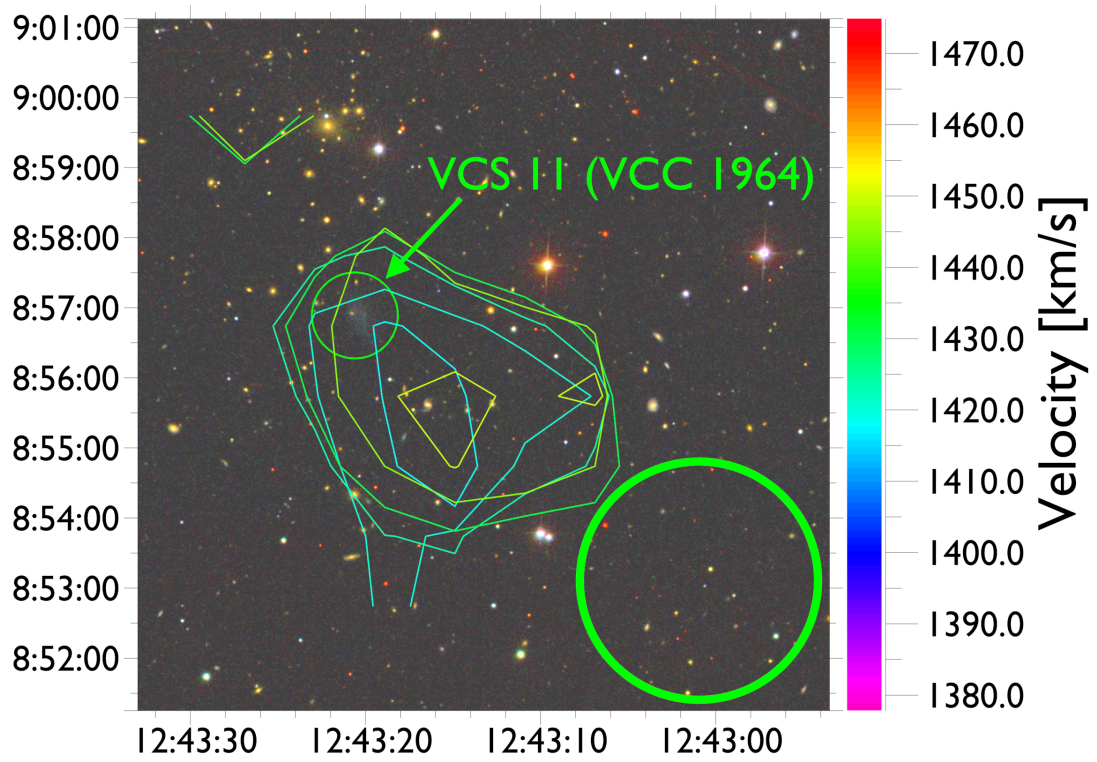

Figure 4.5: Renzograms of VCS 11. The green circle in the corner shows the 3.5 arcmin beam size.

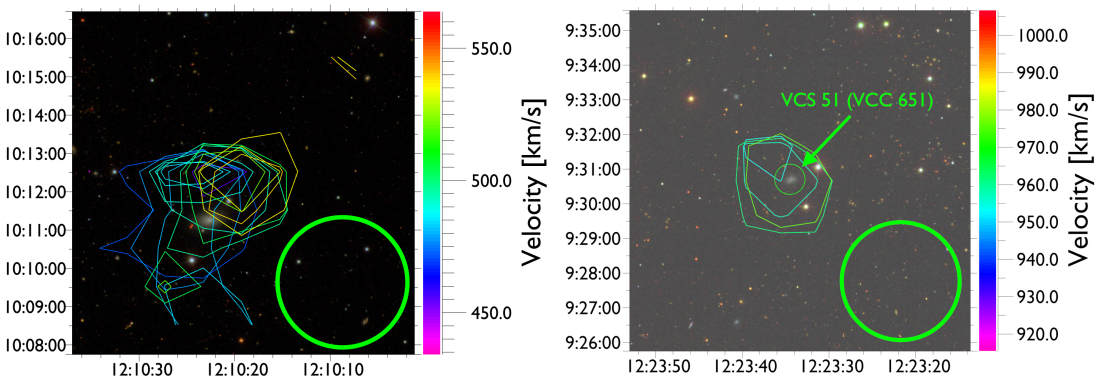

(a) (b)

Figure 4.6: Renzograms of VCS 47 (a) and VCS 51 (b). The green circle in the corner shows the 3.5 arcmin beam size.

4.2.2 Stacking

The three aforementioned early-type galaxies have an HI content, but what about the rest? In WAVES there are a further 72 early-type galaxies (with good photometry and velocity measurements, see table 3.3), which were not detected in HI at all. Through stacking of many different combinations of objects, I was able to achieve much better mass sensitivity than the nominal one as is shown in table 3.6. We can also see from this table that in some combinations a larger number

of stacked objects with the 1000 kms^{-1} bandpass is not necessarily a guarantee of lower *rms*. This is likely because the baseline might not be fitted very well, due to its shorter span, which results in systematically higher *rms*. Nevertheless, the best *rms* achieved in this work was 0.129 mJy after stacking 80 spectra in total from WAVES and VC1, all morphologies and at all distances. This translates to a mass sensitivity of 1.32×10^6 M$_\odot$, assuming the 3σ tophat profile with 50 kms^{-1} width at 17 Mpc, which is similar to the value[2] of 0.9×10^6 M$_\odot$ achieved in VC1. Both of these results support conclusions by Taylor et al. (2012) that the galaxies in the cluster which were not detected in HI visually likely contain little or no gas. As Taylor et al. (2012) state, this is somewhat in contrast to the field galaxies, which were not initially detected, but after stacking do seem to posses at least some amount of gas, as has been reported by e.g. Fabello et al. (2011)and Deshev et al. (2022). This indicates that galaxies in clusters are indeed very different from the field ones, i.e. with a limiting HI mass threshold below which there is no gas at all.

4.3 Notable objects and other exotica

Finally, the WAVES region also contained some notable objects which did not fit in the analysis described earlier or deserve additional attention. Some of these objects include the pairs of galaxies with unresolvable gas, the gas clouds or they show extreme properties with compared to the rest of the sample.

4.3.1 VCS 9 (AGC 226178)

As described in subsection 3.6.1, VCS 9 (AGC 226178) is a peculiar gas cloud with detected star-forming regions. There are two main theories which try to explain its origin. Junais et al. (2021) claims that the HI detection (VCS 9 in this work) is associated with a low surface brightness dwarf (NGVS 3543) located ~ 5 kpc to the north of the center of the HI cloud. They suggest that this is a blue ultra diffuse galaxy (UDG) which has undergone a RPS event over the last few hundred million years, turning it into a gas-poor red UDG. The authors estimate a stellar population of VCS 9 with a mean age of 20 Myr, which must have formed after the RPS event during an episode of star formation. However, NGVS 4543 does not have a known velocity measurement, which makes it difficult to confirm as the source of the VCS 9 gas cloud. On the other hand Jones et al. (2022) argues that, based on its stellar population, NGVS 3543 does not even lie in the Virgo Cluster, but is rather a foreground object. They propose that VCS 9 is actually associated with the galaxy VCC 2034, which is located ~ 70 kpc SW from VCS 9 itself. They support their claim with an integrated HI map using the ALFALFA survey data (see figure 4.7), where they show a bridge between AGC 226178 and VCC 2034. They also note the similarity in metallicity measurements and velocities between AGC 226178 and VCC 2034 (VCC 2034 has a velocity $v = 1507$ kms^{-1}).

[2]After correcting to the equivalent of a 3σ profile.

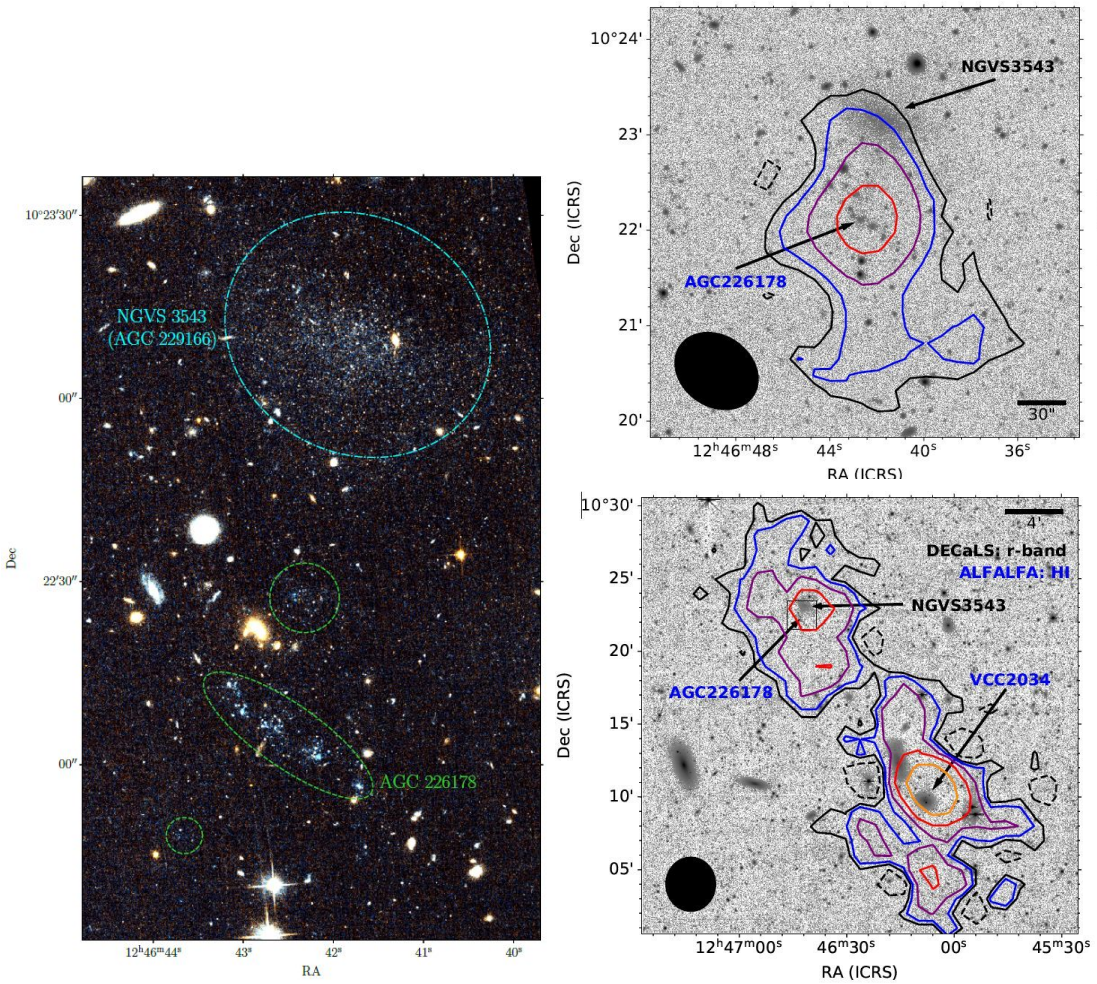

Figure 4.7: Left: False color F606W+F814W image of the AGC 226178 and NGVS 3543 system. Top right: Contours of integrated HI emission (moment 0 map) from the VLA observations of VCS 9 overlaid on a DECaLS g-band image. Bottom right: ALFALFA HI integrated emission contours overlaid on the wide field, including several nearby galaxies that VCS 9 may have interacted with. Figures and caption from Jones et al. (2022).

However, there are still some issues that need to be addressed. Firstly, the distance measurements could be more improved by measurements at different wavelengths, which would put more rigorous constraints on the actual value of the distance. Next, the interpretation of the bridge detected by Jones et al. (2022) in ALFALFA data is still open to question, as I did not detect any such structure with our more than twice as sensitive WAVES data, as seen in figure 4.8. Moreover, VCS 9 and NGVS 3543 lie roughly on a line pointing towards the center of the Virgo Cluster (or perhaps the Cluster C). That would be consistent with the idea of a galaxy falling towards the cluster center, experiencing RPS and leaving the stripped gas behind it. Additionally, VCC 2034 lies in close proximity to VCC 2037, which has velocity $v \approx 1140$ kms^{-1} and with VCS 9 and NGVS 3543 they form a suspiciously perfect line. That could mean they are all associated and hence at the same distance. It seems unlikely, although possible,

that two Virgo Cluster members (VCS 9 and VCC 2037) would line up with two other foreground objects (NGVS 3543 and VCC 2034), especially given how few known foreground Virgo objects there are. And lastly, the difference in velocity of the mentioned objects is not necessarily a direct evidence of either theory, as there are many interacting objects in the Virgo Cluster with velocity differences as high as ~ 1000 kms^{-1}.

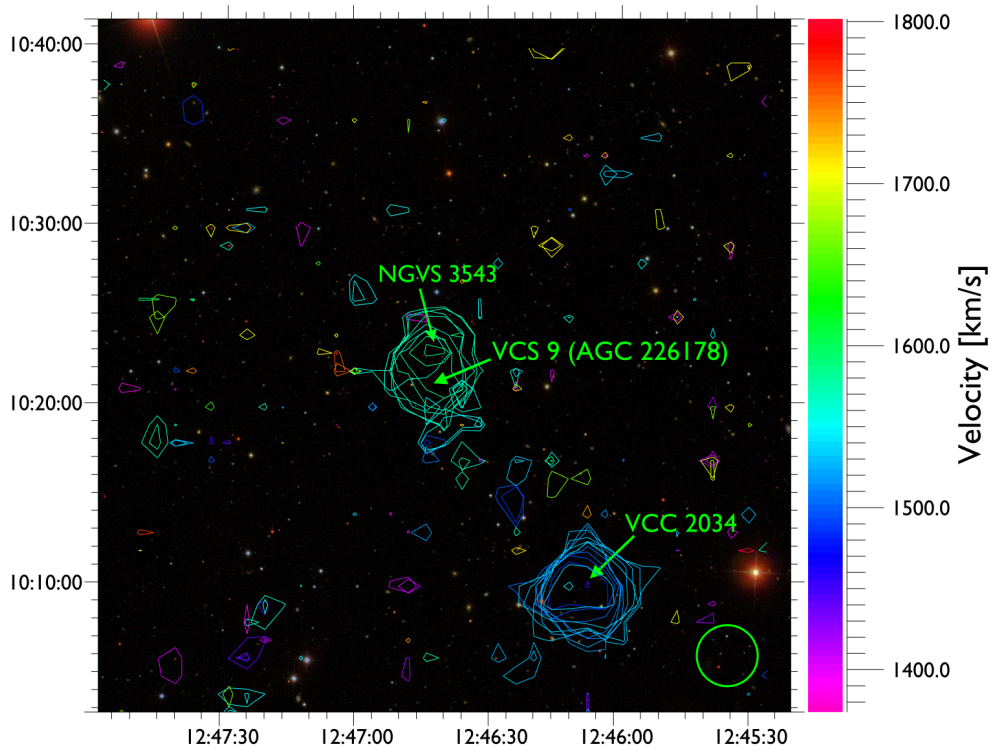

Figure 4.8: Renzogram of VCS 9 and the surrounding regions. The green circle in the corner shows the 3.5 arcmin beam size.

To resolve the issue of VCS 9's origin it is possible to conduct more measurements in other bands, for example by observing the CO emission lines, which should detect and confirm the presence of star-forming regions of VCS 9. Should there be a bridge detected between VCS 9 and NGVS 3543, this would be strong evidence for the association of these two objects. For this purpose we have submitted an ALMA observing proposal, which is pending peer review.

4.3.2 VCS 7 (VCC 2066/2062)

VCS 7 is an HI structure containing the optical galaxies VCC 2066 and VCC 2062. It has been suggested that VCC 2066 has undergone a tidal interaction resulting in stripping gas which formed a tidal dwarf galaxy VCC 2062 (Duc et al., 2007). This is supported by Lelli et al. (2015), who further claimed this must have happened more than 0.5 Gyr ago. The VLA observations in Lelli et al. (2015) clearly show a resolved HI structure connecting VCC 2066 and VCC 2062, and even the WAVES observations are sufficiently resolved to show the presence of the bridge. This is in line with the VLA observations by Lelli et al. (2015), but the WAVES data also show a large potential extension to the south-east,

as seen in figure 4.9. This may indicate some further environmental process at work, which was not detected earlier due to VLA's lower sensitivity and requires further attention.

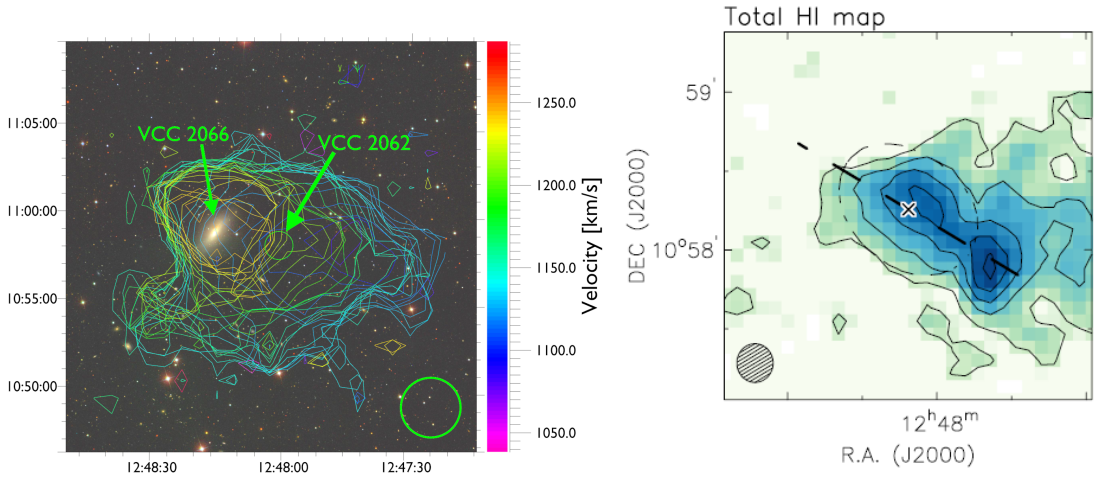

(a) (b)

Figure 4.9: VCC 2066/2062 complex: (a) Renzogram from the WAVES data shows an extension to the lower left. (b) Total HI map from the VLA data by Lelli et al. (2015). Note the difference in spatial scales between the two figures. The green circle in the corner shows the 3.5 arcmin beam size.

4.3.3 VCS 44 (VCCA 52)

Finally, VCS 44 (VCCA 52) is a galaxy with the highest gas fraction in the entire WAVES sample at $M_{HI}/M_\star \approx 27$. This cannot be due to an incorrect distance estimate issue, because the gas fraction calculation is actually independent of distance. Neither are photometric errors a likely culprit, as this was done manually and the galaxy itself is bright enough that measurement errors are unlikely. Also with $g - i \approx 0.18$ it is one of the bluest objects and its HI deficiency of -0.01 is typical of a field galaxy. While an extreme object in terms of its color and gas fraction, it is consistent with the scaling relations: HI deficiency, while correlated to gas fraction is highly scattered and field non-deficient galaxies can have even higher gas fractions (see figure 15 in Taylor et al. (2012) and compare to figure 4.11).

Although VCS 44 has a nice and bright detection in the spectrum, it is located at the very edge of the VSW data cube, with portion of its renzogram cut-off, as visible in figure 4.10. This could have introduced some extra noise, but the possible extent of this is so far unknown. Ultimately, this could be confirmed for example by combining the WAVES and AGES data cubes, since their coverage areas overlap in this region, to get a more definitive measurement.

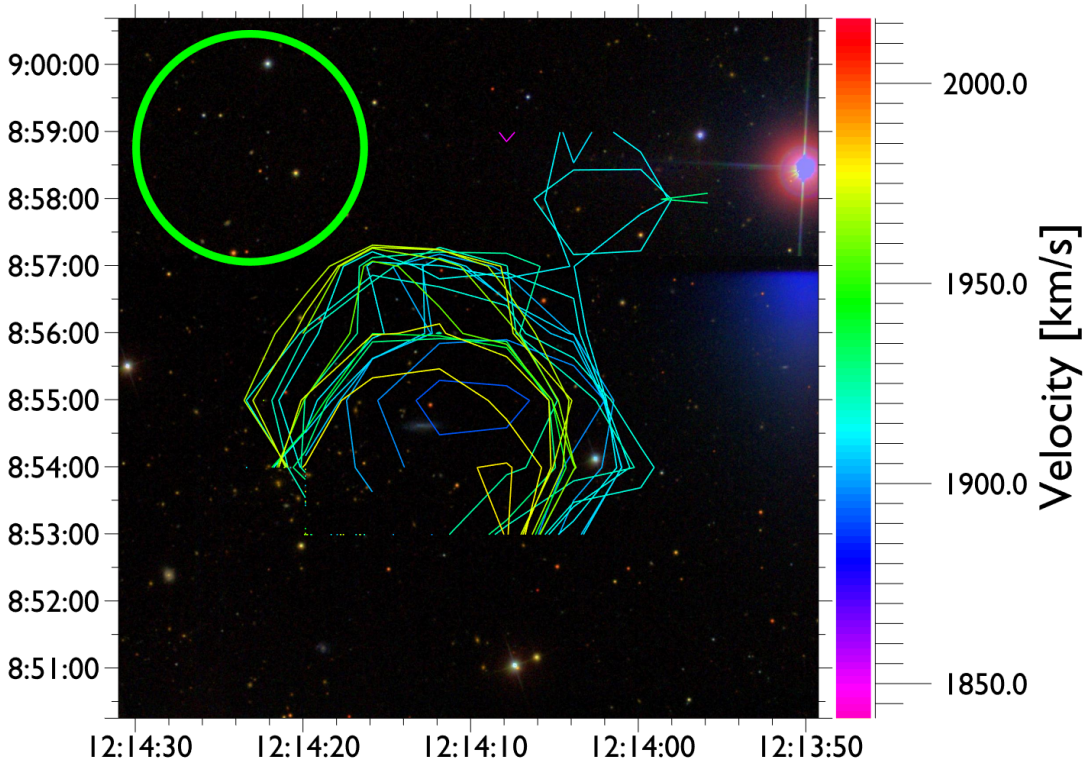

Figure 4.10: VCS 44 renzogram. The green circle in the corner shows the 3.5 arcmin beam size.

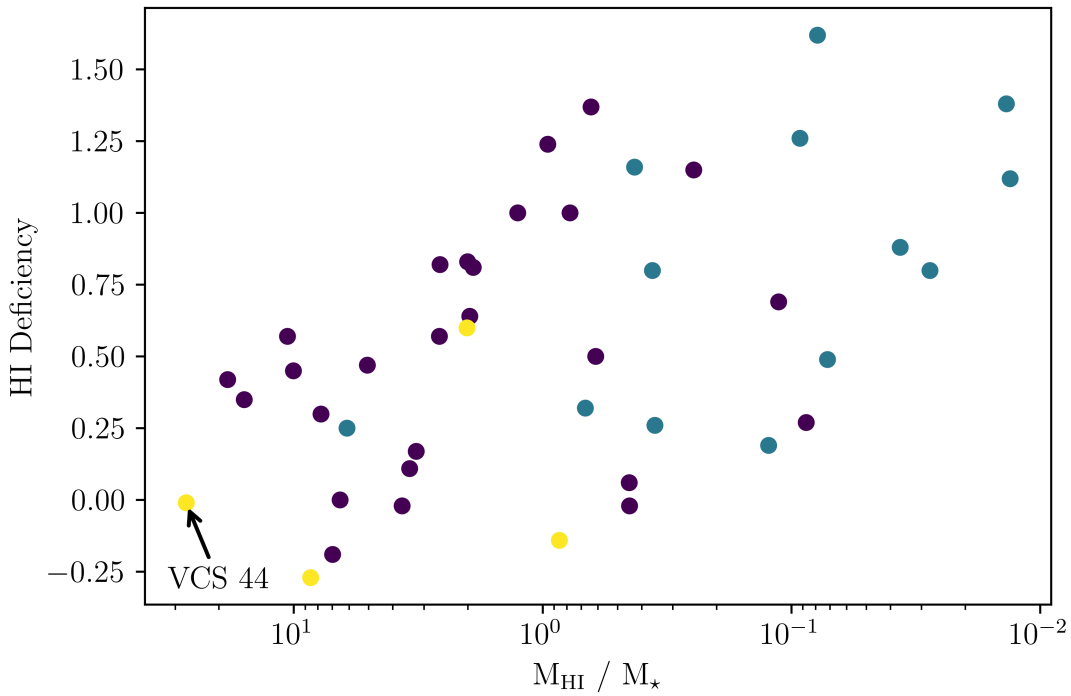

Figure 4.11: Relation of HI deficiency and the $M_{HI}/M_{\star}$ ratio of 43 VCS objects. The horizontal axis is logarithmic. Colors indicate distance: purple = 17 Mpc, blue = 23 Mpc and yellow = 32 Mpc.

5. Conclusions

I analyzed the data from the Wide Arecibo Virgo Extragalactic Survey (WAVES), which observed the 2×10 deg^2 region between M87 and M49 in the Virgo Cluster. In total I recorded 55 VCS objects with an HI detection. Specifically 45 late-type galaxies, 3 early-type galaxies, 3 pairs of galaxies with unresolvable HI emission, one optically dark cloud, one gas cloud with star forming regions and the ALFALFA Virgo 7 complex. I supplemented this with a catalog of HI non-detected objects and filtered it so it only contained objects with good and reliable photometry and velocity measurements, which totalled 86 objects.

I made many comparisons with the VC1 region, which was centered on M49 and adjacent to the WAVES region directly south, to study galaxy evolution in the Virgo Cluster. Based on my data I determine that the WAVES region is likely more relaxed and contains more evolved galaxies than the VC1 region. This is mainly due to the significantly lower fraction of galaxies with HI (16% in WAVES, 29% in VC1) and the velocity distributions, which indicate VC1 contains more objects from infalling clouds which have have not merged with the rest of the cluster. This indicates that this region of the cluster is likely still assembling. I further support this claim with the discrepancy in number of dark clouds, with WAVES containing only one (or at most two) out expected five clouds, based on the detected fraction in the VC1. This suggests they may have had more time to dissipate or collapse. I also examined the effects of ram pressure stripping on the galaxy HI content throughout the cluster, i.e. its efficiency rises with the local density of the ICM the galaxy founds itself in. This is significant because gas loss likely plays an important role in galaxy evolution. The HI deficiency distribution of the WAVES objects further suggests that while WAVES is likely more relaxed, it contains a group of non-deficient galaxies which are probably recent arrivals infalling for the first time. I also showed that HI deficiency is not direct evidence for ongoing gas removal, as most of the objects with HI tails are less deficient compared to the rest of the sample.

Based on the mass-to-light ratio diagram, I found evidence of gas-loss driven evolution of dwarf irregular galaxies being transformed into dwarf elliptical galaxies, in agreement with a theory proposed by Boselli et al. (2008). This was reflected in the relatively low gas fractions found in the early-type galaxies detected in HI, mainly the dEs VCS 11 and VCS 51, but also possibly the dS0 VCS 47. This is in contrast to previous results in VC1 reported by Taylor et al. (2012), where they detected dE galaxies with much higher gas fraction, which would contradict the idea of dI losing gas and transforming into gas-poor dE. But as Taylor et al. (2012) themselves admitted, this might be an issue of dI that were actually misclassified as dE or there is something wrong with the theory. Of course, dE objects in the WAVES region might also suffer from misclassification, but the comparison of color-magnitude diagrams suggests that these two groups are likely indeed different objects. However, further research is needed to determine their true nature.

Lastly, I performed stacking of the HI non-detected galaxies in the WAVES and (partially) in the AGES regions, with many different morphology and distance combinations. It did not result in any new detection, but I was able to achieve

rms noise of 0.129 mJy after stacking 80 objects. This enabled a constraint on HI mass in early-type galaxies in the WAVES region at 1.65×10^6 $M_\odot$, which supports the conclusions of Taylor et al. (2012) that the cluster members without an obvious HI detection likely have little to no gas at all.

Ultimately though, to better understand galaxy evolution, it is necessary to obtain more data and compare cluster members with field galaxies, preferably by further analyzing the WAVES North region and including the background objects behind the Virgo Cluster. As the WAVES data cubes extends to $v = 20\,000$ kms^{-1} and in this work I only cataloged the Virgo Cluster members, with velocity < 3000 kms^{-1}, there is still much more data to analyze. More improvements may also be made with better distance estimates, which are currently inconsistent at best, although this is a ongoing problem in extragalactic astronomy.

In summary, I cataloged 55 objects VCS with HI detection, which I analyzed and concluded that WAVES region is more relaxed than VC1, likely with more evolved galaxies, and I also found evidence for gas-loss driven evolution of dwarf irregular galaxies into dwarf ellipticals.

Bibliography

Kevork N Abazajian, Jennifer K Adelman-McCarthy, Marcel A Agüeros, Sahar S Allam, Carlos Allende Prieto, Deokkeun An, Kurt SJ Anderson, Scott F Anderson, James Annis, Neta A Bahcall, et al. The seventh data release of the sloan digital sky survey. *The Astrophysical Journal Supplement Series*, 182(2): 543, 2009.

Robbie Auld, Robert F Minchin, Jonathan Ivor Davies, Barbara Catinella, Willem Van Driel, Patricia A Henning, Suzanne Linder, Emmanuel Momjian, Erik Muller, Karen O'Neil, et al. The arecibo galaxy environment survey: precursor observations of the ngc 628 group. *Monthly Notices of the Royal Astronomical Society*, 371(4):1617–1640, 2006.

Cecilia Bacchini, Filippo Fraternali, Giuliano Iorio, and Gabriele Pezzulli. Volumetric star formation laws of disc galaxies. *Astronomy & Astrophysics*, 622: A64, 2019.

David G Barnes, Lister Staveley-Smith, WJG e 3 al de Blok, T Oosterloo, Ian M Stewart, AE Wright, GD Banks, R Bhathal, PJ Boyce, MR Calabretta, et al. The h i parkes all sky survey: southern observations, calibration and robust imaging. *Monthly Notices of the Royal Astronomical Society*, 322(3):486–498, 2001.

Joshua E Barnes. Encounters of disk/halo galaxies. *Astrophysical Journal, Part 1 (ISSN 0004-637X), vol. 331, Aug. 15, 1988, p. 699-717.*, 331:699–717, 1988.

Eric F Bell, Christian Wolf, Klaus Meisenheimer, Hans-Walter Rix, Andrea Borch, Simon Dye, Martina Kleinheinrich, Lutz Wisotzki, and Daniel H McIntosh. Nearly 5000 distant early-type galaxies in combo-17: a red sequence and its evolution since z˜ 1. *The Astrophysical Journal*, 608(2):752, 2004.

B Binggeli, CC Popescu, and GA Tammann. The kinematics of the virgo cluster revisited. *Astronomy and Astrophysics Supplement Series (ISSN 0365-0138), vol. 98, no. 2, p. 275-296.*, 98:275–296, 1993.

Bruno Binggeli, A Sandage, and GA Tammann. Studies of the virgo cluster. ii-a catalog of 2096 galaxies in the virgo cluster area. *Astronomical Journal (ISSN 0004-6256), vol. 90, Sept. 1985, p. 1681-1759. SNSF-supported research.*, 90: 1681–1759, 1985.

Bruno Binggeli, GA Tammann, and Allan Sandage. Studies of the virgo cluster. vi-morphological and kinematical structure of the virgo cluster. *Astronomical Journal (ISSN 0004-6256), vol. 94, Aug. 1987, p. 251-277. SNSF-supported research.*, 94:251–277, 1987.

James Binney and Scott Tremaine. *Galactic dynamics*, volume 20. Princeton university press, 2011.

Hans Böhringer, UG Briel, RA Schwarz, W Voges, G Hartner, and J Trümper. The structure of the virgo cluster of galaxies from rosat x-ray images. *Nature*, 368(6474):828–831, 1994.

A Boselli and G Gavazzi. The hi properties of galaxies in the coma i cloud revisited. *Astronomy & Astrophysics*, 508(1):201–207, 2009.

A Boselli, Samuel Boissier, Luca Cortese, and G Gavazzi. The origin of dwarf ellipticals in the virgo cluster. *The Astrophysical Journal*, 674(2):742, 2008.

A Boselli, E Voyer, Samuel Boissier, O Cucciati, G Consolandi, Luca Cortese, M Fumagalli, G Gavazzi, S Heinis, Y Roehlly, et al. The galex ultraviolet virgo cluster survey (guvics)-iv. the role of the cluster environment on galaxy evolution. *Astronomy & Astrophysics*, 570:A69, 2014.

Encyclopedia Britannica. Brittanica arecibo observatory. `https://www.britannica.com/topic/Arecibo-Observatory`, 2024. Accessed: 19.3.2024.

Aeree Chung, JH Van Gorkom, Jeffrey DP Kenney, and Bernd Vollmer. Virgo galaxies with long one-sided hi tails. *The Astrophysical Journal*, 659(2):L115, 2007.

Christopher J Conselice. Early and rapid merging as a formation mechanism of massive galaxies: empirical constraints. *The Astrophysical Journal*, 638(2):686, 2006.

DO Cook, JM Mazzarella, G Helou, A Alcala, TX Chen, R Ebert, C Frayer, J Kim, T Lo, BF Madore, et al. Completeness of the nasa/ipac extragalactic database (ned) local volume sample. *The Astrophysical Journal Supplement Series*, 268(1):14, 2023.

Edvige Corbelli and Paolo Salucci. The extended rotation curve and the dark matter halo of m33. *Monthly Notices of the Royal Astronomical Society*, 311 (2):441–447, 2000.

L Cortese and TM Hughes. Evolutionary paths to and from the red sequence: star formation and h i properties of transition galaxies at z 0. *Monthly Notices of the Royal Astronomical Society*, 400(3):1225–1240, 2009.

Luca Cortese, Robert Frank Minchin, Robbie Richard Auld, Jonathan Ivor Davies, Barbara Catinella, Emmanuel Momjian, Jessica L Rosenberg, Rhys Taylor, Giuseppe Gavazzi, K O'Neil, et al. The arecibo galaxy environment survey–ii. ah i view of the abell cluster 1367 and its outskirts. *Monthly Notices of the Royal Astronomical Society*, 383(4):1519–1537, 2008.

Boris Deshev, Rhys Taylor, Robert Minchin, Tom C Scott, and Elias Brinks. The arecibo galaxy environment survey (ages)-xi. the expanded abell 1367 field: Data catalogue and h i census over the surveyed volume. *Astronomy & Astrophysics*, 665:A155, 2022.

John M Dickey and Felix J Lockman. Hi in the galaxy. *Annual review of astronomy and astrophysics*, 28(1):215–259, 1990.

Alan Dressler. Galaxy morphology in rich clusters-implications for the formation and evolution of galaxies. *Astrophysical Journal, Part 1, vol. 236, Mar. 1, 1980, p. 351-365.*, 236:351–365, 1980.

Alan Dressler. Star-forming galaxies in clusters. *Clusters of Galaxies: Probes of Cosmological Structure*, 3:206–226, 2004.

John Louis Emil Dreyer. A new general catalogue of nebulæ and clusters of stars, being the catalogue of the late sir john fw herschel, bart, revised, corrected, and enlarged. *Memoirs of the Royal Astronomical Society, Vol. 49, p. 1*, 49:1, 1888.

John Louis Emil Dreyer. Index catalogue of nebulæ found in the years 1888 to 1894, with notes and corrections to the new general catalogue. *Memoirs of the Royal Astronomical Society, Vol. 51, p. 185*, 51:185, 1895.

P-A Duc, Jonathan Braine, Ute Lisenfeld, Elias Brinks, and Médéric Boquien. Vcc 2062: an old tidal dwarf galaxy in the virgo cluster? *Astronomy & Astrophysics*, 475(1):187–197, 2007.

L Dunne, Haley Louise Gomez, Elisabete da Cunha, S Charlot, Simon Dye, S Eales, Steve J Maddox, K Rowlands, DJB Smith, R Auld, et al. Herschel-atlas: rapid evolution of dust in galaxies over the last 5 billion years. *Monthly Notices of the Royal Astronomical Society*, 417(2):1510–1533, 2011.

Stephen Eales, Pieter de Vis, Matthew WL Smith, Kiran Appah, Laure Ciesla, Chris Duffield, and Simon Schofield. The galaxy end sequence. *Monthly Notices of the Royal Astronomical Society*, 465(3):3125–3133, 2016.

Harold Irving Ewen and Edward Mills Purcell. Observation of a line in the galactic radio spectrum: Radiation from galactic hydrogen at 1,420 mc./sec. *Nature*, 168(4270):356–356, 1951.

Silvia Fabello, Barbara Catinella, Riccardo Giovanelli, Guinevere Kauffmann, Martha P Haynes, Timothy M Heckman, and David Schiminovich. Alfalfa h i data stacking–i. does the bulge quench ongoing star formation in early-type galaxies? *Monthly Notices of the Royal Astronomical Society*, 411(2):993–1012, 2011.

George B Field. Excitation of the hydrogen 21-cm line. *Proceedings of the IRE*, 46(1):240–250, 1958.

Pascal Fouqué, José M Solanes, Teresa Sanchis, and Chantal Balkowski. Structure, mass and distance of the virgo cluster from a tolman-bondi model. *Astronomy & Astrophysics*, 375(3):770–780, 2001.

Wolfram Freudling, Lister Staveley-Smith, Barbara Catinella, Robert Minchin, Mark Calabretta, Emmanuel Momjian, Martin Zwaan, Martin Meyer, and Karen O'Neil. Deep 21 cm h i observations at z $\approx$ 0.1: The precursor to the arecibo ultra deep survey. *The Astrophysical Journal*, 727(1):40, 2010.

G Gavazzi, A Boselli, M Scodeggio, D Pierini, and E Belsole. The 3d structure of the virgo cluster from h-band fundamental plane and tully—fisher distance determinations. *Monthly Notices of the Royal Astronomical Society*, 304(3): 595–610, 1999.

Giuseppe Gavazzi, Alessandro Boselli, Alessandro Donati, Paolo Franzetti, and Marco Scodeggio. Introducing goldmine: A new galaxy database on the web. *Astronomy & Astrophysics*, 400(2):451–455, 2003.

Giuseppe Gavazzi, Alessandro Boselli, Willem van Driel, and K O'neil. Completing h i observations of galaxies in the virgo cluster. *Astronomy & Astrophysics*, 429(2):439–447, 2005.

Giuseppe Gavazzi, Mattia Fumagalli, Olga Cucciati, and Alessandro Boselli. A snapshot on galaxy evolution occurring in the great wall: the role of nurture at z= 0. *Astronomy & Astrophysics*, 517:A73, 2010.

Riccardo Giovanelli and Martha P Haynes. Gas deficiency in cluster galaxies-a comparison of nine clusters. *Astrophysical Journal, Part 1 (ISSN 0004-637X), vol. 292, May 15, 1985, p. 404-425.*, 292:404–425, 1985.

Riccardo Giovanelli, Martha P Haynes, Brian R Kent, Philip Perillat, Amelie Saintonge, Noah Brosch, Barbara Catinella, G Lyle Hoffman, Sabrina Stierwalt, Kristine Spekkens, et al. The arecibo legacy fast alfa survey. i. science goals, survey design, and strategy. *The astronomical journal*, 130(6):2598, 2005.

Nickolay Y Gnedin, Simon CO Glover, Ralf S Klessen, Volker Springel, Ralf S Klessen, and Simon CO Glover. Physical processes in the interstellar medium. *Star Formation in Galaxy Evolution: Connecting Numerical Models to Reality: Saas-Fee Advanced Course 43. Swiss Society for Astrophysics and Astronomy*, pages 85–249, 2016.

GOLDMine. Galaxy on line database milano network. `http://goldmine.inaf.it/`, 2002. Accessed: 19.3.2024.

Richard Gooch. Karma: a visualization test-bed. In *Astronomical Data Analysis Software and Systems V, ASP Conference Series, Vol. 101, 1996, George H. Jacoby and Jeannette Barnes, eds., p. 80.*, volume 101, page 80, 1996.

James E Gunn and J Richard Gott III. On the infall of matter into clusters of galaxies and some effects on their evolution. *Astrophysical Journal, vol. 176, p. 1*, 176:1, 1972.

Yasuhiro Hashimoto, Augustus Oemler Jr, Huan Lin, and Douglas L Tucker. The influence of environment on the star formation rates of galaxies. *The Astrophysical Journal*, 499(2):589, 1998.

Martha P Haynes and Riccardo Giovanelli. Neutral hydrogen in isolated galaxies. iv-results for the arecibo sample. *Astronomical Journal (ISSN 0004-6256), vol. 89, June 1984, p. 758-800.*, 89:758–800, 1984.

Helmut Hellwig, Robert FC Vessot, Martin W Levine, Paul W Zitzewitz, David W Allan, and David J Glaze. Measurement of the unperturbed hydrogen hyperfine transition frequency. *IEEE Transactions on Instrumentation and Measurement*, 19(4):200–209, 1970.

George Helou, BF Madore, M Schmitz, MD Bicay, X Wu, and J Bennett. The nasa/ipac extragalactic database. *Databases & On-Line Data in Astronomy*, pages 89–106, 1991.

E. Hubble. *The Realm of the Nebulæ*. Memorial lectures. Yale University Press, 1936. URL `https://books.google.cz/books?id=Kl9CrudjMqcC`.

Edwin Hubble. No. 324. extra-galactic nebulae. *Contributions from the Mount Wilson Observatory/Carnegie Institution of Washington*, 324:1–49, 1926.

Michael G Jones, David J Sand, Michele Bellazzini, Kristine Spekkens, John M Cannon, Burçin Mutlu-Pakdil, Ananthan Karunakaran, Giacomo Beccari, Laura Magrini, Giovanni Cresci, et al. Agc 226178 and ngvs 3543: Two deceptive dwarfs toward virgo. *The Astrophysical Journal Letters*, 926(2):L15, 2022.

Michael G Jones, Steven Janowiecki, Swapnaneel Dey, David J Sand, Paul Bennet, Denija Crnojevic, Catherine E Fielder, Ananthan Karunakaran, Brian R Kent, Nicolas Mazziotti, et al. Dark no more: The low luminosity stellar counterpart of a dark cloud in the virgo cluster. *arXiv preprint arXiv:2402.14909*, 2024.

Zhao Jun-liang, Pan Rong-shi, Huang Song-nan, and He Yan-ping. The radial velocity membership of the virgo cluster. *Chinese astronomy and astrophysics*, 15(1):95–102, 1991.

S Junais, Boissier, A Boselli, M Boquien, A Longobardi, Y Roehlly, P Amram, M Fossati, J-C Cuillandre, S Gwyn, L Ferrarese, et al. A virgo environmental survey tracing ionised gas emission (vestige)-x. formation of a red ultra-diffuse galaxy and an almost dark galaxy during a ram-pressure stripping event. *Astronomy & Astrophysics*, 650:A99, 2021.

Hiroyuki Kaneko, Nario Kuno, Daisuke Iono, Tomaka Tosaki, Takeshi Sawada, Hiroyuki Nakanishi, and Akihiko Hirota. Molecular gas in the early stage of interacting galaxies: The ngc 4567/8 pair. In *Galaxy Wars: Stellar Populations and Star Formation in Interacting Galaxies*, volume 423, page 26, 2010.

Igor D Karachentsev, Lidia N Makarova, R Brent Tully, Luca Rizzi, and Edward J Shaya. Trgb distances to galaxies in front of the virgo cluster. *The Astrophysical Journal*, 858(1):62, 2018.

Olga G Kashibadze, Igor D Karachentsev, and Valentina E Karachentseva. Structure and kinematics of the virgo cluster of galaxies. *Astronomy & Astrophysics*, 635:A135, 2020.

Jeffrey DP Kenney, Marla Geha, Pavel Jáchym, Hugh H Crowl, William Dague, Aeree Chung, Jacqueline Van Gorkom, and Bernd Vollmer. Transformation of a virgo cluster dwarf irregular galaxy by ram pressure stripping: Ic3418 and its fireballs. *The Astrophysical Journal*, 780(2):119, 2013.

Brian R Kent, Riccardo Giovanelli, Martha P Haynes, Amélie Saintonge, Sabrina Stierwalt, Thomas Balonek, Noah Brosch, Barbara Catinella, Rebecca A Koopmann, Emmanuel Momjian, et al. Optically unseen hi detections toward the virgo cluster detected in the arecibo legacy fast alfa survey. *The Astrophysical Journal*, 665(1):L15, 2007.

Brian R Kent, Kristine Spekkens, Riccardo Giovanelli, Martha P Haynes, Emmanuel Momjian, Juan R Cortés, Eduardo Hardy, and Andrew A West. The arecibo legacy fast alfa survey. vii. a neutral hydrogen cloud complex in the virgo cluster. *The Astrophysical Journal*, 691(2):1595, 2009.

J Köppen, P Jáchym, R Taylor, and J Palouš. Ram pressure stripping made easy: an analytical approach. *Monthly Notices of the Royal Astronomical Society*, 479 (4):4367–4390, 2018.

Federico Lelli, Pierre-Alain Duc, Elias Brinks, Frédéric Bournaud, Stacy S McGaugh, Ute Lisenfeld, Peter M Weilbacher, Médéric Boquien, Yves Revaz, Jonathan Braine, et al. Gas dynamics in tidal dwarf galaxies: disc formation at z= 0. *Astronomy & Astrophysics*, 584:A113, 2015.

Adam K Leroy, Fabian Walter, Elias Brinks, Frank Bigiel, WJG De Blok, Barry Madore, and MD Thornley. The star formation efficiency in nearby galaxies: measuring where gas forms stars effectively. *The astronomical journal*, 136(6): 2782, 2008.

Paulo AA Lopes, André LB Ribeiro, and Douglas Brambila. The role of groups in galaxy evolution: compelling evidence of pre-processing out to the turnaround radius of clusters. *Monthly Notices of the Royal Astronomical Society: Letters*, 527(1):L19–L25, 2024.

Jennifer M Lotz, Patrik Jonsson, TJ Cox, and Joel R Primack. Galaxy merger morphologies and time-scales from simulations of equal-mass gas-rich disc mergers. *Monthly Notices of the Royal Astronomical Society*, 391(3):1137–1162, 2008.

Naomi M McClure-Griffiths, Snežana Stanimirović, and Daniel R Rybarczyk. Atomic hydrogen in the milky way: A stepping stone in the evolution of galaxies. *Annual Review of Astronomy and Astrophysics*, 61, 2023.

Martin J Meyer, Martin A Zwaan, Rachel L Webster, Lister Staveley-Smith, E Ryan-Weber, Michael John Drinkwater, David G Barnes, Matt Howlett, Virginia A Kilborn, J Stevens, et al. The hipass catalogue–i. data presentation. *Monthly Notices of the Royal Astronomical Society*, 350(4):1195–1209, 2004.

Robert Minchin and Rhys Taylor. Vla observations of optically-dark neutral hydrogen clouds in the virgo cluster. In *American Astronomical Society Meeting Abstracts*, volume 55, pages 460–01, 2023.

Robert F Minchin, Rhys Taylor, Joachim Köppen, Jonathan I Davies, Wim Van Driel, and Olivia Keenan. The widefield arecibo virgo extragalactic survey. i. new structures in the alfalfa virgo 7 cloud complex and an extended tail on ngc 4522. *The Astronomical Journal*, 158(3):121, 2019.

Ben Moore, Neal Katz, George Lake, Alan Dressler, and Augustus Oemler. Galaxy harassment and the evolution of clusters of galaxies. *nature*, 379(6566): 613–616, 1996.

NASA/IPAC. NED database holdings for release 34.1.1. `https://ned.ipac.caltech.edu/CurrentHoldings`, 2024. Accessed: 16.3.2024.

P. Nilson. Uppsala General Catalogue of Galaxies, 1973, Acta Universitatis Upsalienis, Nova Regiae Societatis Upsaliensis, Series v: a Vol. *Nova Acta Regiae Soc. Sci. Upsaliensis Ser. V*, page 0, January 1973.

NSF. National Science Foundation arecibo: Facts and figures. `https://www.nsf.gov/news/special_reports/arecibo/Arecibo_Fact_Sheet_11_20.pdf`, 2021. Accessed: 19.3.2024.

Tom Oosterloo and Jacqueline van Gorkom. A large h i cloud near the centre of the virgo cluster. *Astronomy & Astrophysics*, 437(1):L19–L22, 2005.

Morton S Roberts. The neutral hydrogen content of late-type spiral galaxies. *Astronomical Journal, Vol. 67, p. 437-446 (1962)*, 67:437–446, 1962.

Vera C Rubin and W Kent Ford Jr. Rotation of the andromeda nebula from a spectroscopic survey of emission regions. *Astrophysical Journal, vol. 159, p. 379*, 159:379, 1970.

Amélie Saintonge. The arecibo legacy fast alfa survey. iv. strategies for signal identification and survey catalog reliability. *The Astronomical Journal*, 133(5): 2087, 2007.

Robert J Sault, Peter J Teuben, and Mel CH Wright. A retrospective view of miriad. In *Astronomical Data Analysis Software and Systems IV*, volume 77, page 433, 1995.

S Schindler, B Binggeli, and H Böhringer. Morphology of the virgo cluster: Gas versus galaxies. *arXiv preprint astro-ph/9811464*, 1998.

Edward F Schlafly and Douglas P Finkbeiner. Measuring reddening with sloan digital sky survey stellar spectra and recalibrating sfd. *The Astrophysical Journal*, 737(2):103, 2011.

David J Schlegel, Douglas P Finkbeiner, and Marc Davis. Maps of dust infrared emission for use in estimation of reddening and cosmic microwave background radiation foregrounds. *The Astrophysical Journal*, 500(2):525, 1998.

Paolo Serra, Tobias Westmeier, Nadine Giese, Russell Jurek, Lars Flöer, Attila Popping, Benjamin Winkel, Thijs Van der Hulst, Martin Meyer, Bärbel S Koribalski, et al. Sofia: a flexible source finder for 3d spectral line data. *Monthly Notices of the Royal Astronomical Society*, 448(2):1922–1929, 2015.

Kazuhiro Shimasaku, Masataka Fukugita, Mamoru Doi, Masaru Hamabe, Takashi Ichikawa, Sadanori Okamura, Maki Sekiguchi, Naoki Yasuda, Jon Brinkmann, Istvan Csabai, et al. Statistical properties of bright galaxies in the sloan digital sky survey photometric system. *The Astronomical Journal*, 122(3):1238, 2001.

Jose M Solanes, Riccardo Giovanelli, and Martha P Haynes. The hi content of spirals. i. field-galaxy hi mass functions and hi mass-optical size regression. *arXiv preprint astro-ph/9511003*, 1995.

L.S. Sparke and J.S. Gallagher. *Galaxies in the Universe: An Introduction*. Cambridge University Press, 2007. ISBN 9781139462389. URL `https://books.google.cz/books?id=N8Hngab5liQC`.

Edward N Taylor, Andrew M Hopkins, Ivan K Baldry, Michael JI Brown, Simon P Driver, Lee S Kelvin, David T Hill, Aaron SG Robotham, Joss Bland-Hawthorn, DH Jones, et al. Galaxy and mass assembly (gama): stellar mass estimates. *Monthly Notices of the Royal Astronomical Society*, 418(3):1587–1620, 2011.

R Taylor, RF Minchin, H Herbst, Jonathan Ivor Davies, R Rodriguez, and C Vazquez. The arecibo galaxy environment survey–vii. a dense filament with extremely long h i streams. *Monthly Notices of the Royal Astronomical Society*, 443(3):2634–2649, 2014.

R Taylor, JI Davies, P Jáchym, O Keenan, RF Minchin, J Palouš, R Smith, and R Wünsch. Attack of the flying snakes: formation of isolated h i clouds by fragmentation of long streams. *Monthly Notices of the Royal Astronomical Society*, 461(3):3001–3026, 2016.

Rh Taylor, Jonathan Ivor Davies, R Auld, and Robert Frank Minchin. The arecibo galaxy environment survey–v. the virgo cluster (i). *Monthly Notices of the Royal Astronomical Society*, 423(1):787–810, 2012.

Rh Taylor, JI Davies, R Auld, RF Minchin, and R Smith. The arecibo galaxy environment survey–vi. the virgo cluster (ii). *Monthly Notices of the Royal Astronomical Society*, 428(1):459–469, 2013.

Rhys Taylor. *Virgo Cluster through the AGES*. Cardiff University (United Kingdom), 2010.

Rhys Taylor. Frelled: A realtime volumetric data viewer for astronomers. *Astronomy and Computing*, 13:67–79, 2015.

Rhys Taylor, Joachim Köppen, Pavel Jáchym, Robert Minchin, Jan Palouš, and Richard Wünsch. Faint and fading tails: The fate of stripped h i gas in virgo cluster galaxies. *The Astronomical Journal*, 159(5):218, 2020.

Rhys Taylor, Joachim Köppen, Pavel Jachym, Robert Minchin, Jan Palouš, Jessica L Rosenberg, Stephen Schneider, Richard Wünsch, and Boris Deshev. The arecibo galaxy environment survey. xii. optically dark h i clouds in the leo i group. *The Astronomical Journal*, 164(6):233, 2022.

A Richard Thompson, BG Clark, CM Wade, and Peter J Napier. The very large array. *Astrophysical Journal Supplement Series, vol. 44, Oct. 1980, p. 151-167.*, 44:151–167, 1980.

Alar Toomre and Juri Toomre. Galactic bridges and tails. *Astrophysical Journal, Vol. 178, pp. 623-666 (1972)*, 178:623–666, 1972.

Matthew T Whiting. duchamp: a 3d source finder for spectral-line data. *Monthly Notices of the Royal Astronomical Society*, 421(4):3242–3256, 2012.

Christopher NA Willmer. The absolute magnitude of the sun in several filters. *The Astrophysical Journal Supplement Series*, 236(2):47, 2018.

Mark G Wolfire, Christopher F McKee, David Hollenbach, and AGGM Tielens. Neutral atomic phases of the interstellar medium in the galaxy. *The Astrophysical Journal*, 587(1):278, 2003.

Oiwei Ivy Wong, Emma V Ryan-Weber, Diego A Garcia-Appadoo, Rachel L Webster, Lister Staveley-Smith, Martin A Zwaan, Michael J Meyer, David G Barnes, Virginia A Kilborn, Ragbir Bhathal, et al. The northern hipass catalogue–data presentation, completeness and reliability measures. *Monthly Notices of the Royal Astronomical Society*, 371(4):1855–1864, 2006.

Donald G York, J Adelman, John E Anderson Jr, Scott F Anderson, James Annis, Neta A Bahcall, JA Bakken, Robert Barkhouser, Steven Bastian, Eileen Berman, et al. The sloan digital sky survey: Technical summary. *The Astronomical Journal*, 120(3):1579, 2000.

Fritz Zwicky, E. Herzog, and P. Wild. *Catalogue of galaxies and of clusters of galaxies*. California Institute Of Technology, 1968.

List of Figures

List of Tables

List of Abbreviations

HI - Neutral Hydrogen

HII - Ionized Hydrogen

H_2 - Molecular Hydrogen

ETG - Early-type galaxy

LTG - Late-type galaxy

AUDS - Arecibo Ultra Deep Survey

WAVES - Widefield Arecibo Virgo Extragalactic Survey

AGES - Arecibo Galaxy Environment Survey

ALFALFA - Arecibo Legacy Fast ALFA

ALFA - Arecibo L-band Feed Array

HIPASS - HI Parkes All Sky Survey

VCS - Virgo Cluster South

SF - Star Formation

ICM - Intracluster Medium

RPS - Ram Pressure Stripping

dE - Dwarf Elliptical (galaxy)

dS0 - Dwarf Spheroidal (galaxy)

VCC - Virgo Cluster Catalog

rms - Root Mean Square

RFI - Radio Frequency Interference

S/N - Signal-to-Noise

GOLDMine - Galaxy On Line Database Milano Network

SDSS - Sloan Digital Sky Survey

NED - NASA/IPAC Extragalactic Database

FRELLED - FITS Realtime Explorer of Low Latency in Every Dimension

A. Attachments

A.1 Spectra of the VCS objects

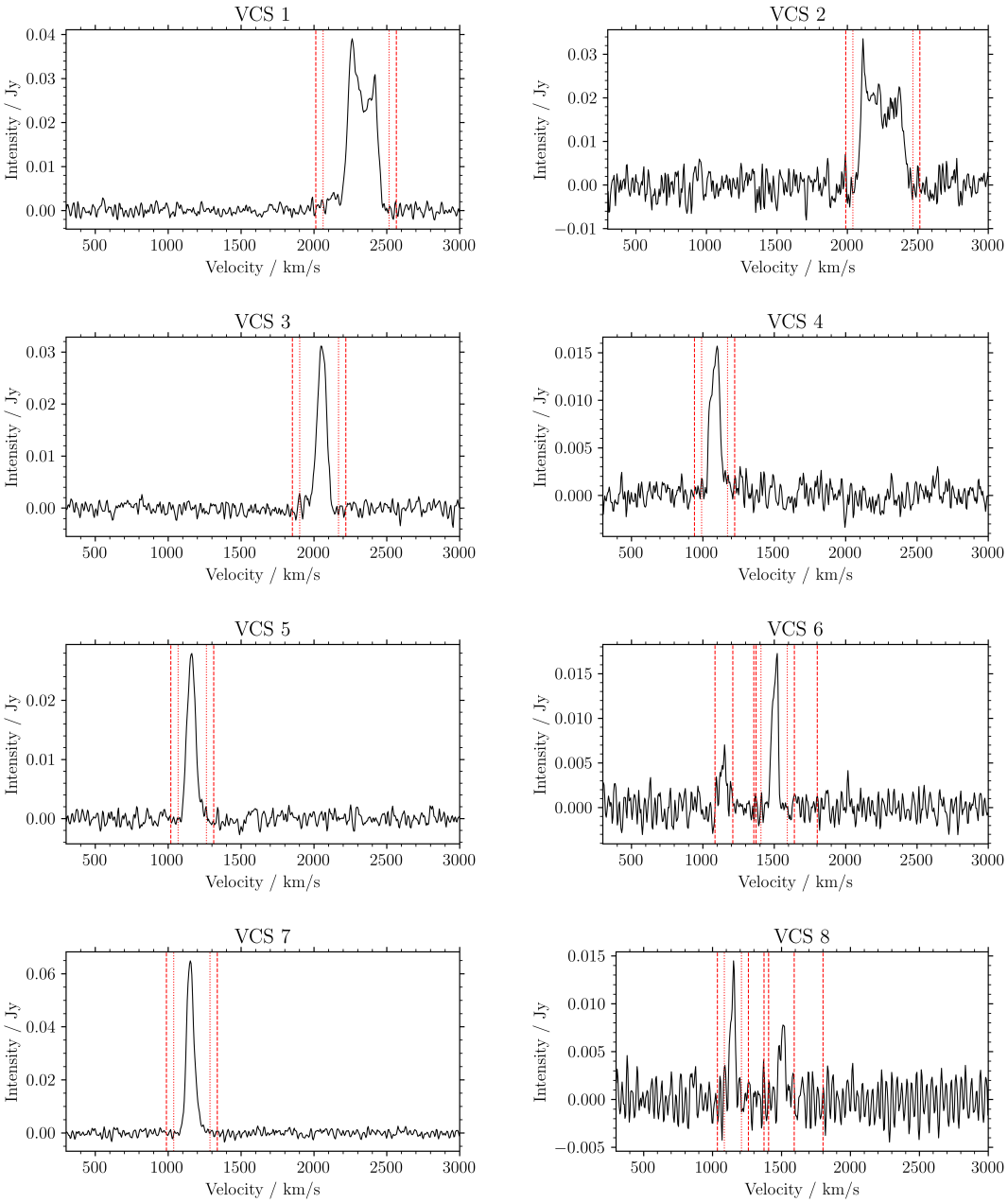

Figure A.1: Measured spectra of VCS 1 – 8. The dotted line shows profile of the line and the dashed line shows the mask.

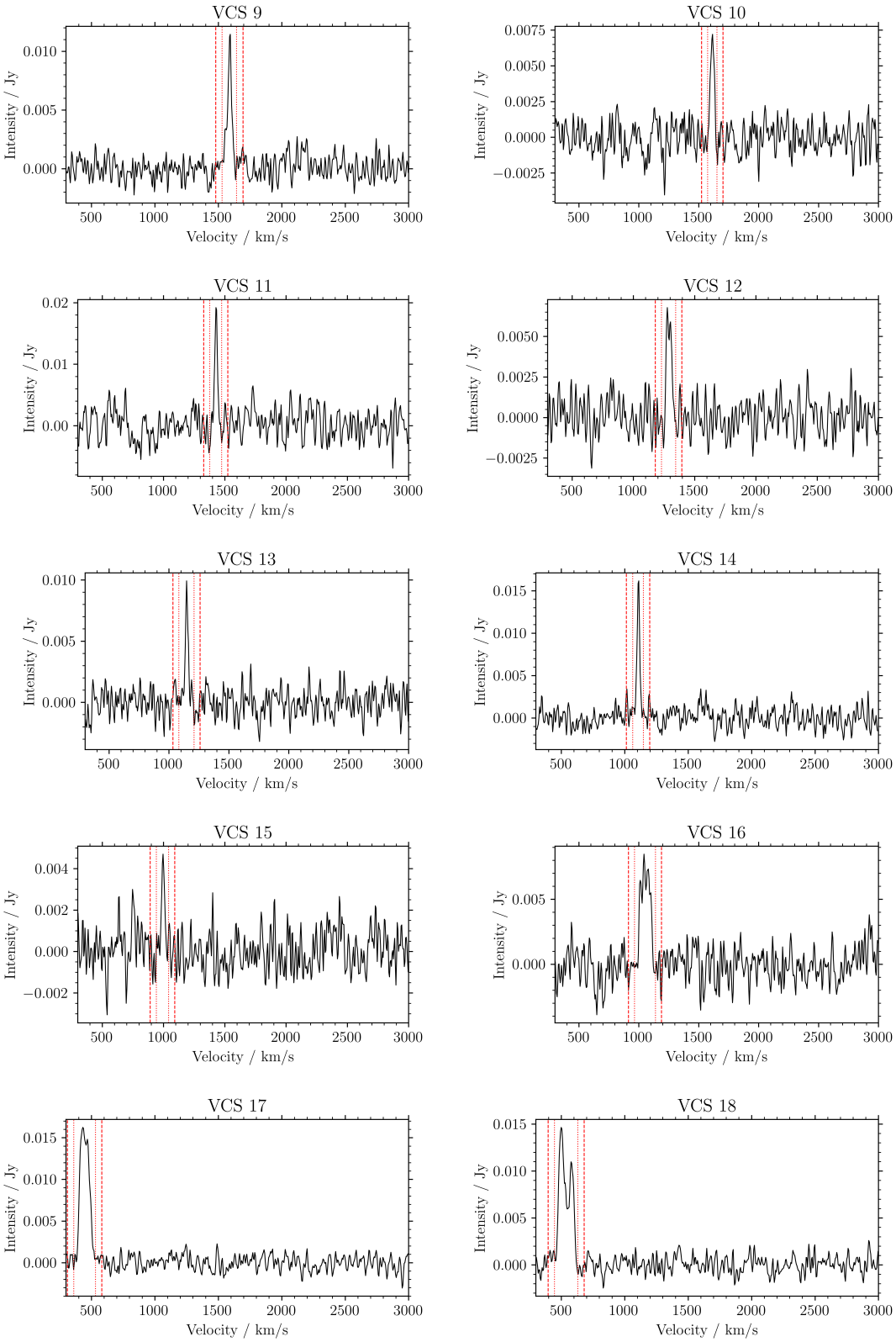

Figure A.2: Measured spectra of VCS 9 – 18. The dotted line shows profile of the line and the dashed line shows the mask.

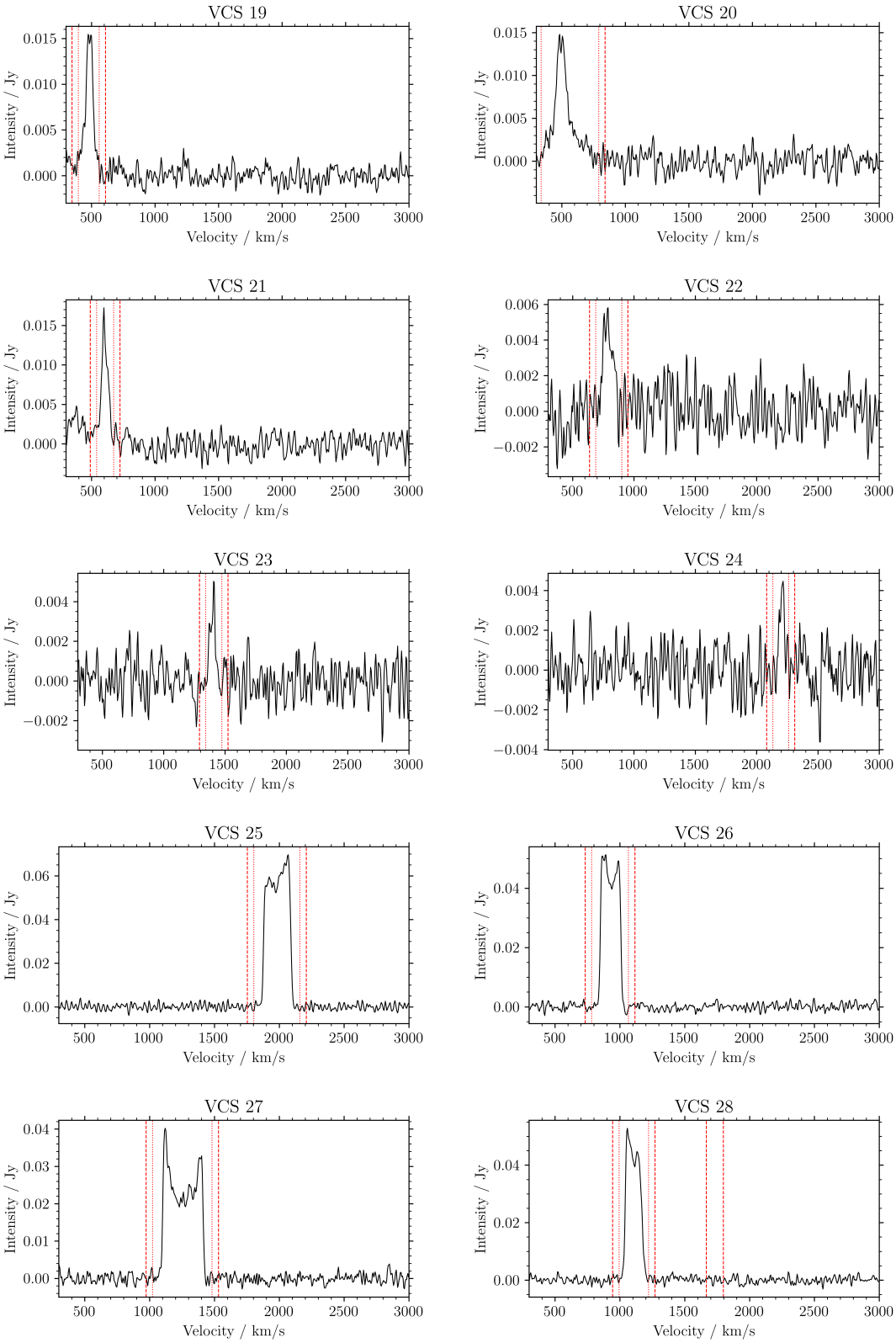

Figure A.3: Measured spectra of VCS 19 – 28. The dotted line shows profile of the line and the dashed line shows the mask.

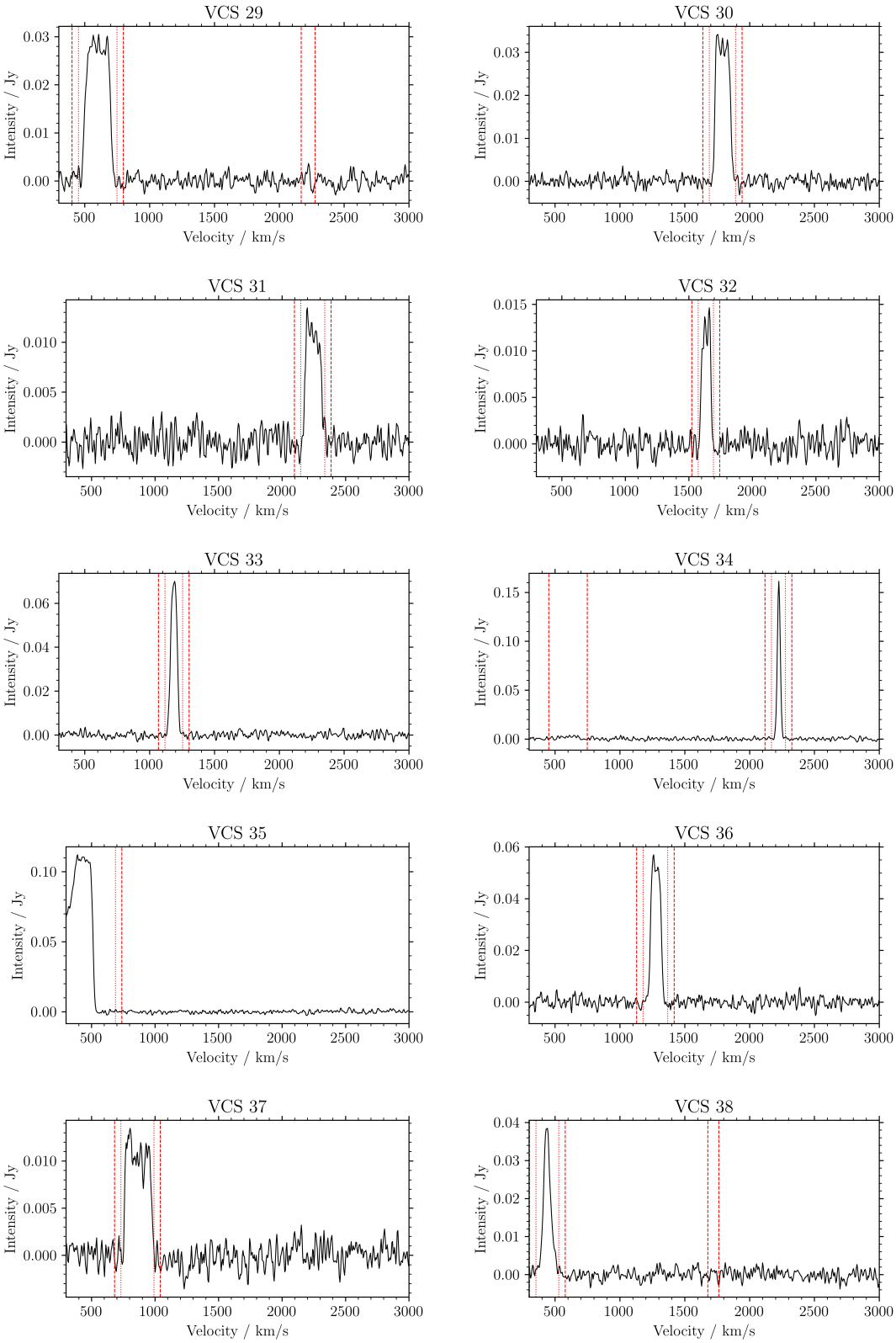

Figure A.4: Measured spectra of VCS 29 – 38. The dotted line shows profile of the line and the dashed line shows the mask.

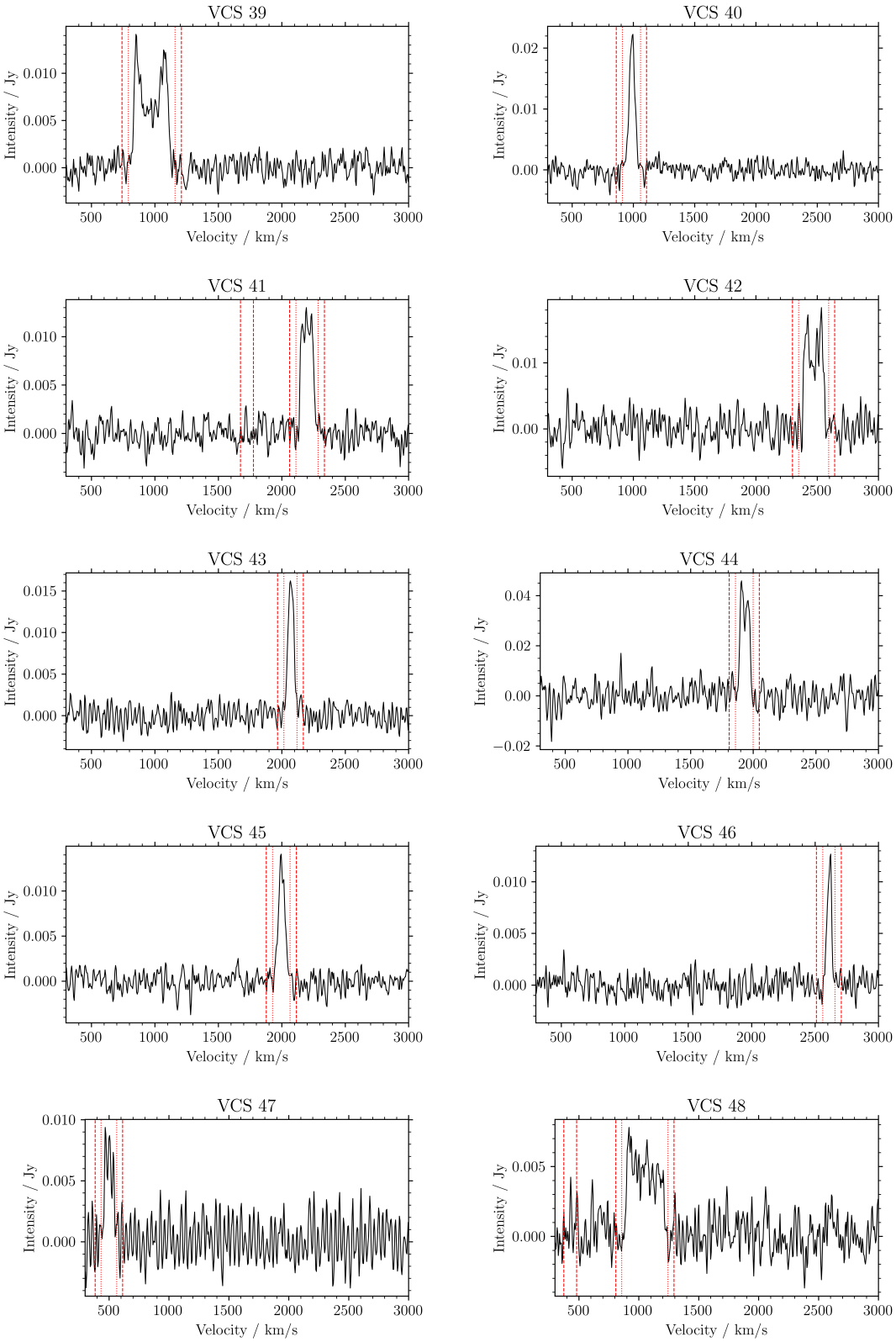

Figure A.5: Measured spectra of VCS 39 – 48. The dotted line shows profile of the line and the dashed line shows the mask.

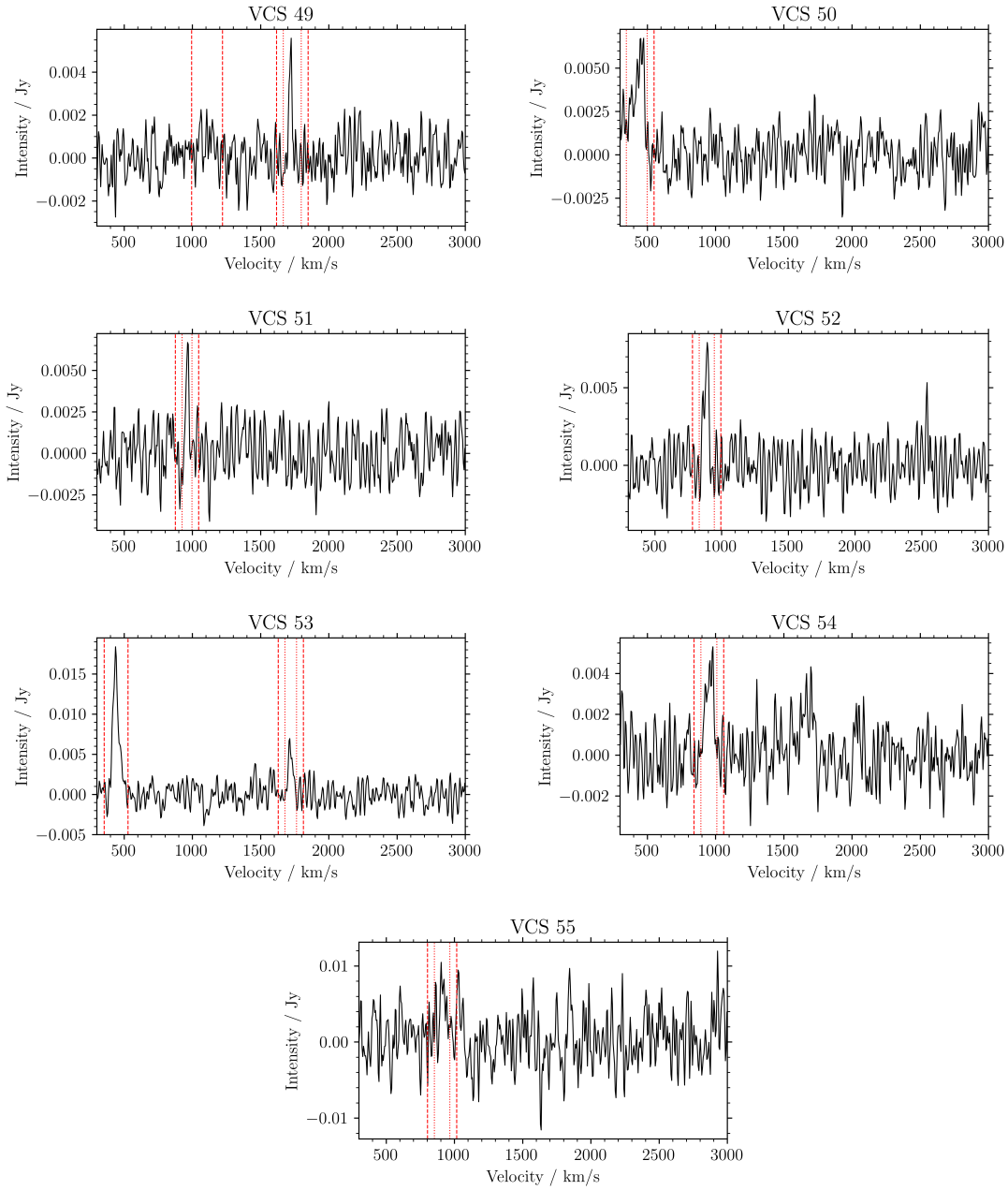

Figure A.6: Measured spectra of VCS 49 – 55. The dotted line shows profile of the line and the dashed line shows the mask.

A.2 Renzograms of the VCS objects

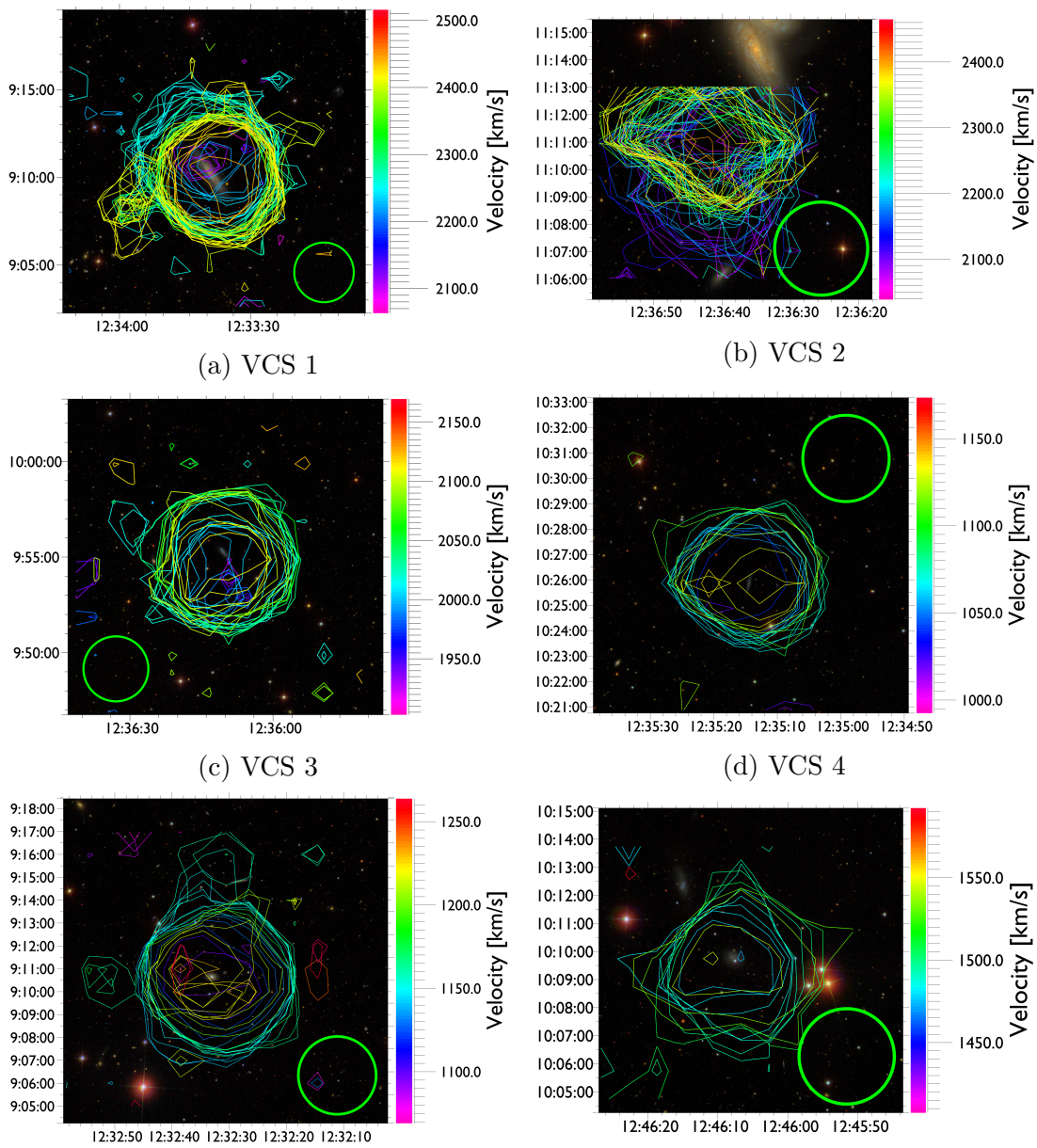

(a) VCS 1

(b) VCS 2

(c) VCS 3

(d) VCS 4

(e) VCS 5

(f) VCS 6

Figure A.7: Renzograms of VCS 1 – 6. The green circle in the corner shows the 3.5 arcmin beam size.

..

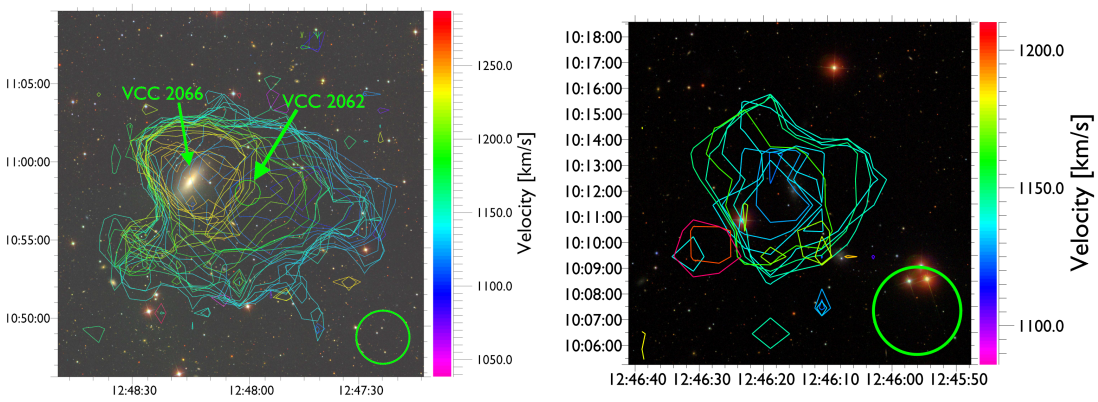

(a) VCS 7

(b) VCS 8

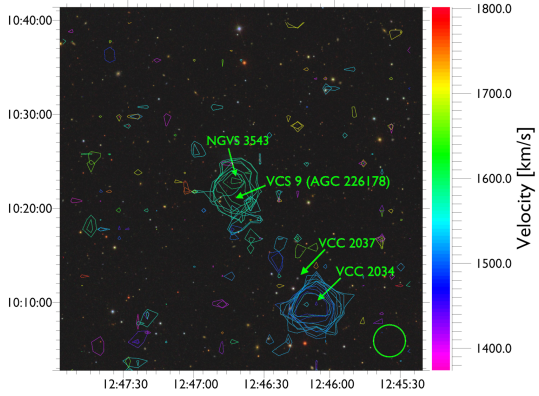

(c) VCS 9

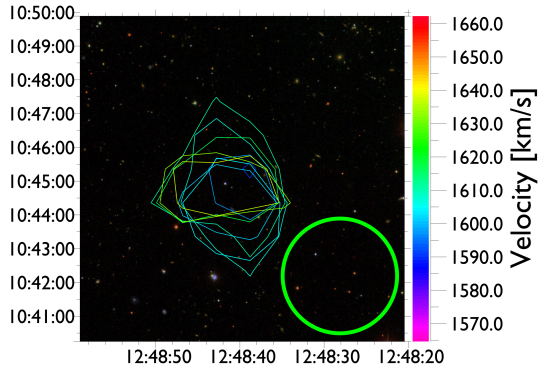

(d) VCS 10

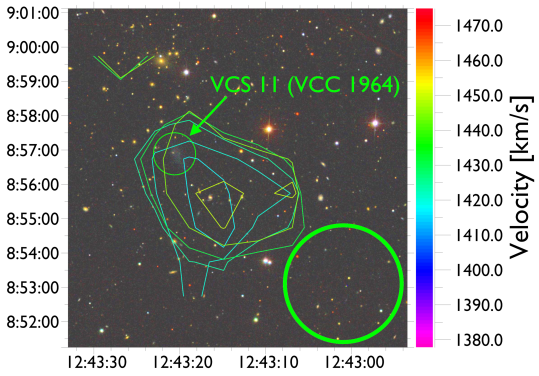

(e) VCS 11

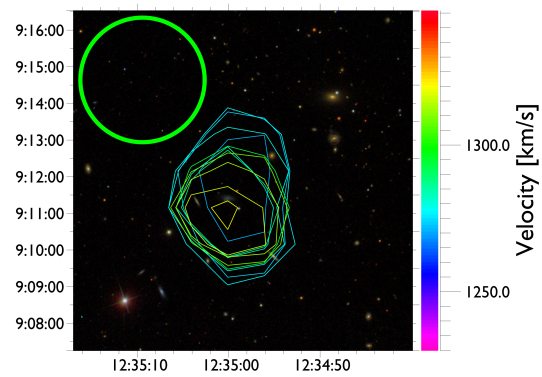

(f) VCS 12

Figure A.8: Renzograms of VCS 7 – 12. The green circle in the corner shows the 3.5 arcmin beam size.

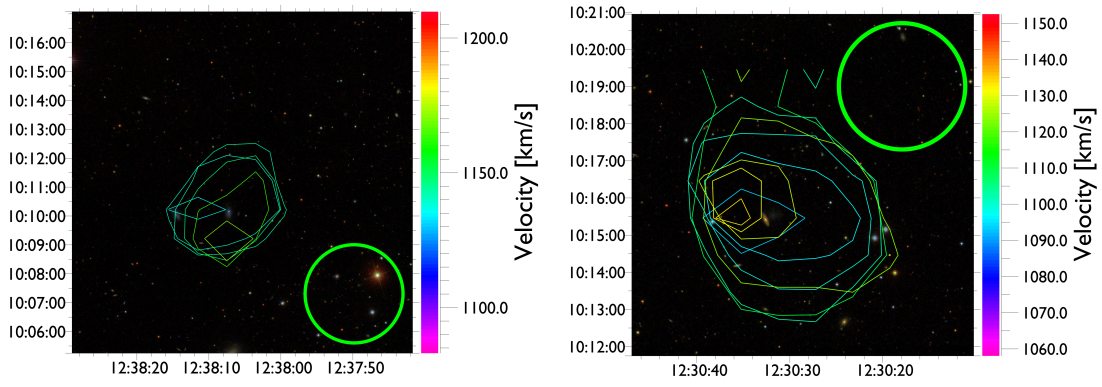

(a) VCS 13

(b) VCS 14

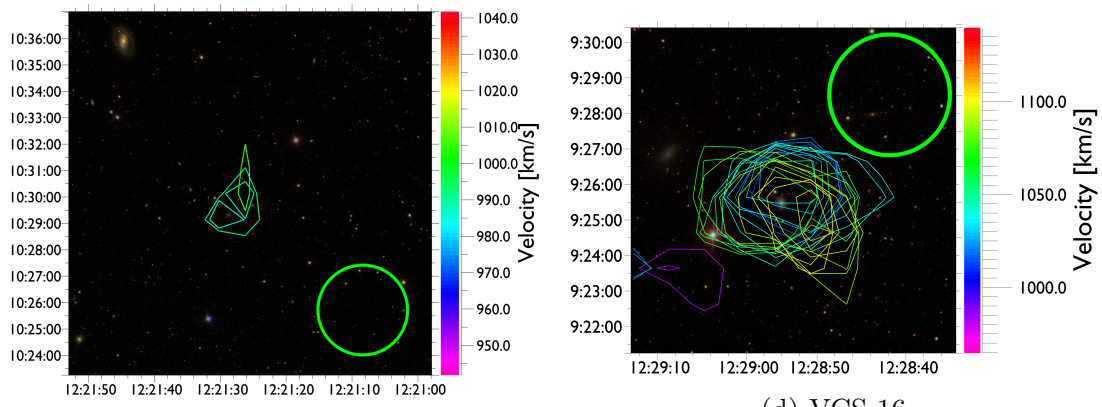

(c) VCS 15

(d) VCS 16

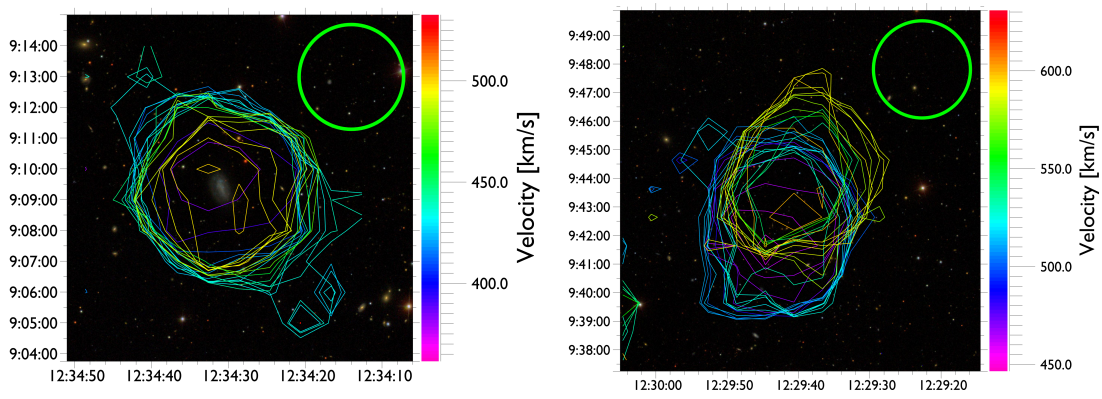

(e) VCS 17

(f) VCS 18

Figure A.9: Renzograms of VCS 13 – 18. The green circle in the corner shows the 3.5 arcmin beam size.

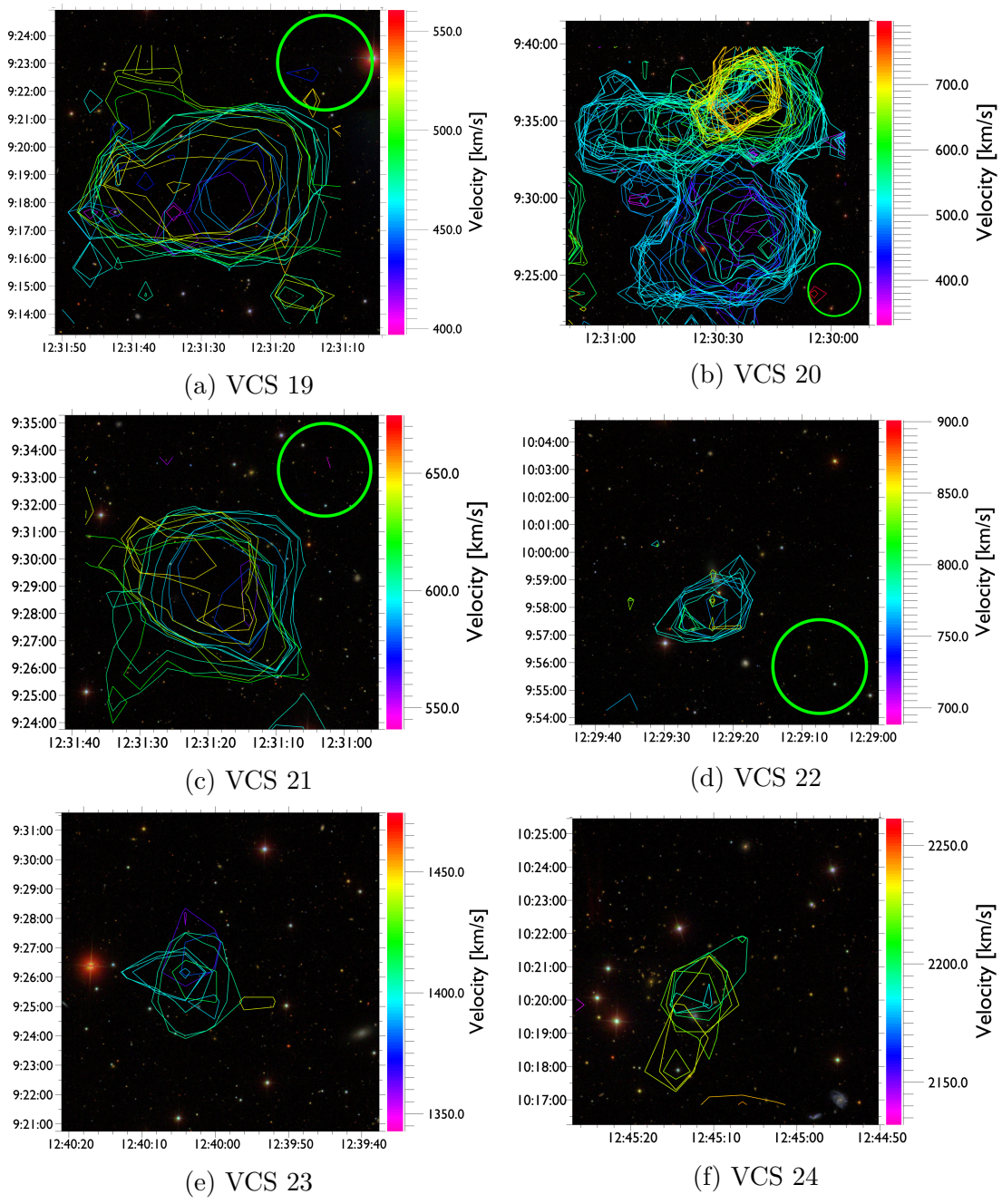

(a) VCS 19

(b) VCS 20

(c) VCS 21

(d) VCS 22

(e) VCS 23

(f) VCS 24

Figure A.10: Renzograms of VCS 19 – 24. The green circle in the corner shows the 3.5 arcmin beam size.

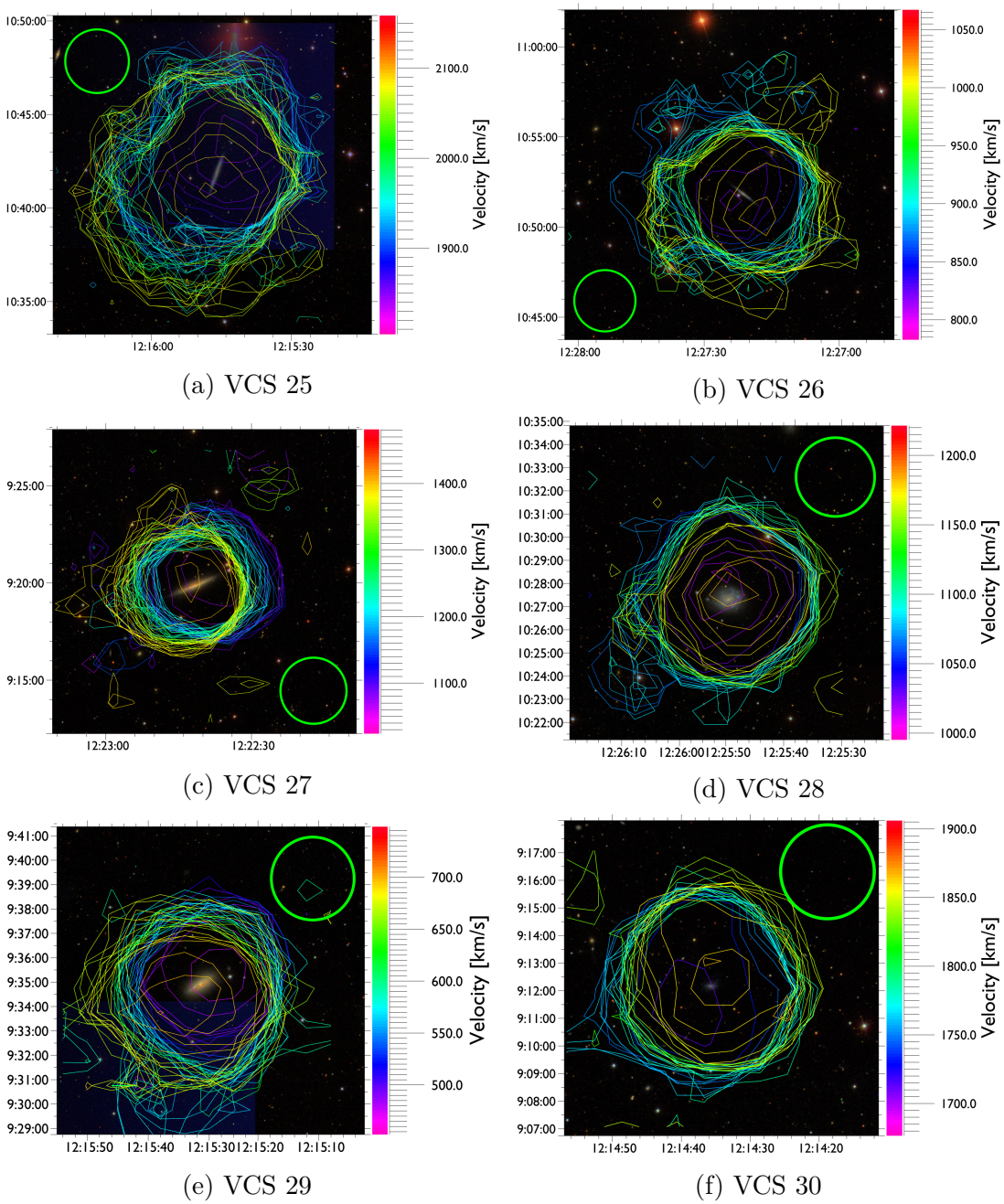

(a) VCS 25

(b) VCS 26

(c) VCS 27

(d) VCS 28

(e) VCS 29

(f) VCS 30

Figure A.11: Renzograms of VCS 25 – 30. The green circle in the corner shows the 3.5 arcmin beam size.

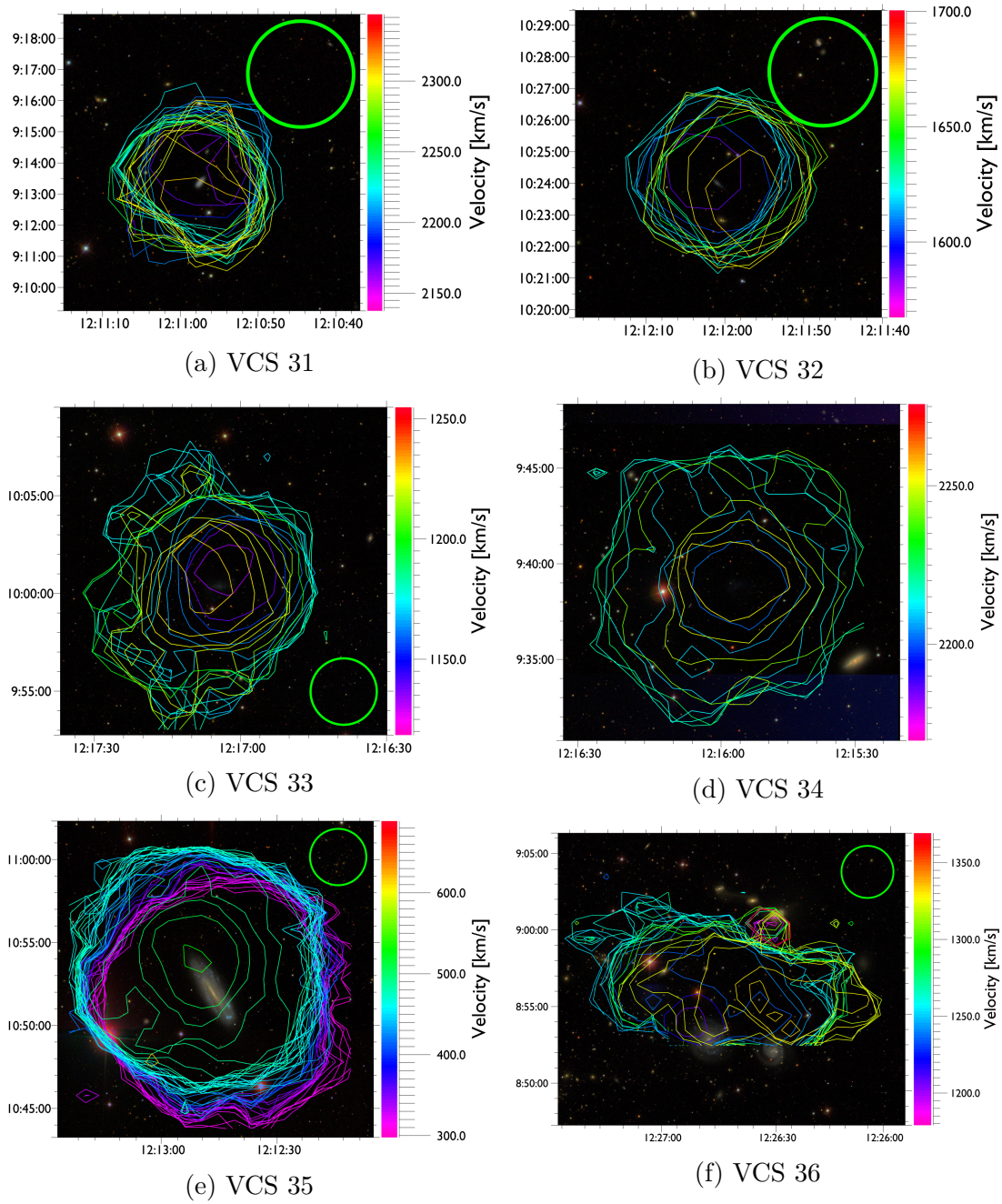

(a) VCS 31

(b) VCS 32

(c) VCS 33

(d) VCS 34

(e) VCS 35

(f) VCS 36

Figure A.12: Renzograms of VCS 31 – 36. The green circle in the corner shows the 3.5 arcmin beam size.

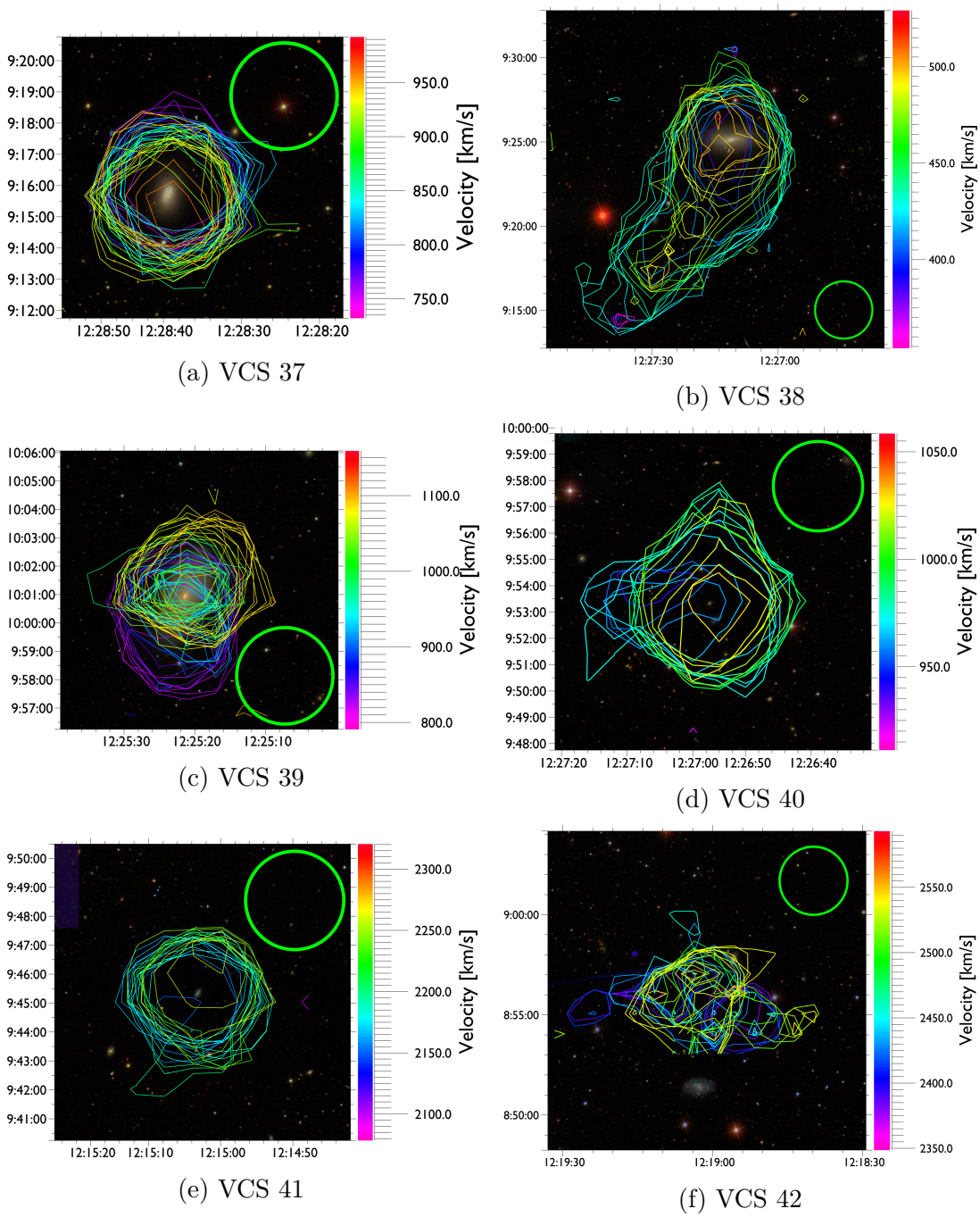

(a) VCS 37

(b) VCS 38

(c) VCS 39

(d) VCS 40

(e) VCS 41

(f) VCS 42

Figure A.13: Renzograms of VCS 37 – 42. The green circle in the corner shows the 3.5 arcmin beam size.

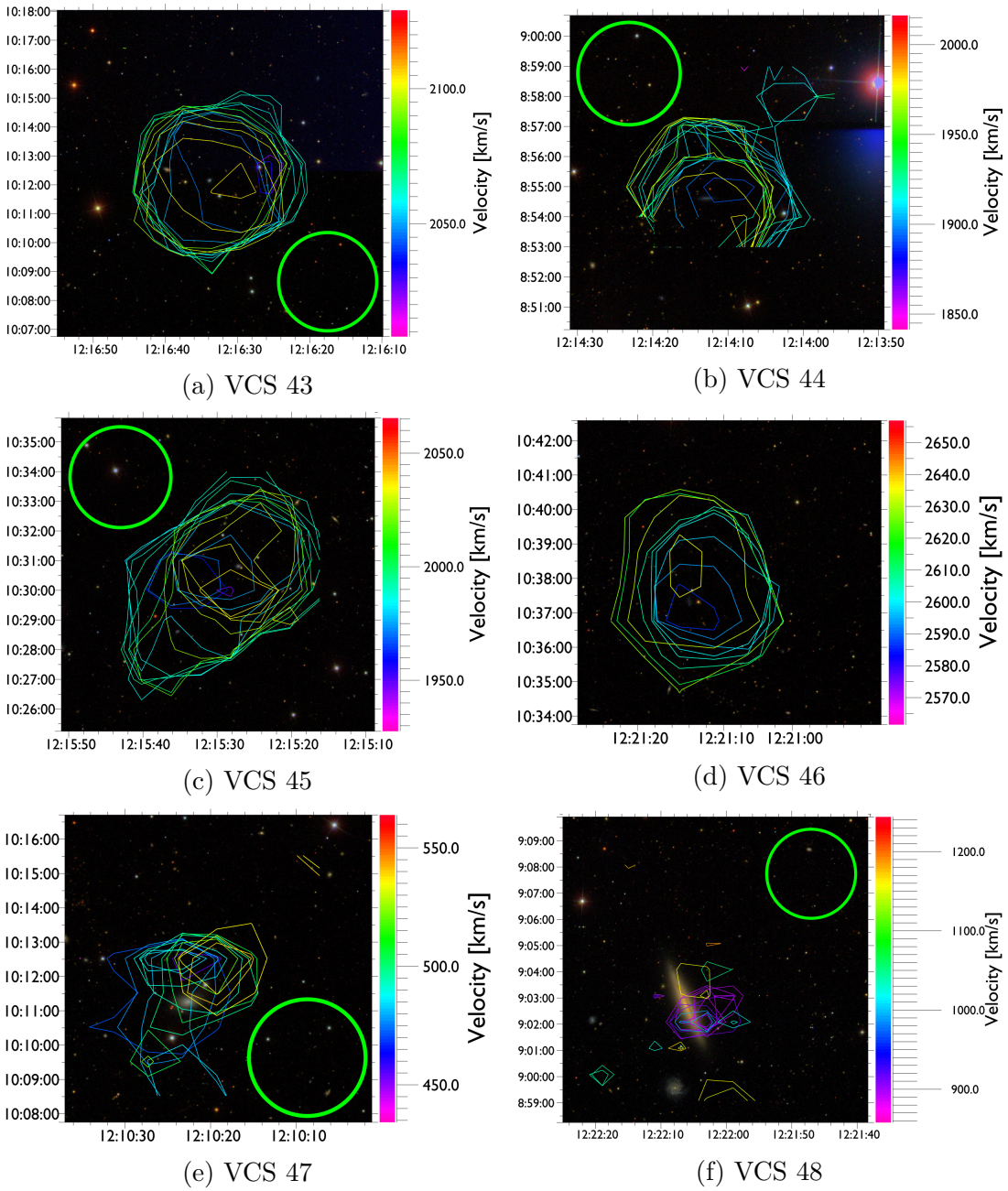

(a) VCS 43

(b) VCS 44

(c) VCS 45

(d) VCS 46

(e) VCS 47

(f) VCS 48

Figure A.14: Renzograms of VCS 43 – 48. The green circle in the corner shows the 3.5 arcmin beam size.

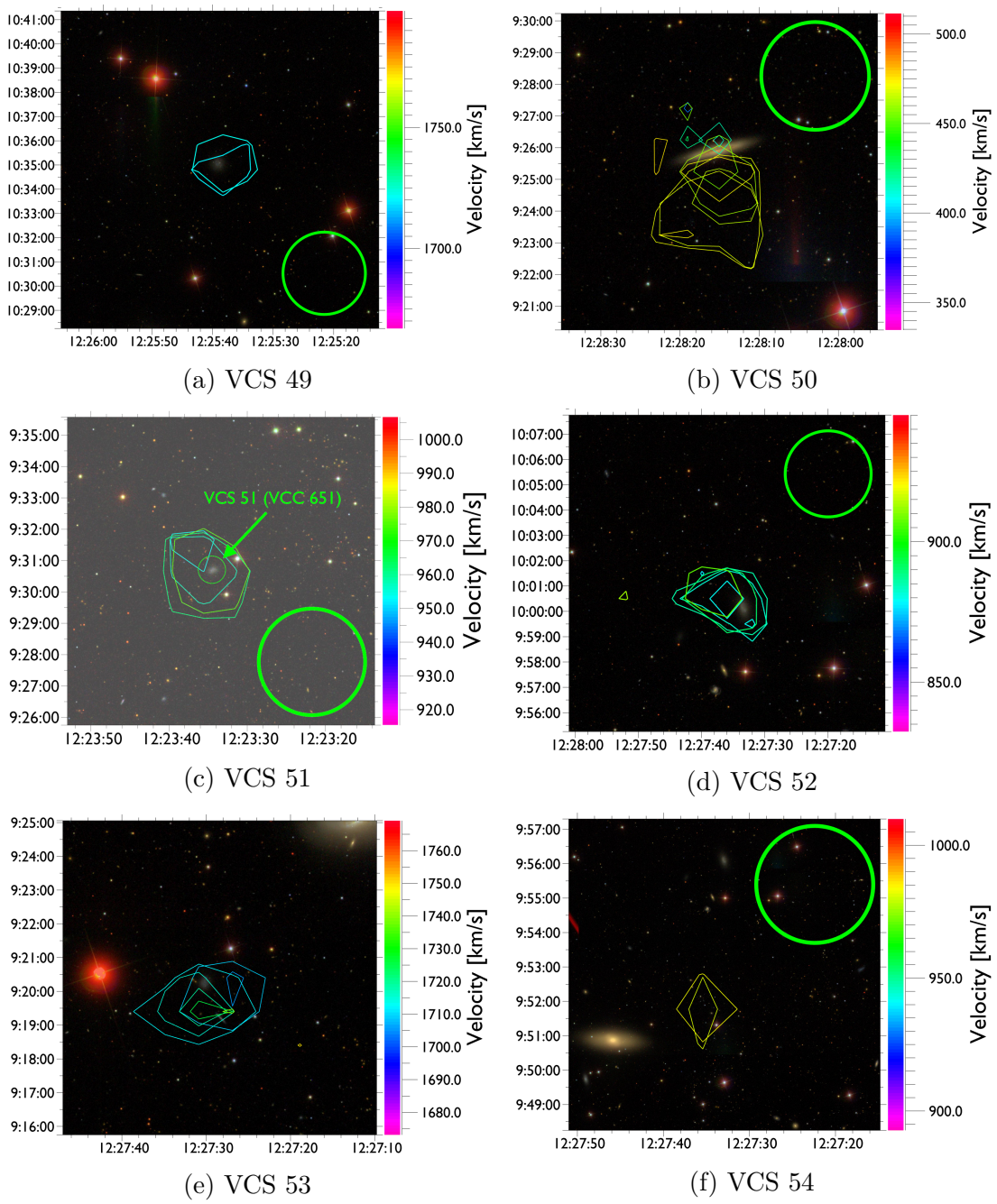

(a) VCS 49

(b) VCS 50

(c) VCS 51

(d) VCS 52

(e) VCS 53

(f) VCS 54

Figure A.15: Renzograms of VCS 49 – 54. The green circle in the corner shows the 3.5 arcmin beam size.

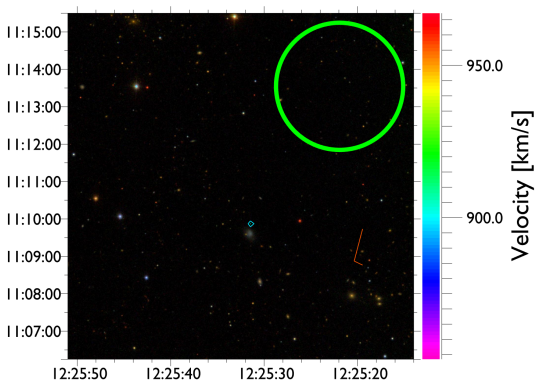

(a) VCS 55

Figure A.16: Renzogram of VCS 55. The green circle in the corner shows the 3.5 arcmin beam size.

A.3 List of uncertain HI sources

Table A.1: Table of uncertain sources cataloged by R. Taylor and their basic properties. Errors in brackets calculated by Miriad. If the position fitting failed, the coordinates brackets are empty. Total integrated S/N given by the equation 2.2. Only Extra_004 (gray background) was accepted as a real source (VCS 15), mainly thanks to its relatively high peak and integrated S/N and presence of an optical counterpart (VCC 476).

Name	RA (HH:MM:SS)	Dec (DD:MM:SS)	Vel [kms^{-1}]	SNpeak	SNtot
VCSExtra_001	12:45:24.87()	+09:00:45.87()	823(4)	5.3	1.3
VCSExtra_002	12:29:47.34(1.3)	+09:12:37.02(14)	254(13)	4.5	1.0
VCSExtra_003	12:41:04.38()	+10:58:58.07()	292(10)	4.4	1.3
VCSExtra_004	12:45:10.85(1.0)	+10:02:41.08(15)	252(4)	4.9	1.6
VCSExtra_005	12:44:32.56()	+09:33:49.06()	198(10)	4.4	1.0
VCSExtra_006	12:30:21.88(2.7)	+09:13:41.56(13)	253(9)	5.5	1.7
Extra_002	12:15:59.52()	+09:17:56.86()	673(10)	4.7	2.0
Extra_003	12:27:49.69(1.0)	+09:44:20.54(20)	130(14)	4.7	0.9
Extra_004	12:21:28.32(0.8)	+10:29:56.21(13)	997(4)	6.2	1.9
Extra_005	12:14:55.10(0.9)	+09:40:36.26(15)	172()	4.5	1.7
Extra_006	12:20:43.01(0.8)	+10:39:50.07(11)	232(12)	3.7	0.8
Extra_008	12:17:16.53(1.5)	+09:51:24.89(13)	185(6)	5.9	1.2